

AD 605215

# **THEORETICAL-EXPERIMENTAL CORRELATION OF LARGE DYNAMIC AND PERMANENT DEFORMATIONS OF IMPULSIVELY-LOADED SIMPLE STRUCTURES**

TECHNICAL DOCUMENTARY REPORT NO. FDL-TDR-64-108

July 1964

Air Force Flight Dynamics Laboratory  
Research and Technology Division  
Air Force Systems Command  
Wright-Patterson Air Force Base, Ohio

Project No. 6906, Task No. 690601

(Prepared under Contract No. AF 33(657)-8427  
by the Aeroelastic and Structures Research Laboratory  
Massachusetts Institute of Technology,  
Cambridge, Massachusetts  
Authors: Hans A. Balmer and Emmett A. Witmer)

REPRODUCED BY  
**NATIONAL TECHNICAL  
INFORMATION SERVICE**  
U S DEPARTMENT OF COMMERCE  
SPRINGFIELD, VA. 22161

188 P. 8

## NOTICES

\*When Government drawings, specifications, or other data are used for any purpose other than in connection with a definitely related Government procurement operation, the United States Government thereby incurs no responsibility nor any obligation whatsoever; and the fact that the Government may have formulated, furnished, or in any way supplied the said drawings, specifications, or other data, is not to be regarded by implication or otherwise as in any manner licensing the holder or any other person or corporation, or conveying any rights or permission to manufacture, use, or sell any patented invention that may in any way be related thereto.

Qualified requesters may obtain copies of this report from the Defense Documentation Center (DDC), (Formerly ASTIA), Cameron Station, Bldg. 5, 5010 Duke Street, Alexandria, Virginia, 22314.

This report has been released to the Office of Technical Services, U.S. Department of Commerce, Washington 25, D. C., for sale to the general public.

Copies of this report should not be returned to the Research and Technology Division, Wright-Patterson Air Force Base, Ohio, unless return is required by security considerations, contractual obligations, or notice on a specific document.

FDL-TDR-64-108

THEORETICAL-EXPERIMENTAL CORRELATION OF  
LARGE DYNAMIC AND PERMANENT DEFORMATIONS OF  
IMPULSIVELY-LOADED SIMPLE STRUCTURES

TECHNICAL DOCUMENTARY REPORT NO. FDL-TDR-64-108

July 1964

Air Force Flight Dynamics Laboratory  
Research and Technology Division  
Air Force Systems Command  
Wright-Patterson Air Force Base, Ohio

Project No. 6906, Task No. 690601

(Prepared under Contract No. AF 33(657)-8427  
by the Aeroelastic and Structures Research Laboratory  
Massachusetts Institute of Technology,  
Cambridge, Massachusetts  
Authors: Hans A. Balmer and Emmett A. Witmer)

## FOREWORD

This report was prepared by the Massachusetts Institute of Technology, Cambridge, Massachusetts on Air Force Contract AF 33(657)-8477 under Project 6906, "Nuclear Weapons Effects on Space Vehicles," and Task No. 690601, "Determination of High Altitude Nuclear Weapon Effects on Space Vehicles", which are a part of the Air Force Systems Command's applied research program 710A, "NUCLEAR WEAPONS EFFECTS." The work was administered under the direction of the Air Force Flight Dynamics Laboratory, Research and Technology Division; Mr. L. E. Gilbert and Mr. J. Dolan served as project engineers for the laboratory.

The contractor's report number is ASRL 110-2.

This report is UNCLASSIFIED.

The authors gratefully acknowledge the efforts and cooperation of Air Force Flight Dynamics Laboratory personnel, L.E. Gilbert, F.O. Chinn, and J. Dolan and Picatinny Arsenal personnel, E.N. Clark, F.H. Schmitt, and their associates in obtaining and furnishing needed data on the stress-strain properties and responses of explosively-loaded beams and circular rings.

The authors are much indebted to Professor T.H.H. Pian, Mr. J.W. Leech, and Dr. W. Herrmann of the MIT Aeroelastic and Structures Research Laboratory for much valuable advice and discussion on theoretical and experimental questions throughout the program described in this report. Also, for assistance and the use of the facilities of the Massachusetts Institute of Technology Computation Center for a part of the present calculations, the authors wish to express their appreciation.

## ABSTRACT

A general numerical method previously developed for analyzing large dynamic two-dimensional deformations of simple structures (and of large axisymmetric dynamic deformations of plates and shells with rotational symmetry) has been extended and evaluated through comparisons of predictions with experimental dynamic response and permanent-deformation data from explosively-loaded beams and circular rings. The method accounts for elastic, perfectly-plastic, strain hardening, and strain rate behavior of the structural material, and the experimental specimens employed were chosen to emphasize one or more of these characteristics and to provide tests of the adequacy of the theoretical prediction method.

The governing finite-difference equations may be interpreted as representing a finite number of concentrated masses connected by straight extensible elements with bending concentrated at the mass locations themselves. The increments in stress resultants and stress couples are determined by idealizing the shell thickness as consisting of  $n$  (even) concentrated layers of material separated by a material that cannot carry normal stress but has infinite shear rigidity. The influences of the number of layers in the idealized-thickness model, the spacing between these layers, the number of masses employed, as well as the aforementioned types of material behavior are demonstrated and discussed in detail. The present method also permits examining the subsequent partitioning of the initial input kinetic energy of impulsively-loaded structures into plastic, elastic, and kinetic forms; this feature is also illustrated and discussed.

Transient response comparisons of the present method, rigid-plastic theory, and experiment show that the present method yields considerably better results with essentially no greater labor than required for the very restrictive rigid-plastic theory. For cases in which the plastic energy absorption is a large fraction of the initial energy input to impulsively-loaded structures, a simple approximate energy method, a rigid-plastic transient-response theory, and the present method predict comparable permanent deformations, but not otherwise.

Residual uncertainties in the experimental data and the theoretical method are discussed, and measures to reduce these uncertainties are proposed.

#### PUBLICATION PREVIEW

This report has been reviewed and is approved.

FOR THE DIRECTOR



HOLLAND B. LOWNDES, JR.  
Acting Chief, Structures Division  
Air Force Flight Dynamics Laboratory

## TABLE OF CONTENTS

<u>Section</u>		<u>Page</u>
I	INTRODUCTION	1
II	BRIEF DESCRIPTION OF EXPERIMENTS	3
	2.1 Scope of Experiments	3
	2.2 Brief Description of Test Specimens, Arrangement, Procedures, and Response Measurements	4
	2.3 Impulse Calibration Tests	5
	2.4 Material-Property Measurements	8
	2.4.1 Static Properties	9
	2.4.2 Dynamic Properties	10
III	REVIEW OF PRESENT THEORETICAL METHOD AND ITS RESPONSE-PREDICTION FEATURES	12
	3.1 Introduction	12
	3.2 Review of Theory Employed Herein	14
	3.2.1 Two-Dimensional Structures	14
	Equations of Motion	14
	Idealized-Thickness Model	18
	Strain-Displacement Relations	20
	Stress-Strain Relations	21
	Energy Distribution in the System	27
	Boundary Conditions	29
	Initial Conditions	32
	Symmetric Motion of a Free Ring	34

<u>Section</u>	<u>Page</u>
3.2.2 Axisymmetric Shells	36
Equations of Motion	36
Yield Condition and Flow Rule	37
3.3 Effects of Dynamic Model Features and Material Properties on Predicted Structural Response	38
3.3.1 Effects of Calculation-Model Parameters	38
Effect of Space-Mesh Size	39
Effects of Calculation-Time Interval	41
Effect of the Number of Flanges of the Idealized-Thickness Model	42
Effect of Flange Spacing	44
3.3.2 Effects of Stress-Strain Approximations	45
3.3.3 Effects on Energy Distribution in the System	48
IV CORRELATION OF THEORY WITH EXPERIMENT	
4.1 Introductory Comments	50
4.2 Material Stress-Strain Descriptions	52
4.2.1 Static Data	52
6061-T6 Beam Material	52
2024-0 Beam Material	53
1010 Steel Beam Material	54
6061-T6 Ring Material	54

<u>Section</u>	<u>Page</u>
4.2.2 Dynamic Data	55
6061-T6 Beam Material	55
2024-0 Beam Material	57
1010 Steel Beam Material	58
4.3 Beams of 6061-T6 Material	60
4.3.1 Predominant Bending Cases: SS Beams	63
4.3.2 Predominant Stretching Cases: Clamped Beams	66
4.4 Beams of 2024-0 Material	68
4.4.1 Predominant Bending Cases: SS Beams	69
4.4.2 Predominant Stretching Cases: Clamped Beams	70
4.5 Beams of 1010 Steel Material	72
4.5.1 Predominant Bending Cases: SS Beam	72
4.5.2 Predominant Stretching Cases: Clamped Beam	73
4.6 Circular Rings	74
4.6.1 Free Circular Rings	74
4.6.2 Clamped Ring	78
4.7 Comparisons with Rigid-Plastic Theory	80
4.8 Summary Comments on the Present Comparisons	82

<u>Section</u>	<u>Page</u>
V SUMMARY AND CONCLUSIONS	
5.1 Theory and Correlation	87
5.2 Experiment	91
REFERENCES	93

## LIST OF TABLES

<u>Table</u>		<u>Page</u>
4.1	Identification of Static and Dynamic Stress-Strain Specimens from Material Lots Associated with Impulsively-Loaded Beams and Rings	96
4.2	Summary of Bi-Linear Approximations to Static Stress-Strain Properties of Beam and Ring Materials	97
4.3	Five-Segment Fit of 2024-0, Lot V (Termed Fit No. 9)	97
4.4	Summary of Dimension and Loading Data for Impulsively-Loaded Beams and Rings	98
4.5	Summary of Theoretical-Prediction Features and Parameters used to Compare with Experimental Responses of Explosively-Loaded Beams and Rings	99
4.6	Comparison Between Experimental and Predicted Permanent Midspan Beam Deflections Obtained by an Approximate Energy Method	101

## ILLUSTRATIONS

<u>Figure</u>		<u>Page</u>
2.1	Schematics of Explosively-Loaded Simple Structures	102
2.2	HE Edge Effects on the Spanwise Distribution of Imparted Impulse	103
2.3	Schematic of Arrangement for Measuring Dynamic Stress-Strain Properties	104
3.1	Nomenclature for a Two-Dimensional Structure	105
3.2	Lumped-Parameter and Idealized-Thickness Model	106
3.3	Idealized Stress-Strain Relations	107
3.4	Boundary Conditions	108
3.5	Nomenclature for a Shell of Revolution	109
3.6	Effect of Space Mesh Size on Dynamic Response of a Clamped Beam	110
3.7	Effect of Space Mesh Size on Deflection Profiles of a Clamped Beam	111
3.8	Effect of Space Mesh Size on Dynamic Response of a Simply-Supported Beam	112
3.9	Effect of Space Mesh Size on Deflection Profiles of a Simply-Supported Beam	113
3.10	Deflection of a Selected Spanwise Point as a Function of Number of Masses for a Simply-Supported Beam	114
3.11	Effect of Calculation Time Interval on Dynamic Response of a Simply-Supported Beam	115

<u>Figure</u>		<u>Page</u>
3.12	Effect of Number of Flanges of Idealized-Thickness Model on Dynamic Response of a Clamped Beam	116
3.13	Effect of Number of Flanges of Idealized-Thickness Model on Dynamic Response of a Simply-Supported Beam	117
3.14	Effect of Flange Spacing on Dynamic Response of a Simply-Supported Beam	118
3.15	Effect of Different Stress-Strain Curve Fits on Dynamic Response of a Clamped Beam	119
3.16	Effect of Different Stress-Strain Curve Fits on Dynamic Response of a Simply-Supported Beam	120
3.17	Ratios of Energies to Initially Imparted Kinetic Energy for a Simply-Supported Beam	121
3.18	Ratios of Energies to Initially-Imparted Kinetic Energy for a Clamped Beam	122
4.1	Measured and Fitted Static Stress-Strain Properties of 6061-T6 Aluminum Beam Materials	123
4.2	Measured and Fitted Static Stress-Strain Properties of 2024-0 Aluminum Beam Materials	124
4.3	Five-Segment Fit of Static Stress-Strain Properties of 2024-0 Beam Material	125
4.4	Measured and Fitted Static Stress-Strain Properties of 1010 Steel Beam Material	126
4.5	Measured and Fitted Static Stress-Strain Properties of 6061-T6 Ring Material	127

<u>Figure</u>		<u>Page</u>
4.6	Measured Static and Dynamic Stress-Strain Properties of 6061-T6 Beam Material	128
4.7	Measured Static and Dynamic Stress-Strain Properties of 2024-0 Beam Material	129
4.8a	Illustrative Time Histories of Stress and Strain of 1010 Steel Specimens	130
4.8b	Dynamic Stress-Strain Characteristics of 1010 Steel Specimen 6	131
4.8c	Dynamic Stress-Strain Characteristics of 1010 Steel Specimen 10	132
4.9	Static and Dynamic Measurements of Stress-Strain Properties of 1010 Steel Specimens	133
4.10	Idealized Representation of Static and Dynamic Stress-Strain Properties of the Present 1010 Steel Material	134
4.11	Comparison of Data on Strain-Rate Effect on Yield Stress of Steel and Aluminum	135
4.12	Comparison of Predicted and Experimental Midspan-Deflection Responses for Explosively-Loaded Simply-Supported 6061-T6 Beam 121	136
4.13	Comparison of Predicted and Experimental Deformation Profiles for Explosively-Loaded Simply-Supported 6061-T6 Beam 121	137
4.14	Comparison of Predicted and Experimental Midspan-Deflection Responses for Explosively-Loaded Simply-Supported 6061-T6 Beam 131	138

<u>Figure</u>		<u>Page</u>
4.15	Comparison of Predicted and Experimental Midspan-Deflection Responses for Explosively-Loaded Clamped 6061-T6 Beam 111	139
4.16	Comparison of Predicted and Experimental Deformation Profiles for Explosively-Loaded Clamped 6061-T6 Beam 112	140
4.17	Comparison of Predicted and Experimental Midspan-Deflection Responses for Explosively-Loaded Clamped 6061-T6 Beam 95	141
4.18	Comparison of Predicted and Experimental Strain-Time Histories for Explosively-Loaded Clamped 6061-T6 Beam 3	142
4.19	Comparison of Predicted and Experimental Strain-Time Histories for Explosively-Loaded Clamped 6061-T6 Beam 2	143
4.20	Comparison of Predicted and Experimental Midspan-Deflection Responses for Explosively-Loaded Simply-Supported 2024-0 Beam 119	144
4.21	Comparison of Predicted and Experimental Midspan-Deflection Responses for Explosively-Loaded Simply-Supported 2024-0 Beam 134	145
4.22	Comparison of Predicted and Experimental Midspan-Deflection Responses for Explosively-Loaded Clamped 2024-0 Beam 88	146
4.23	Further Comparisons of Clamped 2024-0 Beam 88	147
4.24	Comparison of Predicted and Experimental Midspan-Deflection Responses for Explosively-Loaded Clamped 2024-0 Beam 100	148

<u>Figure</u>		<u>Page</u>
4.25	Comparison of Predicted and Experimental Mid-span-Deflection Responses for Explosively-Loaded Simply-Supported 1010 Steel Beam 129	149
4.26	Comparison of Predicted and Experimental Mid-span-Deflection Responses for Explosively-Loaded Clamped 1010 Steel Beam 89	150
4.27	Illustration of Predicted Deflection Profiles for Clamped 1010 Steel Beam 89 at Several Instants of Time	151
4.28	Comparison of Predicted and Experimental Central Separation Responses for Explosively-Loaded 6061-T6 Free Circular Ring F4	152
4.29	Comparison of Predicted and Experimental Permanent Deformation Profiles for Explosively-Loaded 6061-T6 Free Circular Ring F4	153
4.30	Comparison of Predicted and Experimental Strain-Time Histories for Explosively-Loaded 6061-T6 Free Circular Ring F4	154
4.31	Strain Profiles for Explosively-Loaded 6061-T6 Free Circular Ring F4	156
4.32	Comparison of Predicted and Experimental Central Separation Responses for Explosively-Loaded 6061-T6 Free Circular Ring F15	157
4.33	Comparison of Predicted and Experimental Deformation Profiles for Explosively-Loaded 6061-T6 Free Circular Ring F15	158
4.34	Comparison of Predicted and Experimental Strain-Time Histories for Explosively-Loaded 6061-T6 Free Circular Ring F15	161

<u>Figure</u>		<u>Page</u>
4.35	Strain Profiles for Explosively-Loaded 6061-T6 Free Circular Ring F15	163
4.36	Comparison of Predicted and Experimental Central Deflection Responses for Explosively- Loaded 6061-T6 Clamped Circular Ring C4	164
4.37	Comparison of Predicted and Experimental Deformation Profiles for Explosively-Loaded 6061-T6 Clamped Circular Ring C4	165
4.38	Comparison of Predicted and Experimental Strain-Time Histories for Explosively- Loaded 6061-T6 Clamped Circular Ring C4	167
4.39	Strain Profiles for Explosively-Loaded 6061-T6 Clamped Circular Ring C4	169
4.40	Comparison of Transient Responses Obtained by the Present Elastic-Plastic Theory and Rigid-Plastic Theory (Simply-Supported Beam 121)	171

## SECTION I

### INTRODUCTION

The prediction of large dynamic and permanent deformations of simple structures usually involves an accounting for both geometric and material constitutive nonlinearities. Rigid-plastic analysis together with the assumption of small displacements has been applied to obtain closed-form solutions to estimate permanent plastic deformations of simple beams [1, 2]. When large deflections are taken into account, the rigid-plastic approximation no longer permits closed-form analytical solutions, and numerical methods must be used. Furthermore, the rigid-plastic analysis is applicable only to problems in which the elastic energy of the system is negligible compared with the plastic energy absorbed by the structure. In many practical problems, however, this condition is not realized. Therefore, a more realistic method of analysis is required.

The research reported in Reference 3 was conducted in order to develop a general numerical method of analysis of the large-deformation dynamic elastic-plastic behavior of simple structures for which the region of severe post-elastic deformation does not remain at a fixed structural station but propagates. The elastic-plastic analysis developed underwent preliminary evaluation [4] by comparing predictions with dynamic deformations measured on a few initial structural specimens from a comprehensive experimental program [5, 6] designed to provide well-defined data on large dynamic strains and deformations, impulse loading, and permanent deformations

- - - - -  
Manuscript released by the authors June 1964 for publication as an RTD Technical Documentary Report.

of impulsively-loaded beams and rings. Now that those experiments have been completed, it is possible to carry out an extensive detailed evaluation of the adequacy of the elastic-plastic analysis [3]; reporting that evaluation and describing certain modifications of the analysis are the purposes of the present report.

For purposes of clarity and continuity, a brief description of the subject impulsive-loading and structural-response experiments is given in Section II; a complete account may be found in Reference 6. Section III is devoted to a brief description of the elastic-plastic method of analysis and a description of the effects on structural response of various material properties and dynamic-model features. In Section IV, detailed comparisons of elastic-plastic theory with experiment in terms of dynamic deformation and strain response and permanent deformations of explosively-loaded clamped and simply-supported beams (6061-T6 and 2024-0 aluminum alloy and 1010 steel) and 6061-T6 circular rings which are freely suspended and clamp-supported are given. Also, some comparisons are shown among experiments and predictions from elastic-plastic theory, rigid-plastic theory, and an approximate energy method. Summary remarks and conclusions with reference to the adequacy of the theory and merits of the experiments are given in Section V.

## SECTION II

### BRIEF DESCRIPTION OF EXPERIMENTS

#### 2.1 Scope of Experiments

The experiments discussed in this section of the report are those which were designed and conducted expressly within and to support the present Air Force-sponsored research program\*. The types of experiments needed were designed by the MIT Aeroelastic and Structures Research Laboratory in conjunction with AFFDL project personnel and Picatinny Arsenal personnel. The detail designs of testing fixtures, photographic arrangements, explosive-loading techniques, static and dynamic tests of models, etc., were carried out by Picatinny Arsenal personnel under AFFDL sponsorship.

These experiments consisted of explosively loading clamped rectangular beams, simply-supported beams, free single-layer rings, and clamped single-layer rings, and measuring the transient deformations and strains, and the permanent deformations of these structures. In support of these experiments, it has been necessary to conduct supplementary experiments to define (a) the explosively-imparted impulse to the above test specimens and (b) the static and the dynamic stress-strain properties of coupons of materials from the same material lots as those for the beam and ring materials actually employed in the explosive-loading tests. All of this work is described briefly in the following subsection.

- - - - -  
\* Air Force Flight Dynamics Laboratory, Research and Technology Division, Project No. 6699, "Nuclear Weapon Effects on Space Vehicles," Task No. 690601, "Determination of High Altitude Nuclear Weapon Effects on Space Vehicles," Contract No. AF 33(657)-8427.

## 2.2 Brief Description of Test Specimens, Arrangement, Procedures and Response Measurements

Figure 2.1 illustrates schematically the four types of explosive-loading experiments conducted. Clamped and simply-supported rectangular beams of 6061-T6 and 2024-0 aluminum alloy and heat treated\* 1010 steel were tested. Also, single-layer circular rings of 6061-T6 aluminum alloy were tested in both freely suspended and clamped configurations. As indicated, each test specimen has its entire width and a portion of its span or periphery covered by a thin layer of high explosive (HE). The test specimen is separated from the HE layer by a thin layer of a suitable buffer material (in this case, polyethylene) which attenuates and lengthens the pressure pulse so that spall fracture of the test specimen by the otherwise excessively short-duration and intense pressure pulse produced by detonation of the thin layer of HE does not occur.

Through the use of high-speed streak and framing cameras, respectively, the deformation time history at the mid-span or diameter of the specimen and the spanwise and peripheral deformations at various times throughout the response to the permanent-deformation condition were obtained. Baffles were provided adjacent to the edges of the test specimen to reduce and/or prevent obscuration of the test specimen by the

- - - - -

\* Normalized at 1650°F for one hour, then air cooled, next annealed at 1600°F for one hour, and then furnace cooled at 250°F per hour in a hydrogen atmosphere, as reported in Krafft, J.M. and Sullivan, A.M., "Effect of Grain Size and Carbon Content on the Yield Delay Time of Mild Steel," Transactions of the American Society for Metals, Vol. 51, pp. 643-659, 1959.

detonation products. Strain time histories were measured using strain gages attached at several locations on certain beam and ring specimens. Further discussion of these measurements and their comparisons with theory is given in Section IV.

As shown schematically in Fig. 2.1, the detonation of the HE layer proceeds uniformly across the width of the test specimen, thus inducing some dynamic twisting rather than purely two-dimensional deformation. Hence, the streak camera deformation measurements inherently contain this effect; the camera employed has a very limited depth of field and was focused on the front edge of the specimen. The effect of this dynamically-induced twisting may be seen by examining (for example, in Table 4.4) the permanent midspan deflections at the front edge and the rear edge of several of the clamped-beam specimens.

### 2.3 Impulse Calibration Tests

In order to define reliably the explosive impulse imparted to the test specimens, Picatinny Arsenal personnel conducted a series of "impulse calibration" experiments in which unrestrained "timepiece specimens" of 6061-T6 and 2024-0 aluminum alloy and 1010 steel were explosively loaded and their resulting velocities measured to determine the impulse imparted to each. In all cases, the timepiece was separated from intimate contact with the HE layer by a layer of polyethylene buffer of the same thickness and density as that used in the beam and ring tests. The HE material employed was DuPont EL 506D, and was from the same lot of HE sheet as used in the dynamic loading tests of the beam and

ring specimens. Since the beam (and ring) specimens had only a portion of their spans or peripheries covered by HE, it was convenient to conduct calibrations for both (a) one-dimensional behavior and (b) finite-span HE effects or "edge effects."

For the tests to determine imparted impulse under one-dimensional behavior, a timepiece of nominal dimensions: 0.25 inch thick by 1.2 inches wide by 1.5 inches long was placed in a test fixture such that it was surrounded on its 1.2 and 1.5-inch sides by two steel and two aluminum baffle plates. There was an extremely small gap between the timepiece and the baffle plates so that the timepiece could fall freely. The polyethylene and HE layers placed on this configuration extended well beyond the edges of the timepiece so that explosive edge effects would not influence the velocity imparted to the timepiece upon detonation of the HE layer. This velocity was measured by photographing the timepiece against a known space grid background with high-speed cameras operating at a known speed. A streak camera observed the centerline of the spanwise front edge of the timepiece while a framing camera viewed the specimen in a direction parallel to the direction of detonation wave propagation across the width direction of the specimen. For timing scales, 10 kc and 1 kc pips were applied to the film of the streak camera and the framing camera, respectively.

In these tests, nominal HE-layer uniform thicknesses of 0.010, 0.015, 0.020, and 0.030, and 0.045 inch were employed. The weight per unit area of each HE layer employed and of each timepiece was measured carefully. From these values and the measured timepiece velocities, the total impulse per gram of explosive (i.e., specific impulse) was determined for a wide range of ratios  $W/C$ , where  $W$  is the weight per unit

area of timepiece and  $C$  is the weight per unit area of explosive. It was found that the specific impulse exhibits no significant variation for  $W/C$  values greater than about 3; this "limit" was always exceeded by a wide margin in the structural response experiments of this program. It was found for the lot of explosive used for these structural and impulse-calibration experiments that the average effective impulse from 14 tests on 6061-T6 aluminum alloy test timepieces was  $18.6 \times 10^4$  dyne-sec/gm. HE. Similar experiments performed using 3 samples of 2024-0 aluminum and 6 samples of 1010 steel gave effective impulses of  $18.2 \times 10^4$  and  $18.5 \times 10^4$  dyne-sec/gm. HE, respectively. Hence,  $18.6 \times 10^4$  dyne-sec/gm. HE was employed in all calculations involving dynamic response of explosively-loaded test specimens in this program.

The effect of finite-span of the HE layer on the distribution of imparted impulse to a test specimen near the edges of the HE layer was studied experimentally. This was accomplished by dividing a 6061-T6 aluminum timepiece into segments of  $1/4$ -inch span for a total span of 4 inches in some cases, and by employing a solid central portion of 1.5 inches span with  $1/4$ -inch segments extending on either side for  $3/4$  inch in other tests; an 0.015-inch thick HE layer covered the central 2-inch span in all cases, and was separated from the timepiece segments by a 0.055-inch thick polyethylene sheet. The velocities imparted to these pellets upon HE detonation were determined photographically, and revealed that (to the resolution afforded by  $1/4$ -inch-span segments) the imparted velocity distribution was very nearly a square wave. A normalized distribution of this imparted impulse is shown in Fig. 2.2.

It is seen that this spanwise distribution of imparted impulse differs somewhat from a square wave. Since in the explosive-loading experiments on beam and ring specimens, the HE thicknesses ranged from about 0.015 to 0.030 inch, one can employ the spanwise distribution data of Fig. 2.2 for all cases, without appreciable error [7]. Note also that the total imparted impulse is almost exactly that obtained by considering only that portion of the specimen covered by the HE layer, neglecting HE edge effects. That is, the impulse deficiency inboard of the edge of the HE layer is compensated for almost exactly by the impulse increment observed outboard of that edge.

#### 2.4 Material-Property Measurements

In order to restrict the data uncertainties insofar as feasible, measurements of the static uniaxial stress-strain properties of the test-specimen materials used in the present beam and ring experiments were made. In addition, some limited measurements of the dynamic stress-strain properties of most of these materials were also made by the Picatinny Arsenal. For continuity, these measurements are discussed herein briefly.

It is useful to recall that the 6061-T6 material was selected as behaving much like an elastic, perfectly-plastic, strain-rate insensitive material; the 2024-0 material was selected as being similar except that it exhibits considerable strain hardening; finally, the 1010 steel was chosen for its reputation as being significantly sensitive to strain rate.

#### 2.4.1 Static Properties

Tensile test specimens from each of the same material lots of 6061-T6 and 2024-0 aluminum and 1010 steel as used for the impulsively-loaded beam specimens were prepared, instrumented with four strain gages, and static tested to fracture in tension. The results of these tests together with approximate analytical fits to these data are given in Subsection 4.2.

For the single-ring specimens of 6061-T6 material, three types of tests were employed to obtain static stress-strain data. Two cylindrical specimens from this lot of material were each instrumented with eight Tatnall HE 141B strain gages oriented both axially and hoopwise [6], and were subjected to internal hydrostatic pressure such that the cylindrical specimen experienced essentially no axial stress until very large strains occurred. From the known dimensions of the specimen, internal pressure, and the measured strain, the hoopwise static stress-strain properties of this material could be determined. However, during testing of one of these two cylindrical specimens, the strain-gage bonds to the specimen failed; hence, the desired strain information at large values of strain to check the data obtained from the first specimen was lost. Because of the pressure of time and funds, a third hydrostatic cylinder test was not made. Instead, some supplementary tests were made.

These consisted of tensile-strain tests of axial test strips cut from a cylindrical specimen of this 6061-T6 material. The stress-strain results obtained were essentially identical to those obtained from the 6061-T6 beam samples, whereas the stress-strain curve obtained in the hoopwise direction

from the hydrostatic cylinder tests fell somewhat below those data but did not extend to strains much above yield.

The third set of ring-specimen tests consisted of cutting a 6061-T6 ring to produce several hoopwise specimens, rolling them flat, instrumenting and tensile testing them to fracture. In spite of the work hardening to which these specimens were subjected during flattening in preparation for tensile testing, the hoopwise stress-strain data obtained (see Subsection 4.2) were in close agreement with that obtained in the "axial specimen" tests.

#### 2.4.2 Dynamic Properties

Since the explosively-loaded test specimens underwent severe transient responses, the material at various given locations within each test specimen experienced a range of strain rates. Should the mechanical stress-strain properties of the material be significantly affected by the rate of straining (instantaneous or "cumulative"), the details of the dynamic response of the structure would be altered; whether one can detect such strain-rate consequences depends upon the type and resolution of the dynamic response measurements made for a given experiment, and the design of that experiment as well. For the present structural response experiments, the transient deflections observed are the consequence of cumulative averaged effects of response of many material elements over a wide spectrum of strain rate in the structure; therefore, unless the material is extremely sensitive to strain rate, distinctive strain-rate-influenced structural response should not be expected to be observed. To some extent this averaging effect will also apply to

measurements of dynamic strain itself on the model, but higher resolution is afforded.

In view of these considerations, some limited measurements of strain rate effect on the uniaxial stress-strain properties of 1010 steel and of 2024-0 and 6061-T6 aluminum beam samples were made by the Picatinny Arsenal, using a pneumatic-hydraulic Hesse-Eastern dynamic tensile loading device [8]. Strain gages placed on each side of the test specimen were measured simultaneously on oscilloscopes operated at calibrated sweep rates. Oscilloscope-recorded measurements from a load cell mechanically in a series with the dynamic test beam coupon of material provided the load time history to which the specimen was subjected. This arrangement is depicted schematically in Fig. 2.3. The results obtained are discussed in Subsection 4.2.

These dynamic material property tests have been described as limited -- in the sense that the feasible range of strain rates extended up to only about 15 inches per inch per second which is far below the maximum local strain rates (about 3000/in/in/sec.) experienced by the explosively-loaded test specimens. Clearly, more extensive strain rate data are desirable; however, these experiments together with other similar data in the literature enable a reasonable appraisal of this effect to be made with respect to strain and deflection response of impulsively-loaded structures.

## SECTION III

### REVIEW OF PRESENT THEORETICAL METHOD AND ITS RESPONSE-PREDICTION FEATURES\*

#### 3.1 Introduction

This section of the report is devoted to a concise review of the elastic-plastic theory given in References 3 and 4 (and to some recent additions) for predicting elastic-plastic large dynamic and permanent deformations of two-dimensional structures such as beams and rings, and of shells of revolution which are restricted to deform in an axisymmetric fashion. The casting of this theory into finite-difference form leads to a dynamic model whose features are discussed and illustrated in detail. The important role of material stress-strain properties is discussed, and the consequences of employing various approximate representations for these elastic, plastic, strain-hardening, and strain-rate properties are illustrated.

Permanent plastic deformations of simple structures under high-intensity impulsive loadings have been analyzed by the so-called rigid-plastic analysis. In the case of simple beams, closed-form analytical solutions have been obtained [1, 2]. Applications to rings, curved beams, and circular plates also have been made [9-11]. In most cases, however, the solution of the resulting nonlinear differential equations still must rely on numerical methods.

- - - - -

\* Reference 4 contains an abbreviated version of the contents of this section.

The rigid-plastic analysis, strictly speaking, is applicable only to problems for which the initial kinetic energy is much higher than the elastic energy. This condition, of course, cannot be realized in most practical problems. Furthermore, recent investigations of beams have indicated appreciable discrepancies between rigid-plastic theory and experiments [12]. These discrepancies have been attributed largely to the effects of strain rate on the yield stress of the structural material. The rigid-plastic analysis is also in error for materials that exhibit appreciable strain-hardening in the plastic range. The existing dynamic analyses of rigid-plastic structures also are limited to cases involving small deflections. When large-deflection effects are taken into account, a rigid-plastic analysis becomes much too complicated; as a result, numerical analysis must be employed.

The present proposed method for dynamic analysis of shells is a general numerical method. It takes into account the effects of elastic-plastic or elastic-strain hardening behavior, strain rate, and large deflections.

Since the prediction of large degrees of dynamic structural response and permanent deformation is desired, the theoretical analysis must account for large deformations as well as elastic and inelastic material behavior. The present analysis, described in detail in Reference 3, accounts for these effects but neglects the effects of rotary inertia and transverse shear deformations and is restricted accordingly. It will be seen that a forcing function of arbitrary distribution and time history can be accommodated readily.

### 3.2 Review of Theory Employed Herein

#### 3.2.1 Two-Dimensional Structures

##### Equations of Motion

Figure 3.1 illustrates the internal and external forces acting upon a deformed element of length  $ds$  of a two-dimensional structure. The internal forces consist of moments, axial forces, and shear forces normal to the centroidal axis of the structure. The external forces may be considered to consist of inertia forces and forces externally applied normal and tangential to the exposed surfaces; these may be expressed in terms of convenient components.

The differential equations of dynamic equilibrium of this structural element in the  $y$  and  $z$  directions, respectively, are

$$\frac{\partial}{\partial s}(N \cos \theta) - \frac{\partial}{\partial s}(Q \sin \theta) + F_y - m\ddot{v} = 0 \quad (1)$$

$$\frac{\partial}{\partial s}(N \sin \theta) + \frac{\partial}{\partial s}(Q \cos \theta) + F_z - m\ddot{w} = 0 \quad (2)$$

where  $m = m(s)$  is the mass per unit length,  $\theta$  is the slope of the structure  $= \sin^{-1}(\partial w / \partial s)$ ,  $(\ddot{\phantom{x}})$  denotes partial double differentiation with respect to time, and all other quantities are defined in Fig. 3.1.

The equation of moment equilibrium about an axis perpendicular to the  $yz$  plane is

$$\frac{\partial M}{\partial s} - Q = 0 \quad (3)$$

where rotary inertia has been neglected.

Equations corresponding to Eqs. (1-3) now will be written in finite-difference form. To do this it is convenient to consider the structure to be divided along its length into segments of initial length  $\Delta s_{i0}$ . Let stations along the structure be designated as ...  $s_{i-1}$ ,  $s_{i-1/2}$ ,  $s_i$ ,  $s_{i+1/2}$ ,  $s_{i+1}$ , etc., where the segment between stations  $s_{i-1/2}$  and  $s_{i+1/2}$  is termed the  $i^{\text{th}}$  segment and has a length  $\Delta s_i$ . The mass of segment  $i$  is  $m_i = m \Delta s_i$  and remains constant even if the length of the segment changes during the response due to straining along the axis of the structure. The dynamic equilibrium equation in the  $y$  direction for the  $i^{\text{th}}$  segment can be written as

$$\frac{N_{i+1/2} \cos \theta_{i+1/2} - N_{i-1/2} \cos \theta_{i-1/2}}{\Delta s_i} - \frac{Q_{i+1/2} \sin \theta_{i+1/2} - Q_{i-1/2} \sin \theta_{i-1/2}}{\Delta s_i} + F_{yi} - (m\ddot{v})_i = 0 \quad (4)$$

Multiplying through by  $\Delta s_i$  and setting  $m\Delta s_i = m_i$ , Eq. (4) becomes

$$N_{i+1/2} \cos \theta_{i+1/2} - N_{i-1/2} \cos \theta_{i-1/2} - Q_{i+1/2} \sin \theta_{i+1/2} + Q_{i-1/2} \sin \theta_{i-1/2} + F_{yi} \Delta s_i - m_i \ddot{v}_i = 0 \quad (4a)$$

Similarly, the dynamic equilibrium equation for the  $i^{\text{th}}$  segment in the  $z$  direction becomes

$$N_{i+1/2} \sin \theta_{i+1/2} - N_{i-1/2} \sin \theta_{i-1/2} + Q_{i+1/2} \cos \theta_{i+1/2} - Q_{i-1/2} \cos \theta_{i-1/2} + F_{zi} \Delta s_i - m_i \ddot{w}_i = 0 \quad (5)$$

Similar equations could be written for any other segment or subsegment.

Corresponding to Eq. (3), the finite-difference moment-equilibrium equation for the segment between stations  $i-1/2$  and  $i+1/2$  is

$$M_{i+1/2} - M_{i-1/2} - Q_i \Delta s_i = 0 \quad (6)$$

or, for the segment between stations  $i$  and  $i+1$ ,

$$M_{i+1} - M_i - Q_{i+1/2} \Delta s_{i+1/2} = 0 \quad (6a)$$

This moment equilibrium must hold, of course, for all segments and subsegments.

An inspection of the terms in Eqs. (4a), (5), and (6a), all of which must hold at all instants of time, indicates that these equations may be interpreted as describing a lumped-parameter model. This model is shown in Fig. 3.2 with quantities relabeled with whole rather than half indices for convenience. The model is seen to consist of concentrated masses connected by massless extensible links that remain straight between mass points; that is, for example, the axial forces acting on and between masses  $i-1$  and  $i$  both are inclined at angle  $\theta_i$  with respect to the horizontal. All bending is concentrated at the mass-point locations. The externally applied forces may be considered as being concentrated at each mass point, as shown.

For the relabeled lumped-parameter model shown in Fig. 3.2, the three previously discussed equilibrium equations are

$$N_{i+1} \cos \theta_{i+1} - N_i \cos \theta_i - Q_{i+1} \sin \theta_{i+1} + Q_i \sin \theta_i + F_{yi} [(\Delta s_i + \Delta s_{i+1})/2] - m_i \ddot{v}_i = 0 \quad (7)$$

$$N_{i+1} \sin \theta_{i+1} - N_i \sin \theta_i + Q_{i+1} \cos \theta_{i+1} - Q_i \cos \theta_i + F_{zi} [(\Delta s_i + \Delta s_{i+1})/2] - m_i \ddot{w}_i = 0 \quad (8)$$

$$M_i - M_{i-1} - Q_i \Delta s_i = 0 \quad (9)$$

In terms of the mass-point coordinates  $v, w$ , the link lengths and angles may be written as

$$\Delta s_i = [(\nu_i - \nu_{i-1})^2 + (w_i - w_{i-1})^2]^{1/2} \quad (10)$$

$$\sin \theta_i = (w_i - w_{i-1}) / \Delta s_i \quad (11)$$

$$\cos \theta_i = (\nu_i - \nu_{i-1}) / \Delta s_i \quad (12)$$

The finite-difference equations (7-9), which approximate Eqs. (1-3), respectively, may be solved numerically for each mass point at successive instants of time  $t_j$ . Let it be assumed that, at time  $t_j$ , the following quantities already have been determined for all mass points of the structure:  $\nu_i$ ,  $w_i$ ,  $N_i$ ,  $M_i$ , and  $(\dot{\nu}_i$  and  $\dot{w}_i)$  if desired. Thus, Eqs. (10-12) can be used to calculate  $\Delta s_i$ ,  $\sin \theta_i$ , and  $\cos \theta_i$  for all links. Equation (9) then permits the determination of all  $Q_i$ . Then, if the  $F_y$  and  $F_z$  are given at time  $t_j$ , Eqs. (7) and (8) can be used to calculate  $\ddot{\nu}_i$  and  $\ddot{w}_i$  for all mass points at time  $t_j$ . Finally, since one may write, in general,

$$\ddot{x}_j = \frac{[(x_{j+1} - x_j)/\Delta t] - [(x_j - x_{j-1})/\Delta t]}{\Delta t} = \frac{x_{j+1} - 2x_j + x_{j-1}}{(\Delta t)^2} \quad (13)$$

the mass-point locations  $v_i$  and  $w_i$  at time  $t_{j+1} = t_j + \Delta t$  may be written as

$$v_{i,j+1} = \ddot{v}_{ij}(\Delta t)^2 + 2v_{ij} - v_{i,j-1} \quad (14)$$

$$w_{i,j+1} = \ddot{w}_{ij}(\Delta t)^2 + 2w_{ij} - w_{i,j-1} \quad (15)$$

Having  $v_{i,j+1}$  and  $w_{i,j+1}$  for all points, one then can determine (1) the increment in strain along the axis of each link, and (2) the increment in the angles between neighboring links. From this information, one can determine the increments,  $\Delta N_{i,j+1}$  and  $\Delta M_{i,j+1}$  or  $N_{i,j+1}$  and  $M_{i,j+1}$  for all links, and the calculation proceeds cyclically. Approximate determinations for these forces and moments are considered next.

### Idealized-Thickness Model

Of a number of possibilities for determining the internal forces and moments in the present numerical method, the method explored herein consists of idealizing the actual structural cross section as consisting of  $n$  discrete, evenly spaced, equal-area layers of material that can carry normal stresses. These layers are considered to be separated by material that cannot carry normal stresses but that has infinite shear rigidity. With this simplified model (see Fig. 3.2), the stress and strain in the structure can be defined by the individual normal stresses in the  $n$  layers, invoking the

assumption that plane sections remain plane throughout the response.

Considering, for the moment, structural material that is elastic-perfectly plastic, one might select the spacing between the discrete layers or areas and the size of the concentrated areas by requiring that the idealized model exhibit elastic extensional stiffness  $Ebh$  and elastic bending stiffness  $EI$  equal to those of the actual cross section of the two-dimensional structure. If the actual cross section were rectangular as shown in Fig. 3.2, requiring equal elastic extensional stiffness and taking equal Young's modulus leads to the following area  $A$  per "flange":

$$A = bh/n \quad (16)$$

Similarly, using equal Young's modulus and requiring equal elastic bending stiffnesses lead to the following spacings  $d$  between flanges:

$$d = h/\sqrt{n^2 - 1} \quad (17)$$

If, on the other hand, one requires that the idealized model exhibit the same fully plastic pure axial load-carrying ability and equal fully plastic pure moment-carrying ability as the actual structure, the following flange areas and spacings result:

$$A = bh/n \quad (18)$$

$$d = h/n \quad (19)$$

It is seen that these two sets of conditions lead to the same flange areas, and flange spacings tend to approach each other as the number of flanges is increased.

### Strain-Displacement Relations

The strain in the  $k^{\text{th}}$  flange located at a distance  $z_k$  (see Fig. 3.2) above the centroidal axis at mass point  $i$  may be expressed approximately as

$$\epsilon_{ik} = \frac{\Delta s_i - \Delta s_{i0}}{\Delta s_{i0}} - z_k \frac{\Delta \theta_i - \Delta \theta_{i0}}{\frac{1}{2}(\Delta s_{i+1,0} + \Delta s_{i0})} \quad (20)$$

where  $\Delta s_i$  is the length of the deformed link  $i$ , and  $\Delta \theta_i$  is the angle between the deformed links  $i$  and  $i+1$ . The index 0 refers to the undeformed position.

The first term in Eq. (20) is the axial strain in the  $i^{\text{th}}$  link, and the second term represents the bending contribution evaluated at the  $i^{\text{th}}$  mass point. For sufficiently small angles  $\Delta \theta$ , one may write

$$\Delta \theta_i \approx \sin \Delta \theta_i = \sin(\vartheta_{i+1} - \vartheta_i) = \sin \vartheta_{i+1} \cos \vartheta_i - \cos \vartheta_{i+1} \sin \vartheta_i \quad (21)$$

thus relating the strains directly to the quantities given in Eqs. (10-12) which are also used in the subsequent equilibrium equations.

Strictly speaking, both terms in Eq. (20) should be evaluated at the same point. This could be done, for example, by averaging the axial strain of the links  $i$  and  $i+1$ . For sufficiently small  $\Delta s$ , however, it is reasonable, alternatively, to use the axial strain in either of the neighboring links.

Having found the strains in all the flanges at time  $t_{j+1}$ , the strain increments can be determined by

$$\Delta \epsilon_{ik,j+1} = \epsilon_{ik,j+1} - \epsilon_{ikj} \quad (22)$$

and the associated flange stresses can be obtained from appropriate stress-strain relations. Once these stresses are found, the axial force and moment at each mass-point station may be computed from

$$N_{i,j+1} = A \sum_{k=-n/2}^{n/2} \sigma_{ik,j+1} \quad (23)$$

$$M_{i,j+1} = A \sum_{k=-n/2}^{n/2} \sigma_{ik,j+1} \zeta_k \quad (24)$$

where the idealized-thickness model is considered to consist of  $n$  flanges with areas concentrated at distances  $\zeta_k$  from the centroidal axis.

### Stress-Strain Relations

In order to describe the mechanical behavior of a given material adequately, a strain-hardening constitutive relation should, in general, be employed. A mechanical model describing such a behavior, has been suggested in Reference 13, pp. 6-8, and may readily be utilized in the present method.

Consider the idealized thickness model described previously. Each flange element representing part of the beam or ring element may be regarded as being composed of a number of perfectly plastic subflange elements with different yield limits successively taking part in the plastic yielding. These subflange elements (arranged in parallel) are all

subjected to the same longitudinal total strain while the axial loads carried by them must be added to furnish the axial load acting on the strain-hardening total flange element. The flange stress is then

$$\sigma = \frac{P}{A} = \frac{\sum_{i=1}^n P_i}{A} = \frac{\sum_{i=1}^n \sigma_i A_i}{A} \quad (25)$$

where  $n$  is the number of subflanges,  $A_i$  are the subflange areas,  $A = \sum A_i$  is the total flange area, and  $\sigma_i$  are the subflange stresses.

If  $\sigma_{0i}$  denotes the yield limit of each of the subflange elements,  $E$  is their common Young's modulus, and  $\epsilon$  their common strain, Eq. (25) appears, in general, in the following forms

$$\begin{aligned} \sigma &= \frac{E\epsilon A_1 + E\epsilon A_2 + \dots + E\epsilon A_n}{A} = \\ &= \left( \frac{A_1 + A_2 + \dots + A_n}{A} E \right) \epsilon = E\epsilon, \quad \left( 0 \leq \epsilon \leq \frac{\sigma_{01}}{E} \right) \end{aligned} \quad (26a)$$

$$\begin{aligned} \sigma &= \frac{\sigma_{01} A_1 + E\epsilon A_2 + \dots + E\epsilon A_n}{A} = \\ &= \frac{\sigma_{01} A_1}{A} + \left( \frac{A_2 + A_3 + \dots + A_n}{A} E \right) \epsilon, \quad \left( \frac{\sigma_{01}}{E} \leq \epsilon \leq \frac{\sigma_{02}}{E} \right) \end{aligned} \quad (26b)$$

$$\begin{aligned} \sigma &= \frac{\sigma_{01} A_1 + \sigma_{02} A_2}{A} + \left( \frac{A_3 + \dots + A_n}{A} E \right) \epsilon, \quad \left( \frac{\sigma_{02}}{E} \leq \epsilon \leq \frac{\sigma_{03}}{E} \right) \\ &\vdots \end{aligned} \quad (26c)$$

$$\sigma = \frac{\sigma_{01} A_1 + \sigma_{02} A_2 + \dots + \sigma_{0n} A_n}{A}, \quad \left( \epsilon \geq \frac{\sigma_{0n}}{E} \right) \quad (26d)$$

In relation (26a) all subflange elements remain elastic, in (26b) and (26c), part of the subflange elements yield, and in (26d) all subflange elements yield. Figure 3.3a shows the piecewise linear stress-strain diagram corresponding to relations (26) which describe the mechanical behavior of the flange element during the first loading.

Now consider an experimental stress-strain curve, and a flange element with a given area. In order to determine the subflange areas and yield limits, the stress-strain curve is approximated by a polygon defined by the coordinates of its corners  $(\epsilon_l, \sigma_l)$ . Since Eqs. (26) represent the equations of the polygon segments, the coefficients of  $\epsilon$  may be set equal to the corresponding slopes of the given polygonal stress-strain diagram

$$E_l = \frac{\sigma_l - \sigma_{l-1}}{\epsilon_l - \epsilon_{l-1}} \quad (27)$$

and one obtains

$$\begin{aligned} E_1 &= \frac{A_1 + A_2 + \dots + A_n}{A} E = E \\ E_2 &= \frac{A_2 + A_3 + \dots + A_n}{A} E \\ E_3 &= \frac{A_3 + A_4 + \dots + A_n}{A} E \\ &\vdots \\ E_n &= \frac{A_n}{A} E \\ E_{n+1} &= 0 \end{aligned} \quad (28)$$

Taking the differences of two neighboring expressions in (28) yields

$$\begin{aligned} E_2 - E_1 &= -\frac{A_1}{A} E \\ E_3 - E_2 &= -\frac{A_2}{A} E \\ &\vdots \end{aligned}$$

or in general

$$E_{l+1} - E_l = -\frac{A_l}{A} E \quad (29)$$

and hence the subflange areas

$$A_{\ell} = \frac{A}{E} (E_{\ell} - E_{\ell+1}) \quad (30)$$

It can be verified that expressions (30) add up indeed to the total flange area.

Examining the limits of strain in Eqs. (26) the subflange yield limits are immediately found to be

$$\sigma_{0\ell} = E \epsilon_{\ell} \quad (31)$$

In order to obtain a physically reasonable representation with this model, the approximate stress-strain diagram must be upwardly convex with non-negative slopes.

The perfectly plastic and linear strain-hardening constitutive relations employed in Reference 4 may be treated as special cases. In the case of perfect plasticity, there is only one subflange and in the case of linear strain-hardening there are two subflanges whereby the yield limit of the second subflange is taken sufficiently high so that the deformation in that subflange remains elastic.

Having established the model for the stress-strain behavior, one may proceed to determine the stress in each subflange. Assume that at time  $t_j$  all subflange stresses

$\sigma_{iklj}$  are known, and at time  $t_{j+1}$  the strain increments of all flange elements  $\Delta \epsilon_{ik,j+1}$  (Eq. (22)) are also known, then the subflange stresses at time  $t_{j+1}$  can be determined systematically as follows:

- (1) Start by taking a trial value (superscript t) of  $\sigma_{\ell,j+1}$  computed by assuming an elastic path

$$\sigma_{\ell,j+1}^t = \sigma_{\ell,j} + E\Delta\epsilon_{j+1} \quad (32)$$

- (2) Check the sign of  $\Delta\epsilon_{j+1}$  and proceed to see what the correct value of  $\sigma_{\ell,j+1}$  must be

$$\Delta\epsilon_{j+1} \begin{cases} > 0 \rightarrow \sigma_{\ell,j+1}^t \begin{cases} > \sigma_{o\ell} \rightarrow \sigma_{\ell,j+1} = \sigma_{o\ell} \\ \leq \sigma_{o\ell} \rightarrow \sigma_{\ell,j+1} = \sigma_{\ell,j+1}^t \end{cases} \\ = 0 \rightarrow \sigma_{\ell,j+1} = \sigma_{\ell,j+1}^t = \sigma_{\ell,j} \\ < 0 \rightarrow \sigma_{\ell,j+1}^t \begin{cases} \geq -\sigma_{o\ell} \rightarrow \sigma_{\ell,j+1} = \sigma_{\ell,j+1}^t \\ < -\sigma_{o\ell} \rightarrow \sigma_{\ell,j+1} = -\sigma_{o\ell} \end{cases} \end{cases} \quad (33)$$

For brevity, the subscript, k and i which refer to the total flanges and mass point stations, respectively, have been omitted in the above expressions.

Obviously, by employing this step-by-step procedure, the behavior of the mechanical model described by Eqs. (26) for the first loading is also valid for subsequent unloading and reloading.

Once the subflange stresses  $\sigma_{ik\ell,j+1}$  have been computed, the flange stresses  $\sigma_{ik,j+1}$  are obtained from Eq. (25), and the axial forces  $N_{i,j+1}$  and bending moments

$M_{i,j+1}$  from Eqs. (23) and (24) respectively. The cyclic time-wise calculation of the dynamic response of the structure as described in the paragraph following Eq. (12) may then proceed.

For cases in which the structural material exhibits significant strain rate sensitivity, an approximate accounting for this effect may be made. Although numerous strain rate laws have been proposed and discussed, there appears to be no universally validated and accepted description. In the case of a perfectly plastic material, for example, the following simple expression has been employed previously by Ting [14], among others.

$$\dot{\epsilon} = D \left( \frac{\sigma_y}{\sigma_o} - 1 \right)^p \quad (34)$$

Here the effect of strain rate is regarded as raising the yield limit  $\sigma_y$  above the static yield limit  $\sigma_o$ .  $D$  and  $p$  are material constants.

In the case of the present strain-hardening model, Eq. (34) is now applied to each perfectly plastic subflange element. Since the flange strain increment (Eq. (22)) and hence the strain rate is known at this stage of computation, the rate dependent subflange yield limit is readily obtained from

$$\sigma_{yl} = \sigma_{ol} \left( 1 + \left| \frac{\Delta \epsilon / \Delta t}{D} \right|^{\frac{1}{p}} \right) \quad (35)$$

and subsequently replaces the static yield limit in relations (33).

The family of stress-strain curves for different constant strain-rates is shown in Fig. 3.3b. The construction is seen to be very simple: segments belonging to the same subflange are parallel because the expressions for the slopes (28) do not contain the yield limits, and corresponding intersections lie on rays going through the origin because, for a constant strain rate, the corresponding yield limits (Eq. (35)) and hence the strain limits (Eq. (31)) are raised by the same ratio.

### Energy Distribution in the System

The energy theorem for a mechanical system states that the increase of the kinetic energy within an arbitrary time interval is equal to the total work done by the external and internal forces acting on and in the system during that time interval. For the present purpose it can be written as

$$T - T_0 = W_e + W_i \quad (36)$$

where  $T$  is the kinetic energy at an arbitrary time  $t$  of the dynamic response,  $T_0$  is the initial kinetic energy,  $W_e$  is the work done by the external forces, and  $W_i$  is the work done by the internal forces.

For an elastic-plastic structure, the work of the internal forces can be expressed by

$$W_i = - (U + W_p) \quad (37)$$

where  $U$  is the elastic strain energy at time  $t$ , and  $W_p$  is the mechanical work dissipated during plastic flow, henceforth referred to as plastic energy. Substituting Eq. (37) into

Eq. (36), and rearranging terms gives

$$T_o + W_e = T + U + W_p \quad (38)$$

For the cases considered in this report,  $W_e$  vanishes because there are no applied loads and the external reactions do no work. Thus, one obtains

$$T_o = T + U + W_p \quad (39)$$

which means that the initially imparted kinetic energy is subsequently partitioned among kinetic, elastic, and plastic components.

The kinetic energy for beams and rings is

$$T = \frac{1}{2} \sum_i m_i (\dot{v}_i^2 + \dot{w}_i^2) \quad (40)$$

and the total elastic strain energy appropriate to the strain-hardening model adopted in this report is obtained as the sum of the contributions of all the subelements in all the flange elements at all mass point stations. It can be written as

$$U = \sum_i \sum_k \sum_l \frac{\sigma_{ikl}^2 A_l \Delta s_{io}}{2E} = \frac{1}{2E} \sum_i \Delta s_{io} \sum_l A_l \sum_k \sigma_{ikl}^2 \quad (41)$$

where the summations are taken over the mass points  $i$ , flanges  $k$ , and subflanges  $l$ .

At any time of the response, the kinetic energy (40) and the elastic energy (41) can be evaluated and the plastic energy  $W_p$  can then readily be obtained from Eq. (39).

Another means to determine  $W_p$  is furnished by Eq. (37). But, because of the plastic deformation present, it would require a timewise step-by-step evaluation of the work of the internal forces  $W_i$  using the instantaneous stresses and strain increments along the response.

The plastic energy  $W_p$  represents the mechanical work dissipated into heat and, therefore, is lost to the system. Also lost is that portion of elastic strain energy  $U$  which cannot be recovered as kinetic energy, after the structure has shaken down to a purely elastic response; this represents trapped elastic energy.

#### Boundary Conditions

Since the beams and rings dealt with in this report all contain an axis of symmetry with respect to both geometry and loading, and hence with respect to the motion, only one half-span of the structure need be considered in the calculation. Referring to Fig. 3.4a, the following appropriate symmetry conditions for the quantities defined in Fig. 3.2 can be established:

$$\begin{aligned} Q_i &= 0 \\ \sin \theta_i &= 0 \\ \cos \theta_i &= 1 \\ \Delta s_i &= 2v_i \end{aligned} \tag{42}$$

Note that the first mass point is assumed to be located half a link length off center.

If the mass point representing the end element of the half-span is labeled  $n$ , the free-end conditions become (see Fig. 3.4b)

$$\begin{aligned}
N_{n+1} &= 0 \\
Q_{n+1} &= 0 \\
\Delta\theta_n &= 0
\end{aligned}
\tag{43}$$

The last condition automatically causes the end moment  $M_n$  to be zero\*.

The present numerical step-by-step procedure allows one to treat the kinematic constraints -- such as boundary conditions -- imposed on the structure in a relatively simple fashion: the forward positions of all the mass points are calculated according to the equilibrium equations (7) and (8). This is done for the sole purpose of being able to apply the same equations to every mass point, thus preserving the cyclic, time-saving nature of the calculation. The forward positions of the restrained mass points calculated in the above manner are naturally meaningless. The forward positions of these particular restrained points are thus recalculated on the basis of the appropriate kinematic constraints. For instance, if a point of a beam is not free to move, the calculated position of this point is disregarded and the "new" position which the point occupies is simply its old position.

For a horizontally clamped end, one may write (see Fig. 3.4c)

- - - - -

\* In the case of the shell of revolution,  $M_n$  is equal to zero, but  $\Delta\theta_n$ , in general, is not.

$$\begin{aligned}
\sin \theta_{n+1} &= 0 \\
\cos \theta_{n+1} &= 1 \\
w_n &= 0 \\
\Delta s_{n+1} &= 2(v_c - v_n) \\
\Delta \theta_{n+1} &= \Delta \theta_n
\end{aligned}
\tag{44}$$

The third condition prevents the mass point  $n$ , adjacent to the fixed wall, from moving vertically but not horizontally (zero deflection and zero slope). The last two conditions are needed to obtain the axial force at the edge,  $N_{n+1}$ , which in turn restrains the horizontal motion of the mass point  $n$  by means of the dynamic equilibrium equations. Note that the shear force,  $Q_{n+1}$ , can be given an arbitrary value, since it influences only the vertical motion which is subsequently annulled by the third condition. Clamped ends in a slanted position may be treated similarly.

The ordinary simple-support condition of a beam (Fig. 3.4d) is obtained by allowing the mass point connected with the support to move longitudinally but not laterally.

If the deformation is not too large, it can be expected that this simple support condition is adequate to simulate the fixed roller support that is used in the experiments for the explosively-loaded beams (see Fig. 2.1b). A better representation should be achieved by allowing the beam to slide between two pairs of fixed knife edges. Figure 3.4e illustrates how the forward position of the link containing the support is recalculated to simulate a sliding through the knife edges: in addition to being stretched, the link translates

parallel to its instantaneous axis and rotates into a position parallel to the unrestrained forward position. How the deflection of the beam is affected by the two different simple-support conditions will be seen in Section IV.

In the case of a ring, a second symmetry condition at the other end of the half-ring is needed. It can be written as

$$\begin{aligned} Q_{n+1} &= 0 \\ \sin \vartheta_{n+1} &= 0 \\ \cos \vartheta_{n+1} &= -1 \\ \Delta s_{n+1} &= 2r_n \\ \Delta \vartheta_{n+1} &= \Delta \vartheta_n \end{aligned} \tag{45}$$

#### Initial Conditions

In order to commence the numerical step-by-step procedure, appropriate initial conditions must be established first.

An impulsive loading applied to the structures is best described in terms of an initial velocity distribution. Thus, with the position of the undeformed structure defined by the coordinates of the mass points  $(v_{i0}, w_{i0})$ , and with the velocity distribution defined by the velocities of the mass points  $(\dot{v}_{i0}, \dot{w}_{i0})$  known at time  $t_0$ , the positions of the mass points at time  $t_1 = t_0 + \Delta t$  can be evaluated

$$v_{i1} = v_{i0} + \dot{v}_{i0} \Delta t \tag{46}$$

$$w_{i1} = w_{i0} + \dot{w}_{i0} \Delta t$$

and the general cyclic procedure may then begin.

If the structure is set in motion by applied loads of finite value (step function) the acceleration of each mass point is known, namely

$$\ddot{v}_{i0} = \frac{F_{yio}(\Delta s_{i0} + \Delta s_{i+1,0})/2}{m_i} \quad (47)$$

$$\ddot{w}_{i0} = \frac{F_{zio}(\Delta s_{i0} + \Delta s_{i+1,0})/2}{m_i}$$

where the loads are written in the forms as given in Eqs. (7) and (8)

Applying Eq. (14) at  $j = 0$  one obtains

$$v_{i1} = \ddot{v}_{i0}(\Delta t)^2 + 2v_{i0} - v_{i,-1} \quad (48)$$

From the initial velocity condition

$$\dot{v}_{i0} = \frac{v_{i1} - v_{i,-1}}{2\Delta t} = 0 \quad (49)$$

it follows that  $v_{i,-1} = v_{i1}$ , and Eq. (48) becomes

$$v_{i1} = v_{i0} + \frac{1}{2} \ddot{v}_{i0}(\Delta t)^2 \quad (50a)$$

Similarly,

$$w_{i1} = w_{i0} + \frac{1}{2} \ddot{w}_{i0}(\Delta t)^2 \quad (50b)$$

Equations (50) include the case of a forcing function of zero initial value in which case  $\ddot{v}_{i0} = \ddot{w}_{i0} = 0$ .

### Symmetric Motion of a Free Ring

The symmetric motion of a free ring (or beam) subjected to applied loads is conveniently referred to a translating coordinate system whose origin coincides with the center of mass of the ring at any instant of time. The differential equations of motion must then be modified to include the additional (fictitious) forces of relative motion, namely the centrifugal force and the Coriolis force. The Coriolis force, in this case, vanishes since the coordinate frame does not rotate.

If the z axis is the axis of symmetry, the two components of the centrifugal force acting on each mass point are

$$\sum_{y_i} = -m_i \ddot{v}_{cm} = 0 \quad (51)$$

$$\sum_{z_i} = -m_i \ddot{w}_{cm}$$

where  $(\ddot{v}_{cm}, \ddot{w}_{cm})$  denotes the acceleration of the center of mass which is moving with the coordinate frame. The y component is zero because of symmetry. The acceleration of the center of mass is related to the external forces by means of the momentum theorem

$$\ddot{w}_{cm} = \frac{\sum_i F_{zi} (\Delta s_i + \Delta s_{i+1}) / 2}{\sum_i m_i} \quad (52)$$

and the centrifugal force term which must be added to the left-hand side of Eq. (8) becomes

$$\sum_{z_i} = -\frac{m_i}{\sum_i m_i} \sum_i F_{zi} (\Delta s_i + \Delta s_{i+1}) / 2 \quad (53)$$

where the summations are taken over the half ring.

In the case of an impulsively-loaded ring (initial velocity distribution), the external forces and with them the centrifugal forces vanish, and the center of mass moves at uniform velocity  $\dot{w}_{cm}$  equal to: (z component of total impulse)/(total mass of ring).

The initial conditions given previously must also be modified to account for the relative motion. If primes refer to the relative motion, Eqs. (46) are replaced by

$$v'_{i1} = v'_{i0} + \dot{v}'_{i0} \Delta t = v_{i0} + \dot{v}_{i0} \Delta t \quad (54)$$

$$w'_{i1} = w'_{i0} + \dot{w}'_{i0} \Delta t = w_{i0} + (\dot{w}_{i0} - \dot{w}_{cm0}) \Delta t$$

where

$$\dot{w}_{cm0} = \dot{w}_{cm} = \frac{\sum_i m_i \dot{w}_{i0}}{\sum_i m_i}$$

and Eqs. (50) by

$$v'_{i1} = v'_{i0} + \frac{1}{2} \ddot{v}'_{i0} (\Delta t)^2 = v_{i0} + \frac{1}{2} \ddot{v}_{i0} (\Delta t)^2 \quad (55)$$

$$w'_{i1} = w'_{i0} + \frac{1}{2} \ddot{w}'_{i0} (\Delta t)^2 = w_{i0} + \frac{1}{2} (\ddot{w}_{i0} - \ddot{w}_{cm0}) (\Delta t)^2$$

where  $\ddot{v}_{i0}$ ,  $\ddot{w}_{i0}$  are given by Eqs. (47), and  $\ddot{w}_{cm0}$  by (52) applied at  $j = 0$ .

The form of the energy equations, (38) and (39), is not affected by the relative motion. The kinetic energy now contains the relative velocities, and the work of the external forces the relative displacements. The centrifugal forces must also be counted as external forces. Their work, however, vanishes since the reference frame is centered on and moves with the center of mass of the ring.

### 3.2.2 Axisymmetric Shells

#### Equations of Motion

Figure 3.5a shows a shell of revolution defined by the curvilinear coordinates  $s$  and  $\varphi$ . The location of any point on the meridian can be determined by the two coordinates  $r$  and  $z$ . On the element of the shell shown in Fig. 3.5b, there are two tangential stress resultants  $N_\theta$  and  $N_\varphi$ , a transverse stress resultant  $Q_\theta$ , and two stress couples  $M_\theta$  and  $M_\varphi$ . The equations of equilibrium for large deflections of shells are

$$\frac{\partial}{\partial s}[N_\theta r \cos \theta] - \frac{\partial}{\partial s}[Q_\theta r \sin \theta] - N_\varphi - mr\ddot{r} = 0 \quad (56)$$

$$\frac{\partial}{\partial s}[N_\theta r \sin \theta] + \frac{\partial}{\partial s}[Q_\theta r \cos \theta] - mr\ddot{z} = 0 \quad (57)$$

$$\frac{\partial}{\partial s}[M_\theta r] - M_\varphi \cos \theta - Q_\theta r = 0 \quad (58)$$

where  $m$  is the mass of the shell per unit area, and  $\theta$  is the angle of inclination of the element with respect to the  $r$  direction.

Equations corresponding to Eqs. (56-58) can be written in finite-difference form in the same manner as for the two-dimensional structures. These equations again can be interpreted as describing a lumped-parameter model consisting of rings connected by weightless frustums. The thickness of the shell also is idealized by  $n$  discrete layers of material that can carry normal stresses in the planes parallel to the tangential plane of the shell surface, whereas the material connecting these layers cannot carry normal stress but has infinite shear rigidity.

### Yield Condition and Flow Rule

The strain-hardening model, previously outlined for uniaxial stress can readily be extended [15] to include plane stress used in shell theory: each layer element representing part of the shell element may be regarded as being composed of a number of perfectly plastic sublayer elements successively taking part in the plastic yielding. These subelements obey, for example, the Mises-Hencky yield condition with different yield limits, and are all subjected to the same total strain. Written for the  $\ell^{\text{th}}$  sublayer, the yield condition reads

$$\sigma_{\phi\ell}^2 - \sigma_{\phi\ell}\sigma_{\theta\ell} + \sigma_{\theta\ell}^2 = \sigma_{o\ell}^2 \quad (59)$$

where  $\sigma_{\phi\ell}$  and  $\sigma_{\theta\ell}$  are the principal stresses, and  $\sigma_{o\ell}$  is the sublayer yield stress in simple tension obtained from a polygonal approximate stress-strain curve as described earlier.

The numerical procedure for solving the response of thin shells is similar to that for the two-dimensional structures. The increments in principal curvatures and midplane strains are expressed first in terms of the deflections in the  $r$  and  $z$  directions. The increments of total strains  $\Delta\epsilon_{\phi}$  and  $\Delta\epsilon_{\theta}$  in each layer then can be determined by imposing the Kirchhoff's assumption that normals to the midsurface of the shell remain normal to the midsurface of the deformed shell. In the plastic range, these increments in strain must be resolved into their elastic and plastic components, i.e.,

$$\begin{aligned} \Delta\epsilon_{\phi} &= \Delta\epsilon_{\phi\ell}^e + \Delta\epsilon_{\phi\ell}^p \\ \Delta\epsilon_{\theta} &= \Delta\epsilon_{\theta\ell}^e + \Delta\epsilon_{\theta\ell}^p \end{aligned} \quad (60)$$

where the elastic strain increments are given by

$$\Delta \epsilon_{\phi l}^e = (1/E)(\Delta \sigma_{\phi l} - \nu \Delta \sigma_{\theta l}) \quad (61)$$

$$\Delta \epsilon_{\theta l}^e = (1/E)(\Delta \sigma_{\theta l} - \nu \Delta \sigma_{\phi l})$$

and the plastic strain increments can be written according to the incremental strain theory of plasticity, as follows:

$$\Delta \epsilon_{\phi l}^p = \frac{1}{3}(2\sigma_{\phi l} - \sigma_{\theta l})\Delta \lambda_l \quad (62)$$

$$\Delta \epsilon_{\theta l}^p = \frac{1}{3}(2\sigma_{\theta l} - \sigma_{\phi l})\Delta \lambda_l$$

where  $\lambda_l$  is a measure of the plastic deformation. Equations (60) thus contain three unknown quantities:  $\Delta \sigma_{\phi l}$ ,  $\Delta \sigma_{\theta l}$ , and  $\Delta \lambda_l$ . A third equation required for the solution is the yield condition:

$$\begin{aligned} (\sigma_{\phi l} + \Delta \sigma_{\phi l})^2 + (\sigma_{\phi l} + \Delta \sigma_{\phi l})(\sigma_{\theta l} + \Delta \sigma_{\theta l}) + \\ + (\sigma_{\theta l} + \Delta \sigma_{\theta l})^2 = \sigma_{\theta l}^2 \end{aligned} \quad (63)$$

### 3.3 Effects of Dynamic Model Features and Material Properties on Predicted Structural Response

#### 3.3.1 Effects of Calculation-Model Parameters

In the present finite-difference method for calculating the elastic-plastic response of transiently-loaded simple structures, there are a number of calculation-model parameters which may be varied. Included among these parameters are space-mesh size, finite-difference time increment, number of flanges of the idealized thickness model, spacing of these flanges, etc. What values these parameters should be assigned in order to produce

reliable structural response predictions with a minimum of computational effort is the question to be examined in the following.

#### Effect of Space-Mesh Size (or the Number of Masses)

It is desirable to employ the largest space-mesh size feasible when calculating the dynamic elastic-plastic response of a given simple transiently-loaded structure, consistent with the prediction accuracy sought; this is desired in order to minimize computation time, other factors being equal. Since the response of the structure is critically dependent upon the intensity, distribution, and time history of the forcing function, space-mesh size selection for a given desired prediction accuracy depends also upon these factors. However, in the following, discussion will be limited to only one type of loading condition (a reasonably severe one), and one corresponding closely to certain experiments noted in Section II.

To illustrate the effects of space-mesh size on predicted structural response, consider two elastic, perfectly plastic beams: a beam clamped at each end, and a simply-supported beam, each with a 10-inch span between supports and each loaded impulsively over a spanwise segment centered at the midspan. The geometry and impulsive loading of the clamped and simply-supported beams are depicted schematically in Figs. 3.6 and 3.8, respectively. In each case a 4-flange calculation model with flange spacing  $d = h/4$  taken to correspond with the fully-plastic equivalence rule has been used to represent the beam cross section.

Referring to the clamped beam, 5, 10, 30, and 60 space meshes (or lumped masses) have been taken to occupy the region from the midspan to the support point; for these cases the ratio of calculation time interval to the critical time interval (see page 42) was kept constant. Figure 3.6 shows the corresponding time histories of the midspan deflection (mass point closest to the center) and Fig. 3.7 shows the spanwise deflection profiles at two instants of time. It is seen that there is not much difference in the deflection as the number of masses is increased from 10 to 60. Note that even the very coarse mesh of 5\* masses per semispan yields good results as long as the plastic hinge at the clamped edge has not developed yet. At a later stage (500 microseconds) with the rotation taking place at the last mass point, there are bound to be some differences since this point is constrained to stay on the horizontal (see boundary conditions). For this reason, and also for providing an adequate representation of the abrupt change of the initial velocity distribution at the edge of the explosive, 30 mass points have been chosen in the correlation calculations.

In the case of the simply-supported beam, calculations with 7.5, 12.5, 17.5, ..., 42.5, and 52.5 meshes between midspan and support have been made. Figure 3.8 depicts the corresponding time histories of the deflection of the mass point located one inch\*\* away from the midspan, and Fig. 3.9 depicts the deflection profiles at two instants of time. The results are practically identical between 12.5 and 22.5 masses but deviating not only with decreasing but also with increasing number of

- - - - -

\* This is the smallest number of masses that can be used to represent the beam-loading conditions of this example properly.

\*\* This is the shortest distance from midspan for which the above mesh series yields identical spanwise mass point positions.

masses. The first deviation is probably due to the error that is introduced by the finite-difference approximation of the differential equation, while it is surmised that the second deviation is mainly due to the accumulation of round-off errors caused by the huge amount of numerical operations inherent in the present method. In order to substantiate this surmise, some of the calculations have also been carried out with double precision carrying 16 figures instead of 8. Figure 3.10 shows the deflection of a selected mass point (one inch from midspan) versus the number of masses at three instants of time. The deflections are plotted using two scales, one corresponding to Figs. 3.8 and 3.9, and the other 25 times larger. As expected, double precision does not alter the results as long as either the number of masses or the response time is kept small, both cases involving only a restricted amount of numerical operations. For higher number of masses and longer response times, the double precision points show the expected tendency to stay on the horizontal while the single precision points gradually deviate. The number of masses chosen for the correlation calculations is 22.5.

#### Effects of Calculation Time Interval

The time interval  $\Delta t$  appearing in the numerical step-by-step procedure cannot be chosen arbitrarily. By means of numerical experiments, it has been demonstrated that the present large-deflection finite-difference equations for beams and rings are subject to two stability criteria. One pertains to the longitudinal vibration equation (simple wave equation), and the other to the lateral vibration equation for beams [16]. They can be combined as follows:

$$\text{If } \frac{h}{\Delta s} \begin{cases} \leq \left(\frac{h}{\Delta s}\right)^* & r \equiv \frac{\Delta t}{\Delta s} \sqrt{\frac{E}{\rho}} \text{ must be } \leq 1 \\ \geq \left(\frac{h}{\Delta s}\right)^* & r \text{ must be } \leq \frac{(h/\Delta s)^*}{h/\Delta s} \end{cases} \quad (64)$$

$(h/\Delta s)^* = \sqrt{3}$  if flange spacing corresponds to elastic equivalence  
 $(h/\Delta s)^* = \sqrt{3} \frac{n}{\sqrt{n^2 - 1}}$  if flange spacing corresponds to fully-plastic equivalence

where  $n$  is the number of flanges and  $\rho$  is the mass density.

There exists a thickness-to-mesh-size ratio,  $(h/\Delta s)^*$ , below which the longitudinal, and above which the lateral vibration criterion yields a smaller critical time interval. Figure 3.11 shows the dynamic responses of a simply-supported beam applying different time intervals to a fixed mesh size. It clearly demonstrates immediate divergence if the stability condition (in this particular case the longitudinal) is only slightly violated. Note also the deviation at a later stage of the response if the time interval is taken relatively small ( $r = .50$ ). This obviously means a loss of accuracy, and has also been observed on finite-difference solutions of the simple wave equation [16]. The time interval, therefore, should be kept as close as possible to the critical one.

#### Effect of the Number of Flanges of the Idealized-Thickness Model

Recall that the present analysis idealizes the thickness of the two-dimensional structure as consisting of concentrated equal-area discrete layers of material, or flanges, carrying

only normal stresses, separated at equal fixed distances by material which is infinitely rigid in shear, but incapable of carrying normal stresses. This model is consistent with the neglect of shear deformation and rotary inertia in the analysis, and is also convenient for applications in which the effects of a variety of stress-strain relations are to be employed. Alternatively, one could, in a similar fashion, evaluate the stresses at a number of points through the thickness and integrate these numerically through the thickness to obtain the necessary force and moment resultants.

To illustrate the effects of the number of flanges employed in this model, calculations of response of a clamped and a simply-supported beam subjected to impulse loading over a portion of the span of each have been conducted using 2-, 4-, 6-, and 10-flange models. The results for most of these calculations are shown in Figs. 3.12 and 3.13 in terms of midspan deflection time history. In all cases, the material was considered to be elastic, perfectly-plastic, and flange spacings according to the fully-plastic equivalence rule  $d = h/n$  were employed, where  $n$  is the number of flanges. Thirty masses per semispan were used for the clamped beam, and 22.5 for the simply-supported beam.

It is seen that there are fairly distinct differences between the responses for the 2-flange and 4-flange cases, but insignificant response differences between 4-flange cases and those with a greater number of flanges. Similar degrees of comparison were noted at other spanwise stations.

For reliable calculations, it is believed that at least four flanges should be used, but more than six will usually be unnecessary.

### Effect of Flange Spacing

It has been pointed out that the selection of flange spacing ( $d$ ) in the idealized-thickness model may be made in a number of ways. For example, one may choose the spacing of the equal-area flanges to be such as to provide the same elastic bending stiffness as the actual structure in which case  $d = h/\sqrt{n^2-1}$ , or such that the fully-plastic moment-carrying ability of the model equals that of the actual elastic, perfectly-plastic structure in which case  $d = h/n$ . If one expects essentially purely elastic response, the former spacing provides a model most nearly agreeing with the effective behavior of the structure. On the other hand, for a case in which the applied loading or impulse produces a very substantial amount of plastic response, the latter spacing is more appropriate. For intermediate degrees of response, an intermediate spacing may yield improved results compared with those obtained by the above extremes.

To illustrate flange-spacing effects on structural response, an impulsively-loaded, simply-supported beam made of elastic, perfectly-plastic material has been analyzed. A 4-flange (the smallest number of flanges which previous studies have shown to provide reliable results) and a 10-flange calculation model have been employed using the above spacings. The results are shown in Fig. 3.14 in terms of midspan deflection as a function of time. As one would expect, the deflections and the period of oscillation are larger for the model with the smaller elastic stiffness or spacing,  $d = h/n$ , which corresponds to that for fully-plastic equivalence. The responses of the two 10-flange models approach each other very closely. These models can therefore be regarded as correctly simulating the actual rectangular cross section. For this particular

loading which causes considerable plastic deformations, the 4-flange plastic equivalence model yields better results than the 4-flange elastic equivalence model.

Also shown in Fig. 3.14 is the corresponding purely elastic response of the beam. Here, of course, the elastic equivalence model, by definition, represents the actual cross section, independent of the number of flanges taken, and hence the smallest possible number (2) may be used. The response clearly demonstrates the presence of higher modes superposed on the fundamental, whereas plastic behavior (dissipation) appears essentially to eliminate the higher modes. Note also the complete reversal of the deflection to the negative side.

### 3.3.2 Effects of Stress-Strain Approximations

Since structural materials differ in their stress-strain properties, exhibiting various degrees of strain-hardening and strain-rate sensitivity, it is instructive to examine the effects of these features on the large-deformation dynamic response of simple structures. Further, various degrees of approximation can be used in accounting for these stress-strain properties in an analysis, and it is desirable to ascertain the response-prediction consequences of several typical approximations of this type.

To illustrate these effects, the responses of impulsively-loaded simply-supported and clamped beams of a significantly strain-hardening material, 2024-0 aluminum alloy, are shown in the following, using various approximations for the stress-strain properties of this material. In all of these cases, deflection-time histories and structural-deformation profiles are compared. Figures 4.2 and 4.3 depict the uniaxial static

tensile stress-strain properties of this material, as well as several approximate analytical fits. For convenience, these fits are designated fits, 4, 5, 6, and 9.

In all calculations, the stress-strain curve of the 2024-0 material was represented by an elastic segment having  $E = 10.9 \times 10^6$  psi and one or more of the segments shown in Figs. 4.2 and 4.3. Fit 5 represents a fairly close fit of the true curve for the region just beyond the initial linear portion of the stress-strain curve; thus, for responses extending only slightly beyond the elastic range, the use of this approximation would be expected to produce good response results. For larger responses, the use of fit 4 would be expected to be more appropriate. Also, an elastic, perfectly-plastic approximation, fit 6, the simplest possible representation, is given. Table 4.2 gives the pertinent segment fit data.

The usefulness of each of the above approximations is limited, and the bounds of applicability are only vaguely defined. Because of the ease with which still closer stress-strain fits can be handled with a digital computer, and through the use of the previously-discussed subflange concept, the stress-strain curve of the 2024-0 material was fitted by a total of 5 segments as shown in Fig. 4.3. The pertinent data for the 5 segments of fit 9 are given in Table 4.3.

To illustrate the influence of these four types of fits, the elastic-plastic responses of example impulsively-loaded, simply-supported and clamped beams have been calculated; these two types of structures were chosen to illustrate the importance of these stress-strain fits when widely different boundary conditions are employed. For the clamped beam, the midspan deflection as a function of time and the spanwise deflection at

the instant of maximum midspan deflection are shown in Fig. 3.15 for all four stress-strain fits. Similar data are shown in Fig. 3.16 for the simply-supported beam example. It is seen from these two figures that the response pertaining to fit 4 and that pertaining to the more realistic fit 9, approach each other very closely. Accordingly, fit 4, which is a linear strain-hardening approximation averaged over the range of strain occurring, can be expected to represent adequately the actual stress-strain curve of 2024-0 aluminum alloy and may be employed in the correlation calculations of Section IV in those cases for which the plastic strains are not too large. Considering the time history of the midspan deflection only, even the averaged perfectly-plastic fit 6 yields good results. With respect to the deflection profile, however, there is a significant difference between the perfectly-plastic fit on one side and the three strain-hardening fits on the other. The perfectly-plastic idealization shows a pronounced plastic hinge located at the center of the simply-supported beam, and at both the center and the clamped edge for the clamped 2024-0 beam, whereas the strain-hardening idealization exhibits a gradual bend. A similar deflection-profile difference has been noted in Reference 17 where measured permanent deformation profiles of impulsively-loaded aluminum alloy 1100-0 clamped circular plates have been compared with EL-PP and EL-SH five-segment fit calculations; the deflection-profile results from the complete EL-SH fit agree well with experiment.

An inspection of Figs. 4.1 and 4.4 indicates that the two other beam materials, 6061-T6 aluminum alloy and 1010 steel permit an even better linear strain-hardening approximation than 2024-0. Similar comparisons of the kind just outlined have, therefore, been omitted for these materials.

The manner of including approximate strain-rate effects in the present elastic-plastic dynamic response analysis has been discussed previously. Comparisons with rate independent predictions and experiments are shown in Section IV.

### 3.3.3 Effects on Energy Distribution in the System

A convenient means to gain some insight into a complicated structural response such as that of an elastic-plastic material is the timewise evaluation of the different energies occurring in the system, namely kinetic, elastic, and plastic energies. It also supplies some necessary checks of the analysis, for example, the fact that the plastic energy is not allowed to decrease.

It is emphasized at this point that the present analysis does not include any other damping mechanism than that due to plastic flow. Once the structure has shaken down to a purely elastic response, no further damping occurs.

For an impulsively-loaded, elastic, perfectly-plastic, simply-supported beam, the ratios of the different energies to the initially imparted kinetic energy, together with the midspan deflection are shown as functions of the time in Fig. 3.17. Figure 3.17a pertains to a 2-flange, and Fig. 3.17b to a 4-flange calculation model. A significant difference between the responses of these two models can be observed. In the case of 2 flanges, the plastic energy remains constant once the first deflection peak has been reached, that is, the beam has shaken down already at this point. The midspan deflection periodically approaches the height of its first peak, and the remaining energy alternates between the elastic and kinetic forms; note that the fundamental vibration mode prevails after the higher

modes have been essentially eliminated by dissipation. In the case of 4 flanges, additional damping develops just before maximum spring-back time, thus reducing the deflection maxima and the remaining elastic-kinetic energy. Note also that the minima of the elastic energy do not touch the zero line which means that a small portion is not recovered as kinetic energy. This nonrecoverable or trapped elastic energy is obviously due to residual stresses caused by the internal kinematic constraints "plane cross sections remain plane" if the number of flanges is increased from two to four or more.

For highly strain-hardening materials such as 2024-0 aluminum alloy, the trapped elastic energy can represent a larger portion of the total energy (order of magnitude 10 per cent). Here, it is attributed mainly to a microscopic effect inside the material structure which, in the present method, is simulated by the strain-hardening model. A demonstration of this effect on the response of clamped beams is given in Fig. 3.18, where Fig. 3.18a belongs to a perfectly plastic, and Fig. 3.18b to a typical strain-hardening material. Note in case b the considerable amount of elastic energy remaining at the cost of plastic energy.

Redundant structures like the above clamped beams give rise to a third, although minor, source of trapped elastic energy, even for the simple 2-flange perfectly-plastic calculation model. This results from the constraints on the system and may be visualized readily by observing that, for example, upon release of the clamped ends of a permanently deformed beam, some elastic energy of the system will be released and the structure will assume a different permanently-deformed shape.

## SECTION IV

### CORRELATION OF THEORY WITH EXPERIMENT

#### 4.1 Introductory Comments

This section is devoted to comparing the predictions of the present elastic-plastic dynamic response theory with a typical experimental result from each of 12 groups of experiments conducted in support of the present study by Picatinny Arsenal personnel under AFFDL-RTD sponsorship. In each of these groups, several experiments were performed to examine and demonstrate repeatability; these additional experimental results may be found in Reference 6\*. In addition, some comparisons between simplified theories and some experimental results are included in the present report.

Certain motivations for including these 12 groups of experiments should be cited, and were as follows. It was desired to obtain large dynamic response and permanent deformation data on well-defined simple models under accurately-known inputs so that a definitive evaluation of the prediction methods could be made; accordingly, explosively-loaded simple beams were chosen for use. In order to examine the influence of predominant bending or predominant stretching behavior, simple and clamped supports, respectively, were employed; to contrast this effect further, specimens of 1/8- and 1/4-inch thickness were used. In addition to these considerations, it was desired to study the effects of elastic, strain-hardening, and strain-rate properties of material upon the large dynamic response behavior;

- - - - -  
\* For numerous additional details of this extensive experimental program, the reader is also referred to Reference 6.

accordingly, (1) 6061-T6 aluminum alloy was chosen as behaving essentially in an elastic, perfectly plastic fashion, (2) 2024-0 as elastic, strain hardening, and (3) 1010 steel as an elastic, highly strain-rate sensitive material. Finally, explosively-loaded free and clamp-supported circular rings of 6061-T6 material were included as being a somewhat more representative structural element of aerospace vehicle interest.

In order to permit a definitive evaluation of the large dynamic-response prediction methods, not only must the input to and the geometric characteristics of the structure be clearly defined but also the mechanical properties of the specific materials comprising those structures must be known accurately. Thus, a series of static and dynamic stress-strain tests was conducted on specimens from each lot of material employed. The static tests were of adequate scope but the dynamic test conditions available were less extensive than desirable. Nevertheless, much useful stress-strain data were obtained and were subsequently employed in the present correlation studies by devising certain approximate analytical fits to these data.

In Subsection 4.2, therefore, the static and dynamic stress-strain experimental results and approximate fits to those results are discussed (see Tables 4.1-4.3). Subsections 4.3 through 4.6 are devoted to comparing experimental with theoretical dynamic deflection and strain data from the present elastic-plastic analysis for, respectively, 6061-T6 beams, 2024-0 beams, 1010 steel beams, and 6061-T6 circular rings; Table 4.4 identifies these specimens, their dimensions, and the pertinent HE loading data for each. In addition, Table 4.5 summarizes the features and parameters employed in the theoretical dynamic response predictions carried out to compare with each of these test specimens. Comparisons of some experimental

deformation data with the results of certain simplified theories are given in Subsection 4.7. Finally, Subsection 4.8 gives concise summaries of comparisons of predictions from the present elastic-plastic theory with the present experimental dynamic-response data.

## 4.2 Material Stress-Strain Descriptions

Table 4.1 identifies (a) the seven lots (I, II, ... VII) of material comprising the beam and ring models, (b) specific specimens of each material lot used in the static and dynamic stress-strain tests, and (c) the associated explosively-loaded beam and ring models whose results are correlated herein with theory. For use in the theoretical analysis, it is convenient to represent the static and dynamic stress-strain properties of these materials by analytical approximations. Accordingly, the measured stress-strain properties of these materials are now examined and the analytical fits selected are discussed.

### 4.2.1 Static Data

#### 6061-T6 BEAM MATERIAL

The 6061-T6 aluminum alloy beam material consists of material lots I, II, and III. Figure 4.1 shows the static tensile stress-strain results for two samples of each lot of material. For analytical purposes, it is convenient to approximate these characteristics by a bi-linear fit. Such fits: 1, 2, and 3 for material lots I, II, and III, respectively, are indicated by the dashed lines in Fig. 4.1, and the associated constants are listed in Table 4.2. It is seen that these bi-linear fits closely approximate these stress-strain properties except for a small region near the yield points. The

consequences of this discrepancy will be discussed later when the pertinent correlation calculation results are examined.

#### 2024-0 BEAM MATERIAL

The 2024-0 aluminum alloy beam material consists of material lots IV and V. Figure 4.2 shows the static tensile stress-strain results for samples of each lot of material. It is seen that the results from these two material lots are not significantly different from each other, and that the 2024-0 material exhibits a considerable degree of strain hardening. For this material, a simple bi-linear fit does not provide a good approximation of the data over the strain range of interest: 0 to about 3 percent and more. However, depending upon the average strain experienced by an explosively-loaded model in reaching its final deformation condition, one or another type of bi-linear approximation might be adequate to permit reasonably accurate dynamic and permanent deflection predictions. Therefore, three bi-linear fits: 4, 5, and 6 to these data have been made and are shown in Fig. 4.2; the associated constants are listed in Table 4.2. Fit 6, for example, might be an adequate approximation if large average strains were involved in a dynamic case. On the other hand, if only small postelastic average strains were involved, fit 5 might be better. For intermediate average strains, fit 4 might be more appropriate.

Through the use of the subflange model discussed in Subsection 3.2, one may approximate the stress-strain properties of the 2024-0 material as closely as one pleases by employing an adequate number of subflanges. Figure 4.3 demonstrates the fit (termed fit 9) achieved by using 4 subflanges; the appropriate fit data are listed in Table 4.3. It is seen that this five-segment (4 subflange) fit very closely approximates the

static stress-strain properties of the 2024-0 material.

#### 1010-STEEL BEAM MATERIAL

Material lot VI comprises the 1010-steel beam material. Its measured static tensile stress-strain properties are shown in Fig. 4.4. It is seen that the 1010 steel displays a degree of strain hardening lying between those of the 6061-T6 and the 2024-0 materials. Also, its strain hardening is nearly linear, much like that of the 6061-T6 material. Thus, a bi-linear fit (fit 7) to these data has been made and is shown in Fig. 4.4; the associated constants are listed in Table 4.2.

#### 6061-T6 RING MATERIAL

The explosively-loaded free and clamped ring specimens were taken from material lot VII. Since the stress-strain properties of interest are in the hoopwise direction, two cylindrical specimens (CYL 1 and CYL 2 of Fig. 4.5) were instrumented with strain gages, internally pressurized hydrostatically, and tested to failure; because of strain-gage bond failures at relatively small postelastic strains, the data from these tests were very limited, but are shown in Fig. 4.5. To supplement these results, axial specimens were cut from this cylindrical stock (lot VII), instrumented, and static tested; the results of this work are shown in Fig. 4.5 as specimens A, D, and E. These data closely resemble the 6061-T6 beam data of Fig. 4.1. In addition, ring specimens of material lot VII were cut, straightened, instrumented, and tensile static-tested in the "loop" direction; these results are given as specimens K, L, and M in Fig. 4.5. With the exception of two (high) points associated with specimen M, all of these data group fairly

closely, and have been fitted by a bi-linear approximation given as fit 8 in Fig. 4.5; the associated constants are listed in Table 4.2. One should note, however, that the work hardening incurred in flattening these hoop specimens may have altered the stress-strain curve somewhat compared with the unflattened material.

#### 4.2.2 Dynamic Data

##### 6061-T6 BEAM MATERIAL

Two specimens, G and J, of lot II of the 6061-T6 material were instrumented and loaded dynamically as discussed in Subsection 2.4.2. The time histories of (1) the stress  $\sigma$  deduced from the measured load histories and the known cross-sectional areas of these specimens and (2) the measured strain histories are given in part (a) of Fig. 4.6. Strain rates deduced from the measured strain histories are also shown in that figure. It is seen that the strain rates in these tests increase with time over the strain range of interest (up to roughly 4 to 5 percent), but are less than about 12 in/in per second. The outputs from the two pairs of strain gages separated axially by 3/4 inch gave similar but not identical histories. Since the load was sensed at only one location in the system, the strain data shown in part (a) of Fig. 4.6 consist of the average strain at a given instant from these two pairs of strain gages.

In part (b) of Fig. 4.6 the instantaneous dynamic stress-strain values are plotted as  $\sigma$  vs.  $\epsilon$ , and are compared with the previously-discussed static stress-strain data measured for this lot of material. For the strain rates experienced in these tests, there is no large increase in the stress level above the static-test results at a given value of strain.

Despite the lack of significant strain-rate sensitivity in these dynamic stress-strain data, it is interesting to examine whether or not a consistent set of material constants  $D$  and  $p$  are obtained for the simple strain-rate effect approximated by Eq. (34) and depicted in Fig. 3.3b. Accordingly, various pairs of points including strains from 0.2 to about 4 percent have been assessed to determine the implied values of  $D$  and  $p$  using data separately from both specimens G and J in conjunction with bi-linear fit number 2. Unfortunately, the values of  $D$  and  $p$  obtained varied rather widely. However, "average" values which permitted reasonably good data fits for dynamic specimens G and J are:  $D = 7,000 \text{ sec}^{-1}$  and  $p = 2.13$ ; values cited for aluminum alloy in Reference 14 are  $D = 6,500 \text{ sec}^{-1}$  and  $p = 4$ . The stresses predicted employing these two sets of "material constants" at several values of time (strain and strain rate) for specimen J are also shown in part (a) of Fig. 4.6. It is seen that the "predicted" stresses using  $D = 7,000 \text{ sec}^{-1}$  and  $p = 2.13$  compare somewhat better with this experimental stress history than by using  $D = 6,500 \text{ sec}^{-1}$  and  $p = 4$ . Note also that expanded scales have been used in these plots.

However, the present experimental data do not cover a large enough strain-rate range to include the maximum strain-rate conditions experienced by the explosively-loaded models included in the present test program. Therefore, it is presently possible to demonstrate strain-rate effects on dynamic structural response for this 6061 material only on an illustrative rather than on a definitive basis. This is discussed further in Subsection 4.3

## 2024-0 BEAM MATERIAL

Dynamic stress-strain tests were conducted on specimens 3B and 5B from lot IV, 2024-0 aluminum alloy, in a manner similar to the previously-discussed tests on the 6061-T6 material. Part (a) of Fig. 4.7 illustrates the stress, strain, and strain-rate histories for these two specimens, where again the strain and strain-rate data shown consist of the average data from the two pairs of strain gages spaced 3/4-inch apart along the specimen. In these tests, the data includes strains ranging up to about 3.5 percent, with strain rate increasing with increasing strain up to rates of about 8 in/in per second, which are still rather small compared with those of interest in the present impulsive-loading experiment.

Part (b) of Fig. 4.7 compares the static stress-strain data for this lot of material with instantaneous  $\sigma, \epsilon$  pairs for dynamic specimens 3B and 5B from part (a) of Fig. 4.7. It is seen that the "dynamic  $\sigma, \epsilon$  data" do not differ perceptibly from the static results for these small strain rates.

As a matter of curiosity, the "strain rate constants"  $D = 6,500 \text{ sec}^{-1}$  and  $b = 4$  reported in reference 14 for aluminum alloy were employed in Eq. (35) together with the present static five-segment fit 9 to compute predicted stress for specimens 3B and 5B at various instants (or combinations of  $\epsilon$  and  $\dot{\epsilon}$ ). These "predictions" are compared in part (a) of Fig. 4.7 with the measured stress history for specimens 3B and 5B. It appears that the assumed rate sensitivity is somewhat too large. The rate constants  $D = 7,000 \text{ sec}^{-1}$  and  $p = 2.13$  found herein for 6061-T6 material were also used to predict the stress histories for specimens 3B and 5B in conjunction with the five-segment fit 9; these results are also shown in Part (a) of Fig. 4.7, and are seen to agree somewhat better with these experimental results than do the former predictions.

## 1010 STEEL BEAM MATERIAL

Because of its reportedly high sensitivity to strain-rate, the 1010 steel is of much greater strain-rate interest than are the aluminum alloy materials. Accordingly, the Pica-tinny dynamic stress-strain measurements for this material are discussed in greater detail.

Several dynamic test specimens of 1010 steel were tested. The records of "measured stress" and measured strain for specimen 6 are shown in Fig. 4.8a, covering an extensive time period; subsequent figures of this type will be restricted to the early stress-strain and the "high" strain-rate portion of the records. Such "measured stress", measured strain, and computed strain-rate histories are shown in Figs. 4.8b and 4.8c for specimens 6 and 10, respectively. Again, it was observed that the strain histories from strain-gage pairs\* spaced 3/4-inch apart axially were somewhat different. The data shown in Figs. 4.8b and 4.8c for specimens 6 and 10, respectively, depict the average time histories of strain from the pairs of gages on each specimen. For these two cases also, the two strain traces from each specimen were somewhat different at a given instant.

Instantaneous stress-strain pairs from Figs. 4.8b and 4.8c are shown in Fig. 4.9 and are compared with the static stress-strain curve for this 1010 steel material.

By using data for each specimen at a variety of pairs of time, very extensive calculations were made to see whether or not material constants  $D$  and  $p$  could be deduced in conjunction

- - - - -  
\* At a given axial station of the specimen, axially oriented strain gages were placed on opposite sides of the specimen. These gages were connected to cancel out any bending contributions and to give average axial strain histories.

with bi-linear fit 7 for the 1010 steel material. Although these deduced values for  $D$  and  $p$  covered a wide range of values, the choice  $D = 40.4 \text{ sec}^{-1}$  and  $p = 5$  appear to give the best overall compromise; however, the resulting data fit is not very good. A more comprehensive fitting expression needs to be developed; to make this worthwhile, however, better quality data covering a wider strain-rate range would be needed.

In Fig. 4.9 the stresses predicted using these rate constants are compared with the measured time histories of stress for specimens 6 and 10, respectively. It is seen that the results using bi-linear fit 7 and the present pair of "constants":  $D = 40.4 \text{ sec}^{-1}$  and  $p = 5$  leads to rather unsatisfactory agreement with the measured strain histories.

Figure 4.10 depicts the present bi-linear static and dynamic stress-strain idealization for this 1010 steel, and also compares it with an example point from the present experimental data.

Finally, Fig. 4.11 shows the ratio of dynamic yield stress to static yield stress as a function of strain rate for the present 1010 steel and 6061-T6 aluminum alloy as well as similar data reported in References 14 and 18 for "mild" steel and 24ST aluminum alloy, respectively. After the dynamic  $\sigma, \epsilon$  data from the present study were analyzed to deduce "unbiased" strain rate constants, the strain-rate data of Reference 18 were analyzed in the present program and were found to be fitted very well over strains ranging from 2 to 14 percent and strain rates ranging up to  $10,000 \text{ sec}^{-1}$  with the strain-rate constants  $D = 12,000 \text{ sec}^{-1}$  and  $p = 3.23$ , using a static stress-strain curve defined by  $E = 10.5 \times 10^6 \text{ psi}$ ,  $\sigma_0 = 11,000 \text{ psi}$ , and  $E_p = 16,100 \text{ psi}$ . It is seen from Fig. 4.11 that the aluminum alloys are all very similar in their behavior. Since the Reference 18 data appear

to be essentially the best strain-rate data available and since the present 6061-T6 data fall reasonably close to the former data, some measure of added confidence in the present rate fits for the 6061-T6 data is afforded.

Thus, on the basis of these comparisons, it appears reasonable to use the results of the present simple strain-rate fitting procedure to account approximately for strain-rate effects in the present experiments on explosively-loaded beams. However, the present dynamic stress-strain measurements do not include large enough strain rates to cover those of interest for these impulsively-loaded beams. The "extrapolation" to higher strain rates, therefore, in the calculation of beam dynamic response is made with distinct reservations, although the favorable agreement with the Reference 18 data in Fig. 4.11 provides a reasonable degree of confidence.

#### 4.3 Beams of 6061-T6 Material

In order to avoid needless repetition during Subsections 4.3 to 4.6 of discussion of experimental-theoretical correlation of explosively-loaded beams and rings, some abbreviated terminology and discussion of certain features which are common to many of the experimental cases involved are given now.

As a matter of convenience for the saving of computer time, all experimental beam and ring cases were treated as symmetrical problems. Thus, only the beam semispan or ring semiperiphery and symmetrical loading were employed, with attendant symmetrical structural response. As noted in Subsection 3.3.1, the use of about 20 to 30 lumped masses per semispan permits a reasonably accurate accounting for the spanwise distribution of imparted velocity (and hence both impulse and initial kinetic

energy) to each specimen for the types and spanwise extents of impulsive loading employed in these experiments. Hence, in the interests of both accuracy and the saving of computer time, the number of lumped masses employed per semispan were: 22.5\* for all of the simply-supported beams, 30 for the clamped beams, and 30 or 31 for the ring models.

Based upon the studies discussed in Subsection 3.3.1 of the influence of the number of lumped area layers used in the idealized-thickness model, six layers or flanges were used in correlation calculation with but one illustrative exception (see Table 4.5). The smallest number of flanges that can be used meaningfully in this model is two, but the spacing of these flanges must be chosen in accordance with some rational rule such as: wholly-elastic or fully-plastic equivalence. Using these two extreme rules, the associated flange spacings approach each other as the number of flanges is increased. Increasing the number of flanges from two to four leads to distinct response differences, but increasing the number of flanges from four to six to ten leads to very little change in the results. In the interests of accuracy, conservatism, and minimum computer time, a six-flange representation has been employed in the main correlation calculations.

The inclusion of material stress-strain characteristics has been accomplished by using the bi-linear approximate fits to the present experimental stress-strain data; these bi-linear fits are listed in Table 4.2. However, the specific fit or fits used in correlation calculations for a given explosively-

- - - - -

\* For the portion of the beam from the midspan to one support; 4.5 additional masses represented the portion of the beam extending beyond the support.

loaded model are listed in Table 4.5. In nearly all cases, correlation calculations have been carried out in which the material has been treated as (a) elastic, strain-hardening (EL-SH) with the Table 4.2 and 4.3 fits and (b) elastic, strain-hardening, strain-rate sensitive (EL-SH-SR). Hereinafter, these abbreviations will be used in discussing the results.

Boundary conditions which can be employed in the present finite-difference method to analyze the explosively-loaded beams have been discussed in Subsection 3.2.1. For the clamped beams, the proper procedure is well-defined. However, for the "simply-supported" beams (see Fig. 2.1(b)), the actual beam-support condition appears to lie between the rolling simple support, Fig. 3.4(d), and the sliding simple support, Fig. 3.4(e). The former support condition is clear and unambiguous, and has been used for all of the simply-supported beam cases. For the latter type of support representation (i.e., SS-sliding), a reasonable scheme has been devised to approximate this; however, time has not permitted this scheme to be studied exhaustively to verify its reliability. Therefore, the SS-sliding boundary condition has been included only on a tentative illustrative basis as noted in Table 4.5.

In the following, therefore, the above motivation is not repeated when discussing each of the groups of experiments. Instead, attention will be called to the specific calculation parameters listed for each case in Table 4.5.

Returning specifically to the explosively-loaded beam specimens of 6061-T6 aluminum alloy, this material was chosen as one which behaves essentially in an elastic, perfectly-plastic manner. To produce predominant bending and predominant stretching behavior, simply-supported (SS) and clamped (C)

beams, respectively, were employed. These two types of cases are discussed separately in the following.

#### 4.3.1 Predominant Bending Cases: SS Beams

In this category two typical explosively-loaded 6061-T6 beams, 121 and 131, are examined.\* Their dimensions, weights, extent of HE coverage, and imparted impulse are given in Table 4.4. Dynamic response calculations have been carried out using: 22.5 masses per semispan, a six-flange and a two-flange thickness model, and the stress-strain properties shown in Table 4.5.

Figure 4.12 demonstrates comparisons between the time history of measured midspan front-edge beam deflection and theoretical two-dimensional deflection predictions for specimen 121. The measured deflection is represented by the circle symbols. Deflection predictions for the following cases are included:

- (a) 6-flange, EL-SH Rolling: ---
- (b) 6-flange, EL-SH-SR, Rolling,  $D = 6500 \text{ sec}^{-1}$ ,  $p = 4$ : —
- (c) 6-flange, EL-SH-SR, Rolling,  $D = 7000 \text{ sec}^{-1}$ ,  $p = 2.13$ :  
x
- (d) 6-flange, EL-SH-SR, Sliding,  $D = 6500 \text{ sec}^{-1}$ ,  $p = 4$ :  
— . —
- (e) 2-flange, EL-PP, Rolling: ———

Case (a) represents response predicted neglecting strain-rate effects. Cases (b) and (c) show responses including strain-rate effects using constants from Reference 14 and the present studies,

-----  
\* Hereinafter, the test specimens are referred to by the last number of the Picatinny identification code for each (see Tables 4.1 and 4.4).

respectively. It is seen that the inclusion of strain-rate effects leads to an effectively "stiffer" structure: the peak response is reduced and the response period is shortened. Also, the present rate fits, Case (c), lead to somewhat better results than do those of Case (b).

The influence of including a sliding support versus a rolling support may be seen by comparing Case (b) with Case (d). The sliding support condition leads to increased deflection compared with the rolling-support prediction. It is expected that the sliding support condition together with the rate constants of Case (c) would comprise the most realistic calculation at present and would produce a first-peak response about as large as that of Case (a). Finally, Case (e) represents the least refined calculation of this entire group -- using the minimum number of flanges (2) and treating the material as EL-PP with no rate sensitivity; however, while Case (e) is in best agreement with measured peak midspan deflection, it disagrees with experiment in the later stages of response.

From physical considerations, one would expect to observe best theoretical-experimental agreement with the 22.5m, 6f, EL-SH-SR, SS-sliding case where strain-rate constants obtained from the present (limited) tests are used. Whereas there is general agreement with respect to the time-history features of the midspan deflection response, the predicted amplitude is too small. The principal reasons for this discrepancy may include:

- (a) Too small an imparted impulse. Data from impulse calibration tests revealed mean deviations of about 3.5 percent and extreme deviations of -8 and +5.6 percent from the mean value:  $18.6 \times 10^4$  (dyne-sec)/gm.

- (b) The assumed strain rate effect may be too large. Since aluminum alloy is known [18, 19, 20] to be relatively rate insensitive and because of the limited scope and resolution of the present dynamic stress-strain tests, it is perhaps reasonable to neglect strain-rate effects for this material.

Figure 4.13 illustrates the beam deflection versus spanwise station at several instants of time: approximately 550, 1750, and 4425 microseconds after HE detonation for the 1/4-inch thick simply-supported 6061-T6 beam 121; predicted results are plotted for the print-out times which fell closest to the measurements reported. Front-edge deflection data measured from framing camera records are compared with two-dimensional deformation results predicted with a 22.5-mass, 6-flange, rolling-support model with (a) EL-SH and (b) EL-SH-SR ( $D = 6500 \text{ sec}^{-1}$ ,  $p = 4$ ) material behavior. At 550 microseconds, there is good deflection profile shape and magnitude agreement between experiment and both calculations. At 1750 microseconds, the experimental midspan deflection exceeds the EL-SH result by about 8 percent and the EL-SH-SR result by about 20 percent; the measured profile shape agrees slightly better with the EL-SH prediction. At 4425 microseconds, again good agreement exists between theory and experiment; in this case the measured profile shape (although exhibiting some asymmetry) is in somewhat better agreement with EL-SH-SR calculations.

The front-edge midspan deflection history of a similar but thinner (1/8-inch thick) simply-supported beam (131) is given in Fig. 4.14. Those measurements are compared with 22.5-mass, 6-flange, roller-support, EL-SH and EL-SH-SR predictions. Although the peak response predicted by EL-SH theory agrees better with experiment (i.e., 12 percent vs. 19 percent smaller)

the character of the deflection-time history and the time to peak response given by the EL-SH-SR calculation agrees better with experiment. Again, dynamic twisting of uncertain amount is present in the experimental data whereas the present calculations exclude this behavior. Note also in Fig. 4.14 the results of an illustrative 22.5-mass, 6f, EL-SH-SR, sliding-support calculation in which an imparted impulse 10 percent greater, than that listed in Table 4.4 and the strain rate fits  $D = 7000 \text{ sec}^{-1}$  and  $p = 2.13$  are used. In this case, there is better agreement between prediction and experiment with respect to peak amplitude, but the time to peak remains too great; the higher input, the latter strain-rate constants, and the sliding-support all tend to increase the peak response and the time to peak response. One can see also some mode-phasing differences between these two EL-SH-SR response results.

#### 4.3.2 Predominant Stretching Cases: Clamped Beams

Beams with fully-clamped ends experience predominant stretching compared with bending when the deflection exceeds a very small value; such cases are considered now. Beam specimens of 6061-T6 ("non-strain-hardening") material of 1/4- and 1/8-inch thickness were tested and analysed. Midspan deflection time histories are shown in Fig. 4.15 and 4.17 for 1/4-inch beam 111 and 1/8-inch beam 95, while spanwise deflection at various instants of time are shown in Fig. 4.16 for 1/4-inch thick beam 112. Finally, measurements and predictions of dynamic strain at several locations on 1/8-inch thick beams specimens 3 and 2 are shown in Figs. 4.18 and 4.19, respectively. It would have been desirable to compare simultaneous measurements of midspan deflection history, deflection profiles, and dynamic strain for cross-checking; however, such data are not available.

Nevertheless, it will be seen that reasonably good experimental-theoretical agreement has been achieved.

Figures 4.15 and 4.17 show that the peak value of the midspan deflection history predicted by EL-SH theory in each case agrees better with experiment than does the EL-SH-SR calculation. However, the details of the deflection (i.e., time to peak and shape) for the latter calculation show closer similarity to experiment than do those for the EL-SH case. Although the presence of dynamic twisting in the experiment may produce certain "peculiar distortions" of that time history, it is interesting to inquire whether an EL-SH-SR calculation modified to include the present rate fits  $D = 7000 \text{ sec}^{-1}$  and  $p = 2.13$  and an impulse increase of 10 percent will lead to near duplication of the measured midspan deflection history, as previous inquiries and arguments suggest. The results of these "modified EL-SH-SR calculations" are also shown in Fig. 4.15 where it is seen that very close theoretical-experimental agreement is achieved except for some phase difference which might be due to the presence of some dynamic twisting in the experiment.

Figure 4.16 compares measured spanwise deflection profiles for beam 112 at three instants of time with EL-SH and EL-SH-SR predictions. Note that there are certain distinctive differences between the profiles predicted by EL-SH and EL-SH-SR calculations. Also note that the measured deflections are those of the front edge of the beam (rather than the ideal two-dimensional value), and that these measured profiles, unfortunately, do not extend completely to the clamped ends. At 150 microseconds, the influence of the impulse explosively imparted to about the central 2-inch portion of the beam has not yet reached the clamped ends -- having traveled only to a station

about 3.5 inches from midspan; observe also that the EL-SH and EL-SH-SR profiles cross each other. At the two later times shown, these two profiles no longer cross, but the EL-SH deflection is larger than the EL-SH-SR deflection, as is to be expected on the basis of the Fig. 4.15 results. Because the data on the experimental profiles are incomplete, it is not possible to make an incisive appraisal of the EL-SH result versus the EL-SH-SR calculation from Fig. 4.16.

A better comparison is possible, however, through the use of a more sensitive indicator; namely, dynamic strain measurements at specific locations on a specimen, which is an "unintegrated quantity". Figure 4.18 shows comparisons between strains measured at several locations on both the top and bottom surfaces of beam 3 and results predicted by EL-SH and EL-SH-SR calculations (see Table 4.5). Similar results are shown in Fig. 4.19 for beam 2 which has undergone significantly larger strain than has beam 3. In essentially every case, it is seen that the EL-SH-SR theory is in best amplitude and shape agreement with measurements; there is, however, some phase difference (predicted peaks are too early) which could be accounted for largely by the use of strain-rate ( $D, p$ ) pairs 7000, 2.13 rather than 6500, 4 and a small increase in the imparted impulse. The superiority of the EL-SH-SR results compared with the EL-SH results is perhaps most evident in the large-strain case, Fig. 4.19, where strain rate effects would be expected to be the most pronounced.

#### 4.4 Beams of 2024-0 Material

The 2024-0 material was selected to provide dynamic large-response data on a material which exhibits a considerable amount of strain hardening, and to permit evaluating prediction methods designed to account for this effect. As before, predominant

bending (SS) and predominant stretching (clamped) cases were included. Only midspan deflection measurements are available for comparing with predictions.

#### 4.4.1 Predominant Bending Cases: SS Beams

In this category, two typical explosively-loaded 2024-0 beams, 119 and 134, are examined. Their dimensions, weights, extent of HE coverage, and imparted impulse are given in Table 4.4. Dynamic response calculations have been carried out using: 22.5 masses for the portion of the beam from midspan to one support, a 6-flange thickness model, and bi-linear stress-strain fit 4 (see Tables 4.2 and 4.5).

Figure 4.20 shows comparisons, for 1/4-inch thick beam 119, between the measured front-edge midspan deflection history and two-dimensional midspan deflections predicted from EL-SH and EL-SH-SR theory, where strain rate constants for the latter were assumed, for illustration, to be  $D = 6500 \text{ sec}^{-1}$  and  $p = 4$ . While these predicted deflection histories are similar to that which was measured, the predicted amplitudes are considerably below experiment. Certain reasons for this are discussed after Fig. 4.21 has been examined.

Figure 4.21 shows midspan deflection-history results for experiment and theory for 1/8-inch thick beam 134 which has undergone much larger deformations than beam 119. The theoretical calculations made use of a 6-flange thickness model, 22.5 masses per semispan, and stress-strain fit 4; in addition, the features included (a) EL-SH with rolling support, (b) EL-SH-SR with rolling support, and (c) EL-SH-SR with the beam allowed to slide freely over a fixed support. These three predicted results are shown in Fig. 4.21. As usual, it is seen that the inclusion of strain rate leads to a reduced deflection amplitude.

Note that the sliding-support condition, which corresponds more closely to the actual conditions present in the experiment, leads to a response which agrees considerably better with experiment both with respect to amplitude and response period than does the rolling-support EL-SH and EL-SH-SR calculations. There remains, however, some undesirable time history discrepancy between theory and experiment prior to the first peak; clear-cut reasons for this have not been established.

Returning to Fig. 4.20, one may now speculate reasonably that the discrepancy between EL-SH-SR theory and experiment may be explained largely by the fact that a rolling rather than the more-realistic sliding support condition was employed. Extrapolating roughly from the Fig. 4.21 results, it is estimated that the use of the sliding support for an EL-SH-SR calculation for beam 119 would result in a peak response of about 1.35 inches compared with the observed 1.6-inch value. Note also that the initial slope of the experimental midspan deflection versus time curve is steeper than every theoretical result. This feature suggests that the imparted impulse may have been greater than that estimated for these beams on the basis of the separate impulse-calibration experiments. This residual discrepancy is unresolved.

#### 4.4.2 Predominant Stretching Cases: Clamped Beams

The midspan deflection-history measurements for clamped beams 88 and 100 which were of 1/4- and 1/8-inch thickness, respectively, are given in Figs. 4.22 and 4.24, respectively.

Four theoretical results are shown for comparison with the beam-88 data in Fig. 4.22. Two EL-SH calculation results using fits 4 and 9, respectively, are shown as dash-dash and

dash-dot-dash curves; only an insignificant difference arises between these two predictions because of the relatively small average strain level involved. Similarly, two EL-SH-SR calculations result for strain rate (D,p) pairs of 6500,4 and 7000,2.13 are shown by the solid curve and the "x" symbol display, respectively. The latter result which makes use of strain-rate constants deduced from the present experiments demonstrates slightly better agreement with experiment than does the former EL-SH-SR result. In fact, the details of the midspan deflection response for the EL-SH-SR (7000, 2.13) case agree best with experiment; this may be fortuitous in part since the influence of dynamic twisting remains undefined. If one compares the initial slopes (velocities) of the experimental and predicted curves, one might suspect that the actual imparted impulse was larger than that obtained by calibration. Results obtained by using an adjusted 25 percent higher impulse are shown in Fig. 4.23. The theoretical curves are seen to follow the experimental points not only during the early phase, but also fairly well at later stages of the response.

Similar theoretical-experimental comparisons may be noted in Fig. 4.24 for 2024-O beam 100. Here again, the details of the EL-SH-SR result compare better with experiment than does the EL-SH case, where fit 4 is just as valid as fit 9 because of the relatively low level of plastic strain involved. Predicted peak responses for both cases are within 12 percent of the observed peak midspan deflection.

#### 4.5 Beams of 1010 Steel Material

Explosively-loaded 1010 steel beams have been included to provide large dynamic-deformation data on specimens having a relatively high strain-rate sensitivity, and to evaluate prediction methods which are designed to include this effect. Both simply supported and clamped beam tests have been carried out and compared with predictions; however, only midspan deflection time histories are available for comparing with theory.

##### 4.5.1 Predominant Bending Case: SS Beam

A typical experimental result is afforded by the SS-beam 129 midspan deflection history as shown in Fig. 4.25. To compare with the measured midspan deflection, three theoretical calculations were carried out:

- (a) EL-SH, bi-linear  $\sigma, \epsilon$  fit 7, with rolling support
- (b) EL-SH-SR with rolling support
- (c) EL-SH-SR with the beam permitted to slide freely over a fixed support.

In all cases, a model with 22.5 masses per semispan and a 6-flange thickness representation was used.

It is seen that the EL-SH response is much larger than either of the EL-SH-SR results, and all three predictions indicate peak deflections considerably greater than the observed value. As before, the influence of the sliding versus the rolling-support condition is to increase the peak deflection; the very early part of the response remains essentially unaffected by the type of simple support assumed. Observe that the smallest peak response predicted (EL-SH-SR, rolling) is 24 percent greater than the experimental value. Among the

reasons for this discrepancy, the following may be noted. The simple strain-rate approximation employed is not an accurate representation for steel. Also, the end fixture which served to keep the beam in contact with its simple support has a non-negligible mass moment of inertia about the "knife-edge" support upon which the beam rests, and undergoes angular acceleration when the slope of the beam at the support becomes large enough; the instant at which this occurs depends upon the clearance between the beam and the guide pins of the subject end fixture, and is difficult to establish reliably. However, the effect of this end fixture, which has not been accounted for in the predictions, would be to retard the response of the beam so as to lead to a smaller peak response than would occur in the absence of this effect. In view of these uncertainties, further discussion of the beam 129 results appears not to be worthwhile.

#### 4.5.2 Predominant Stretching Case: Clamped Beam

The support condition for the clamped 1010 steel beam experiments is well defined. Hence, this case should permit a clearer assessment of the accuracy and reliability of the prediction methods and the strain rate approximation employed for steel.

Figure 4.26 compares the measured midspan deflection time history with EL-SH and EL-SH-SR predictions using a 6-flange 30-mass model. These calculations show clearly that strain rate is very important for this material. Agreement between experiment and EL-SH-SR theory at and prior to the first peak is very good. There is a discrepancy between these two responses after the first peak has been reached; however, it is not a major one. This may be due in part to the presence of dynamic twisting but this can not presently be confirmed.

Observe also that the experimental and theoretical responses quickly subside after the first peak deflection has been reached, with somewhat greater residual oscillation present in the experiment. Clearly, very good permanent-deflection agreement between EL-SH-SR theory and experiment is achieved: EL-SH-SR theory gives .60 inch versus .55 inch to about an estimated .62 inch for the front and rear edges of beam 89, respectively.

It is interesting to compare the character of spanwise deflection profiles at various instants as predicted by EL-SH and EL-SH-SR theory. Such comparisons are shown in Fig. 4.27. Strain rate influence, as herein included, serves to "stiffen" the structure and reduces the curvature achieved by the specimen. The propagation of the bending wave is also evident. For this material, therefore, accurate spanwise deflection profile data would be a reasonably definitive means of assessing the importance of strain rate effects in structural response problems of this type. A more sensitive indicator, however, would be dynamic strain measurements. Unfortunately, neither of these two types of data is available for these 1010 steel beam experiments.

#### 4.6 Circular Rings

##### 4.6.1 Free Circular Rings

The results from two typical explosive-loading tests of 1/8-inch thick 6061-T6 circular rings are examined next; one case, specimen F4, involves moderate and the other specimen F15, a rather severe degree of response. Each specimen has been explosively loaded over a sector totaling 120 degrees.

Figure 4.28 compares the measured ring centerline mid-plane separation time-history with results predicted from EL-SH and EL-SH-SR calculations (see Table 4.5). During the period

for which measurements exist, there is excellent agreement between experiment and EL-SH-SR theory. As expected, a somewhat larger response is predicted by EL-SH theory.

Another interesting comparison is shown in Fig. 4.29, where the predicted\* midplane permanent deformation profiles are compared with a tracing of the inner and outer surfaces of the permanently-deformed ring. Both the EL-SH and the EL-SH-SR predictions are in reasonably good agreement with experiment, with the EL-SH-SR result being somewhat better.

A somewhat more sensitive comparison between experiment and theory is afforded by dynamic strain measurements made at 6 locations on the ring during the experiment; these results are shown in Fig. 4.30. In view of the earlier comparisons of strain histories among experiment, EL-SH theory, and EL-SH-SR theory, only the results from the latter calculation merit comparison here. Thus, these EL-SH-SR results are compared with experiment in Fig. 4.30. Strains were measured at positions 1, 2, 7, and 8 to check response symmetry, which is seen from Figs. 4.30 and 4.31 to be very good. An inspection of the results given on Fig. 4.30 shows that there is reasonably good agreement between theory and experiment during an initial period of about 700 microseconds. Beyond that time, there remains excellent phase agreement between experiment and theory even to seemingly anomalous details, but the predicted strain amplitudes are too large. This trend, of course, is consistent with the

- - - - -

\* These permanent deformation profiles are estimated by examining the ring centerline responses after the plastic energy absorption has ceased and by selecting as a "permanent-deformation profile" that which has an amplitude midway between the maximum and minimum responses in this residual elastic post-plastic response region.

deformation-response results of Fig. 4.29.

Since the mass-point locations in the theoretical model do not coincide with the strain-gage locations, this could be an added source of discrepancy; hence, plots of predicted strain on the outer and inner surfaces as a function of angular position are given in Fig. 4.31 for two instants: 1080 and 2580 microseconds. Plotted also are the measured strain at these instants. Note in Fig. 4.31 that for the portion beyond  $\theta$  greater than about 70 degrees, the ring is in a state of essentially pure bending; whereas, for  $-70^\circ \lesssim \theta \lesssim +70^\circ$ , the ring experiences both considerable compression and bending strain. Also a rapid strain reversal, as expected, occurs near  $\theta = 60^\circ$  where the edge of the HE layer was located.

The F-15 ring results, involving more severe response, are given in Figs. 4.32-4.35. Figure 4.32 compares the measured ring centerline midplane separation time-history with results predicted from EL-SH and EL-SH-SR calculations (see Table 4.5). In this more severe response case where one expects strain-rate effects to become more important, it is seen that the EL-SH response is much greater than the EL-SH-SR response, with the EL-SH-SR response peak being about 10 percent larger than experiment. Also, the overall EL-SH-SR response history is in good agreement with experiment.

It is also interesting to compare measured and predicted deflection profiles at a sequence of times to assess the faithfulness of the theory in predicting the response details throughout the ring. This is done in Fig. 4.33 at  $t = 510, 1160, 1976$ , and 2584 microseconds and for the permanent deflection condition. The EL-SH and the EL-SH-SR results shown are those for the closest printout time in the calculations. Note that the

experimental deformation profiles are almost but not quite symmetrical, whereas the computer deformation was treated (by choice, not by necessity) as being symmetrical.

At 510 microseconds, there is already a very considerable difference between the measured profile and that given by EL-SH theory, although the difference at the centerline is not very great. On the other hand, the EL-SH-SR deformation profile is still in good overall agreement with experiment. This same trend is seen at 1160, 1976, and 2584 microseconds and at the permanent-deformation condition, where the EL-SH result is consistently poor and the EL-SH-SR result falls reasonably close to experiment. Also note that the experimental deformed profile appears to exhibit some waviness\* but this is not clear enough for more explicit identification. However, note that this waviness is not apparent in the final deformed specimen.

Figure 4.34 compares measured strain histories with those predicted by EL-SH-SR theory. Good amplitude and phase agreement is observed for about the first 600 microseconds. After this time, excellent phase agreement remains but the predicted amplitudes are too large (peaks being about 30 percent too high). This also is consistent with Fig. 4.32 and 4.33 results. Note that peak measured strains ranging from about 2.5 to 4.5 percent occur. Also, if the experimental results at positions 1 and 3 were interchanged, they would be consistent with predictions.

- - - - -  
\* This effect suggests some similarity to waviness observed in similar experiments reported in references 21 and 22.

Strain profiles predicted by EL-SH-SR theory have been plotted in Fig. 4.35 at  $t = 1380$  and  $3000$  microseconds and are compared with measurements at these instants. At  $t = 1380$ , fairly good agreement between theory and experiment is noted; at  $t = 3000$ , the measured and predicted trends are consistent but the strains are overestimated. Again, note that the ring undergoes essentially pure bending beyond  $\theta = 70^\circ$ ; whereas, for  $-70^\circ \lesssim \theta \lesssim 70^\circ$ , the ring experiences both considerable compressive strain and bending behavior. Rapid strain reversal again occurs at about  $60$  degrees.

#### 4.6.2 Clamped Ring

Figures 4.36-4.39 show the deformation and strain response histories for a typical explosively-loaded clamped circular ring of 6061-T6 material (see Tables 4.4 and 4.5). Because the clamped-ring tests could be carried out with less measurement difficulty than the free-ring tests and were thus expected to yield higher quality data, clamped-ring tests were conducted. Also, these tests provide data to test the adequacy of the analysis to treat a structure which has fully clamped ends but does not undergo dominant stretching (membrane) behavior as in the case of the clamped beams.

Figure 4.36 compares the time history of the measured central deflection of the ring (C4) with EL-SH and EL-SH-SR predictions. The latter prediction is seen to be in good agreement with experiment both in amplitude and in phase; whereas the EL-SH prediction vastly overestimates the response.

To assess the accuracy of the deformation predictions throughout the ring, experimental and predicted (EL-SH and EL-SH-SR) deformation profiles are compared in Fig. 4.37 at  $785$ ,  $2854$ ,

and 5495 microseconds after HE detonation and at the permanent-deformation condition. At 785 microseconds, the ring is observed to be deforming in an almost but not exactly symmetrical fashion; at this time, both predictions are in reasonably close agreement with experiment, with the EL-SH-SR being the better. At 2854 microseconds, EL-SH-SR theory still is in reasonable agreement with experiment but the EL-SH result vastly overestimates the deformation; now, however, the actual deformation is exhibiting a definite asymmetry. Near maximum springback, 5495 microseconds, a similar comparison is observed between theory and experiment; some degree of deformation asymmetry exists. Also, there appears to be a certain degree of waviness of the observed shape. However, with the present mass spacing, the possible presence of waviness in the predicted profiles is not observable. Finally, note that the measured permanent-deformation profile continues to exhibit some asymmetry and that the EL-SH-SR prediction remains in reasonably good agreement with experiment while the EL-SH calculation vastly overestimates the deformation.

A more sensitive comparison between theory and experiment is afforded by measurements of strain versus time at several positions on the inner and outer surfaces of the ring. It is already clear that the EL-SH prediction greatly overestimates the deformation and thus the strain as well. Hence, Fig. 4.38 compares measured histories with those of EL-SH-SR theory. Consistent with the deformation results seen earlier, after an early period of close agreement with experiment, the strain histories predicted with the EL-SH-SR calculation exceed those of experiment; however, excellent phase agreement of theory with experiment remains.

Some of the discrepancy between EL-SH-SR theory and experiment may arise from the fact that the peripheral locations of the strain gages do not coincide with the mass-point locations of the theoretical model. Thus, computed strain distributions around the periphery of the ring are shown in Fig. 4.39 at three instants: 780, 1980, and 2880 microseconds; the measured strains at these instants are also plotted. It is observed that the predicted and measured distributions and amplitudes of strain are in good agreement. Again, abrupt reversal of strain occurs at  $\theta = 60$  degrees which was the location of the edge of the HE layer. As in the case of the free rings, nearly pure bending strain is observed for  $\theta$  greater than about 70 degrees for the clamped ring; considerable compression strain plus bending strain is seen to exist for smaller  $\theta$  angles.

#### 4.7 Comparisons with Rigid Plastic Theory

It has been pointed out earlier that the clamped beams have been chosen as producing predominant stretching behavior, and the simply-supported beams as producing predominant bending behavior. Permanent deformations for these cases can be estimated with a simple approximate energy method in which the material is treated as rigid, perfectly-plastic. It is assumed that in the case of a clamped beam, the entire beam deforms by stretching at the constant axial yield force throughout the response or, in the case of the simply-supported beam, deformation occurs entirely by bending at the constant bending yield moment. By taking a plausible deflection mode, the energy absorbed during plastic flow is obtained as a function of the midspan deflection by a simple spanwise integration. The fact that the total plastic work done along the entire response is

assumed to be equal to the initially imparted kinetic energy permits the calculation of the permanent midspan deflection.

Predicted permanent midspan deflections of the simply-supported and clamped beams (listed in Table 4.4) are now compared in Table 4.6 with the corresponding experimental deflections. The pertinent dimension and loading data can also be found in Table 4.4. The following average "perfectly plastic" yield limits have been chosen:

6061-T6:	42,000; 43,500; 45,000 psi (compare Fig. 4.1)
2024-0:	18,000 psi (compare Fig. 4.2)
1010 steel:	16,000 psi (compare Fig. 4.4)

Note that the values pertaining to the considerably strain-hardening materials, 2024-0 and 1010 steel, must be considered as rough estimates. For these calculations, the assumed deformation shapes chosen\* were:

$$w = \delta \sin(\pi x / l)$$

for the simply-supported beam and

$$w = 4\delta \left( \frac{x}{l} - \frac{x^2}{l^2} \right)$$

for the clamped beam, where the midspan deflection  $\delta$  is determined from the assumption that the entire initially imparted kinetic energy is absorbed by plastic work.

- - - - -  
\* The effects of various assumed deformation shapes are shown in Reference 23.

Compared with the simply-supported beams, the clamped beams exhibit a reasonable degree of agreement between theory and experiment. The rigid-plastic approximation which allows no elastic deformation is obviously more appropriate for clamped beams with axial constraints where the variations in deflection remain small once the first peak has been attained (see for example, Fig. 4.17); in this case essentially all of the input energy is absorbed by plastic work, whereas a much smaller fraction of the input energy is absorbed by direct plastic work for these simply-supported beam cases.

For a given beam, the permanent deflection obtained by the above energy method is solely dependent upon the assumed deformation shape and the initially imparted kinetic energy, but does not depend upon the details of the initial velocity distribution; also, this method does not provide the transient response. Although the exact rigid-plastic transient-response theory does not have these deficiencies, it is nevertheless inadequate if the transient response becomes important as in the case of simply-supported beams. This is demonstrated in Fig. 4.40 where the present elastic-plastic theory and rigid-plastic theory are compared with experiment.

#### 4.8 Summary Comments on the Present Comparisons

It is useful at this point to restate concisely the primary factors and features which the present experiments and correlation studies were designed to scrutinize and evaluate. This is done in the following tabular summary.

Type of Specimen	Geometric-Induced Behavior Being Examined	Emphasized Type of Material Behavior Intended			Comparisons Available				
		6061-T6	2024-0	1010	Deflections	Defl. Profiles	Strain Histories	Strain Distributions	
SS Beams	Dominant Bending	EL-PP	EL-SR	EL-SH-SR	x	x	-	-	
Clamped Beams	Dominant Extensional	EL-PP	EL-SH	EL-SH-SR	x	x	x	x	
Free Rings	Dominant Bending plus Significant Extensional	EL-PP	--	--	x	x	x	x	
Clamped Rings	Dominant Bending plus Significant Extensional plus Clamped Boundary	EL-PP	--	--	x	x	x	x	

Here are cited the types of models employed, the primary behavior for which model geometry is responsible, the intended primary behavior due to different mechanical properties of the material, and the types of data available for comparing with predictions.

It has been shown that, for all of the above cases, the present elastic-plastic prediction method for two-dimensional structural response permits predictions which are in excellent qualitative agreement and generally good quantitative agreement with experiment. Clear evidence of the listed types of behavior arising from specimen geometry as listed in the first column was seen both in the experimental and in the theoretical results; the only geometric factor not precisely definable in these experiments as conducted concerned the "restraint of the end fixture" for the simply-supported beams. The histories and instantaneous profiles of strain and deflection permitted making a reasonably thorough appraisal of the adequacy and accuracy of the present prediction method, despite the presence of some uncertainties.

Among the uncertainties present are the following:

- (a) The Impulsive Input. Although considerable effort was devoted to impulse calibration, the impulsive inputs to the dynamic-response models remains somewhat uncertain, as explained in Section V.
- (b) Dynamic Twisting. This arose since the HE detonation front traveled across the width direction of each specimen. The present predictions, however, apply strictly to two-dimensional structural response.

- (c) Static Stress-Strain Properties. Tensile tests on representative samples from each material lot were made, and exhibited some scatter due probably to both experimental measurement uncertainty and to material variations. Also, compressive stress-strain measurements should be made since many materials exhibit distinct differences in tensile and compressive behaviors.
- (d) Dynamic Stress-Strain Properties. Tensile tests of this type were conducted on the materials employed. However, the strain rate range covered was very restricted (less than 15 in/in/sec) and the experimental measurement and interpretation uncertainties were larger than desired, whereas, strain rates ranging up to about 3000 in/in/sec occurred in the dynamic response cases studied. Further work on this aspect of the problem is clearly required, including compressive tests.

The present method can accommodate different stress-strain behavior in tension and compression.

Despite these uncertainties, the present correlation studies of experimental strain and deflection histories and profiles compared with predictions permit one to conclude that the present elastic-plastic prediction method for two-dimensional large dynamic deformations is reliable. The inclusion of an approximate accounting for strain-rate behavior of the material is shown to have a significant effect on the maximum elastic-plastic response, the response phasing, and the (estimated) permanent deformation. Further improvement in experimental-theoretical agreement for cases such as the rings and clamped beams is believed to depend upon (1) the measurement and use of more accurate mechanical property data for the material, especially strain-rate data over a wider strain-rate range, (2) the extension of the method to three-

dimensional deformations in order to account for dynamic twisting, and (3) more refined impulsive-input and initial-model-geometry data. The latter should permit predicting the asymmetrical response noted in certain ring experiments.

Dynamic deformation histories can be computed for certain simple structures from rigid-plastic theory, but are laborious and provide results which are significantly different from both experiment and elastic-plastic theory, giving too small a peak response. Also, permanent deformations for simply-supported beams computed from rigid-plastic transient response theory and from a simple approximate energy method applicable to rigid-plastic materials are found to be in rather poor agreement with experimental results from the present beam experiments. However, for the clamped-beam cases studied, the permanent deformations predicted by the approximate energy method which ignores strain hardening and strain-rate effects are overestimated by only about 25 per cent on the average, except for the 1010 steel-beam example. Since these simplified methods employ the assumption that all of the input energy is absorbed plastically, reasonable predictions cannot be expected in cases for which a substantial fraction of energy input "remains" in elastic and kinetic forms.

## SECTION V

### SUMMARY AND CONCLUSIONS

#### 5.1 Theory and Correlation

The matter of principal interest in the present study is the prediction of large dynamic elastic and post-elastic responses and permanent deformations of simple structures. The present formulation is restricted to two-dimensional and/or axisymmetric responses, neglecting the effects of shear deformation and rotary inertia, and employing the Kirchhoff assumption; thus, within this framework, the present analysis applies to multi-layer hard-bonded structures of various similar or dissimilar materials. Approximate representations: EL-PP, EL-SH, and EL-SH-SR, of the stress-strain properties of the material lead to reasonable theoretical-experimental agreement with peak deflection response and permanent deformation, with the EL-SH-SR results being consistently the better. Strain history comparisons served to emphasize the importance of accounting for strain-rate effects even for the relatively strain-rate-insensitive materials such as aluminum alloy. Improvements in predictions are expected to be realized mainly from the use of more accurate material property or constitutive data and more complete and faithful representations of these properties in the analysis.

Several sources of remaining discrepancy between the present theory and experiment may be cited in addition to the constitutive-relation question. The applied loading was such that a certain (but undefined) amount of dynamic twisting was induced in the specimens whereas the theory presently pertains strictly to two-dimensional response. Despite the fact that the impulse input in the present ex-

periments has been defined at least as and perhaps more accurately than in any other transient loading cases reported in the literature, some distinct uncertainties in these inputs remain, particularly with respect to 2024-0 beam results where apparent impulse-response discrepancies ranging up to about 25 per cent are implied; for the remaining cases, the impulse uncertainty appears to be considerably less. Although the boundary conditions for the free rings, clamped rings, and clamped beams are well defined, the support restraint for the "simply-supported" beams remains somewhat uncertain, particularly the dynamic interaction between the beam and the (rotatable) end fitting which depends critically upon the clearance between beam and support and the moment of inertia of the subject end fixture; this end-fixture effect has not been well defined or treated in the analysis.

The method of analysis employed is simple and straightforward principally because the displacements and strains are extrapolated ahead so that one solves in sequence the displacement-strain, the strain-stress, and the equilibrium equations using a very short time interval. Because of this process it is very easy to incorporate suitable constitutive relations since the strains, strain increments, and strain rates are known at each step of the computation.

The present two-dimensional axisymmetric formulation requires the use of a small space mesh to permit reliable predictions of details of large dynamic response and permanent deformation, with the required space-mesh size depending upon the intensity, distribution, and time history of the forcing function. The resulting number of mass points and the calculation time interval require considerable computing time even on an IBM 7094 computer; for many of the cases calculated and discussed in Section IV, from about 3 to 7

minutes of IBM 7094 time were required for the response durations shown. In view of this and the fact that the present analysis enables one to follow in detail the transient strains and deflections and their distributions as well as the partitioning of the energy of the system among kinetic, elastic, and plastic forms,\* it is desirable to use the present formulation as a learning tool for studying large dynamic elastic-plastic response in order to obtain guidance for the formulation of simpler, less time-consuming predictions and to define realistically the conditions under which these (or other) simpler methods yield reliable predictions.

The thickness idealization employed in the present calculation model has been found to be particularly convenient for studying the influence of various constitutive relation approximations. Also, the use of more than four idealized-thickness flanges alters the resulting dynamic response for a given problem very little compared with the use of additional idealized-thickness flanges; the least number of flanges that can be employed meaningfully in this analysis is two, but at least four and preferably six are recommended. The use of more than six idealized-thickness flanges does not sensibly change the predicted response, and requires an unnecessary expenditure of computer time.

Through the use of a simple mechanical sub-flange model [13], it has been found feasible to account for strain hardening behavior very faithfully. In certain cases involving materials which exhibit considerable strain hardening such as 1100-0 aluminum alloy, a bi-linear stress-strain fit is inadequate and a careful accounting for strain hardening is essential [17].

---

\* Note that damping other than plastic work is not provided for in the present analysis; thus, the computed response exhibits undiminished oscillations indefinitely after plastic work has ceased.

For some beam cases studied in the present program, the use of a simple energy method together with rigid-plastic material behavior enables one to make fairly good estimates of beam permanent midspan deflection, but no transient information is obtained; with this method, no reliable rules for accounting reasonably for strain rate effects are available. A rigid-plastic dynamic response analysis can be carried out for simple cases, but the transient response differs significantly from the experimental and the elastic-plastic responses. However, an approximate accounting for strain rate and large deflections in rigid-plastic calculations [12,14] have lead to significantly improved permanent-deformation agreement with experiment, but there are still significant differences in dynamic response details.

Finally, there are several obvious desirable extensions of the present formulation which can be cited and which currently are being carried out. One of the most important is the lifting of the two-dimensional and axisymmetric response restrictions; a more realistic theoretical-experimental comparison for the several types of experiments discussed herein can then be made. This step should be of particular importance in improving predictions of permanent deformations of projectile-impacted hemispherical shells and the incipient-buckling threshold for blast-loaded spherical shells [24]. Another interesting extension pertains to treating several geometric configurations of multi-layer shells of similar or dissimilar material which are soft bonded or unbonded between layers. Further extensions to include ring-, frame-, and longeron-stiffened single- and multi-layer shells of various geometries would be useful; a rather straightforward extension can be made, but the number of mass points involved and the computer time required to carry out a given response calculation would be formidable. Simplified, less time-

consuming methods retaining the essential features of the problem should be sought; these will likely differ, for a given structure, depending upon the distribution, intensity, and time history of the forcing function.

## 5.2 Experiment

The experimental techniques employed for measuring transient strains and deflections in the present beam and ring experiments afford high accuracy and excellent time resolution.

In view of the fact that in the correlation studies where the model has been represented by an adequate number of masses and a six-flange thickness idealization has been used together with a consistent usage of the EL-SH-SR data presently available, the following trend concerning impulse input level is implied;

- (a) impulse consistently low for all beam specimens of 6061-T6 and 2024-0 material by from about 10 to 25 per cent,
- (b) impulse too high for the simply-supported 1010 steel beams and essentially "correct" for the clamped 1010 steel beams, and
- (c) impulse only slightly high for the 6061-T6 rings.

It appears that further work to reduce the input uncertainty is warranted. Particularly valuable would be the use of a technique to determine the impulsive input in each dynamic response test, rather than relying upon separate calibration tests upon which to estimate the subject input. While other factors may be mainly responsible for the above "discrepancies," the suggested procedure should serve to minimize the input uncertainty.

Among the other factors which may be responsible for the aforementioned discrepancies are the static and dynamic stress-strain properties of the material and the approximations involved in the analytical fits used to represent these properties. It appears that the present knowledge of the rate-dependent material properties constitutes the source of greatest uncertainty in the present work. In particular, the need for precise measurements of stress-strain properties: first under uniaxial stress conditions covering a strain rate range up to at least 3000 in/in/sec is needed to cover the conditions of interest for the present experiments; then secondly, similar determinations are needed under biaxial stress states. Subsequently, material behavior should be determined under more general conditions. With respect to analytical fits used to approximate the stress-strain properties, these can be made to represent the material properties essentially as accurate as one's knowledge of those properties warrants; hence, the importance of this factor is presently (and for future cases can be made) negligible.

## REFERENCES

1. Pian, T. H. H. "A Note on Large Plastic Deformations of Beams under Transverse Impact." Massachusetts Institute of Technology, ASRL TR 25-11, May 1952.
2. Symonds, P. S. "Large Plastic Deformations of Beams under Blast Type Loadings." Proc. 2nd U.S. National Congress of Applied Mechanics, 505-515, 1954.
3. Leech, J. W., Pian, T. H. H., Witmer, E. A., and Herrmann, W. "Dynamic Response of Shells to Externally-Applied Dynamic Loads." Massachusetts Institute of Technology, ASD-TDR-62-610, November 1962.
4. Witmer, E. A., Balmer, H. A., Leech, J. W., and Pian, T. H. H. "Large Dynamic Deformations of Beams, Rings, Plates, and Shells." AIAA Journal, Vol. 1, No. 8, pp 1848-1857, August 1963.
5. Clark, E. N., Schmitt, F. H., and Ellington, D. G. "Explosive Impulse on Structures." Picatinny Arsenal, MIPR(33-616) 61-31-No. 6, September 30, 1962.
6. Clark, E. N., Schmitt, F. H., Ellington, D. G., Engle, R., and Nicolaides, S. "Plastic Deformation of Structures." Volume I-Study of the Plastic Deformation of Beams, Volume II-The Plastic Deformation of Rings." Picatinny Arsenal, FDL-TDR 64-64 (to be published).
7. Clark, E. N., Schmitt, F. H., and Ellington, D. G. "Explosive Impulse on Structures." Picatinny Arsenal, MIPR(33-616) 61-31-No. 5, June 30, 1962.
8. Roach, T. M. Jr. "High Loading Rate Testing Machine, Development and Typical Materials Testing Applications." pp. 341-358, Proceedings of the Army Conference on Dynamic Behavior of Materials and Structures, September 1962.

9. Owen, R. H. and Symonds, P. S. "Plastic Deformations of a Free Ring under Concentrated Dynamic Loading." J. Appl. Mech., 22, 523-529, 1959.
10. Chen, M. M., Hsu, P. T., and Pian, T. H. H. "Impulsive Loading of Rigid-Plastic Curved Beams." AFOSR TR 316, also Proc. 4th Nat'l. Congr. Appl. Mech., 1, 1039-1045, 1962.
11. Wang, A. J. "Permanent Deflection of a Plastic Plate under Blast Loading." J. Appl. Mech., 22, 375-376, 1955.
12. Bodner, S. and Symonds, P. S. "Experimental and Theoretical Investigation of the Plastic Deformations of Cantilever Beams Subjected to Impulsive Loading." J. Appl. Mech. 29, 719-728, 1962.
13. Prager, W. and Hodge, P. G. "Theory of Perfectly Plastic Solids." John Wiley and Sons, Inc., New York 1951.
14. Ting, T. C. T. "The Plastic Deformation of a Cantilever Beam with Strain Rate Sensitivity under Impulsive Loading." Brown University TR 70, Contract Nonr-562(10), July 1961.
15. White, G. N., Jr. "Application of the Theory of Perfectly Plastic Solids to Stress Analysis of Strain Hardening Solids." Grad. Div. Appl. Math., Brown University, TR No. 51, August 1950.
16. Crandall, S. H. "Engineering Analysis." McGraw-Hill Book Co., Inc., New York 1956.
17. Balmer, H. A. and Witmer, E. A. "Examination of Data on Impulsively-Loaded Circular Flat Plates with Clamped Boundaries." Massachusetts Institute of Technology, ASRL Report on DSR Project 9906, September 1963.

18. Hauser, F. E., Simmons, J. A., and Dorn, J. E. "Strain Rate Effects in Plastic Wave Propagation." pp. 93-114, Response of Metals to High Velocity Deformation, Interscience Publishers, New York 1961.
19. Bell, J. F. "Propagation of Large Amplitude Waves in Annealed Aluminum." J. Appl. Phys., Vol. 31, pp. 277-282, 1960.
20. Fowles, G. R. "Shock Wave Compression of Hardened and Annealed 2024 Aluminum." Stanford Research Institute, Poulter Laboratories, TR 011-60, October 25, 1960.
21. Abrahamson, G. R. and Goodier, J. N. "Dynamic Plastic Flow Buckling of a Cylindrical Shell from Uniform Radial Impulse." Fourth U. S. Nat'l. Congr. Appl. Mech., June 18, 1962.
22. Lindberg, H. E. "Buckling of a Very Thin Cylindrical Shell due to an Impulsive Pressure." ASME Applied Mechanics Division, Paper No. 63-APMW-7, March 15, 1963.
23. Witmer, E. A., Herrmann, W., Leech, J. W., and Pian, T. H. H. "Responses of Plates and Shells to Intense External Loads of Short Duration." Massachusetts Institute of Technology, WADD TR 60-433, April 1960.
24. Witmer, E. A., Pian, T. H. H., and Balmer, H. A. "Dynamic Deformation and Buckling of Spherical Shells under Blast and Impact Loading." pp. 607-622, Collected Papers on Instability of Shell Structures, NASA TN D-1510, November 1962.

<p align="center">TABLE 4.1</p> <p align="center">Identification of Static and Dynamic Stress-Strain Specimens from Material Lots Associated with Impulsively-Loaded Beams and Rings</p>						
Material Lot Identification Number (1)	Material and Type	Stress-Strain Test Specimen Designation (2)		Dynamic Test Specimens		
		Static	Dynamic	Type (3)	PA Run Ident. Number (4)	Dimensions (5) (t,w,L(in))
I	Aluminum 6061-T6	1A,6A	--	SS Beam	B-20-25-121	.25x1.2x10.07
II	Aluminum 6061-T6	A,B	G,J	C Beam SS Beam C Beam C Beam	P-15-125-95 B-15-125-131 P-30-125-2 P-15-125-3	.125x1.2x10.01 .125x1.2x10.07 .123x1.2x10.01 .125x1.2x10.01
III	Aluminum 6061-T6	19,20	--	C Beam C Beam	P-25-25-111 P-25-25-112	.25x1.2x10.01 .25x1.2x10.01
IV	Aluminum 2024-0	1B,2B	3B,5B	C Beam SS Beam	P-15-125-100 P-15-125-134	.125x1.2x10.01 .125x1.2x10.07
V	Aluminum 2024-0	21,22,23	--	C Beam SS Beam	P-20-25-88 B-15-25-119	.25x1.2x10.01 .25x1.2x10.07
VI	Steel 1010	1,2	6,7,10	C Beam SS Beam	P-20-125-89 B-15-125-129	.125x1.2x10.01 .125x1.2x10.07
VII	Aluminum 6061-T6	C1,C2 (cylinders) A,D,E (axial coupons) K,L,M (hoop coupons)	-- -- --	F Ring F Ring C Ring	F4 F15 C4	.125x1.2x6" O.D. .125x1.2x6" O.D. .125x1.2x6" O.D.

- (1) These Roman numerals are employed for convenience to identify particular lots of material in this report.
- (2) These designations are those supplied by Picatinny Arsenal personnel who conducted the experiments.
- (3) Prefix meanings: SS- simply supported, C-clamped, F-free.
- (4) These are Picatinny Arsenal identification numbers (Ref. 5).
- (5) Dimensions listed here are nominal values; for SS-Beams, the distance between supports is 10.07 in. (overall beam lengths were 12.00 in.) and is 10.01 in. for the clamped (C) beams.

TABLE 4.2						
Summary of Bi-Linear Approximations to Static Stress-Strain Properties of Beam and Ring Materials						
Material	Lot	Fit No.	E(psi)	$\sigma_o$ (psi)	$\epsilon_o$ (in/in)	$E_p$ (psi)
6061-T6	I	1	$10.6 \times 10^6$	43,800	$4.13 \times 10^{-3}$	88,900
6061-T6	II	2	$10.8 \times 10^6$	41,600	$3.85 \times 10^{-3}$	161,000
6061-T6	III	3	$10.7 \times 10^6$	41,200	$3.85 \times 10^{-3}$	61,200
2024-0	IV, V	4	$10.9 \times 10^6$	13,500	$1.24 \times 10^{-3}$	605,000
2024-0	IV, V	5	$10.9 \times 10^6$	11,600	$1.064 \times 10^{-3}$	1,024,000
2024-0	IV, V	6	$10.9 \times 10^6$	21,000	$1.927 \times 10^{-3}$	0
1010	VI	7	$29.2 \times 10^6$	11,600	$0.397 \times 10^{-3}$	385,000
6061-T6	VII	8	$10.50 \times 10^6$	42,800	$4.08 \times 10^{-3}$	78,700

TABLE 4.3				
Five-Segment Fit of 2024-0, Lot V (Termed Fit No.9)				
Segment	E(psi)	$\sigma_f$ (psi)	$\epsilon_f$ (in/in)	$E_p$ (psi)
1	$10.9 \times 10^6$	11,200	.00103	--
2	--	17,300	.0066	$1.095 \times 10^6$
3	--	24,000	.0170	0.644
4	--	30,000	.0380	0.286
5	--	--	--	0

Type of Test	Specimen	Material	SPECIMEN DATA					HE LOADING DATA				Permanent Midspan Deflection (in)
			t(in)	w(in)	l(in)	weight (gms)	t*(in)	l(in)	HE weight (gms)	Impulse x 10 <sup>-4</sup> dyne-sec	Front Edge	
SS Beam	B-20-25-121	6061-T6	.253	1.187	12.002	158.10	.020	1.988	1.160	21.58	.781	--
SS Beam	B-20-25-123	6061-T6	.251	1.189	12.006	158.45	.020	1.988	1.082	20.12	.553	--
C Beam	P-15-125-95	6061-T6	.124	1.195	21.868	143.62	.015	1.932	0.870	16.18	.581	.700
SS Beam	B-15-125-131	6061-T6	.131	1.197	12.018	82.66	.015	0.997	0.403	7.50	.995	--
C Beam	P-30-125-2	6061-T6	.124	1.199	21.865	143.15	.030	1.739	1.513	28.15	.961	1.021
C Beam	P-15-125-3	6061-T6	.124	1.195	21.867	142.78	.015	1.741	0.730	13.60	.456	.470
C Beam	P-25-25-111	6061-T6	.242	1.195	21.979	280.32	.025	1.988	1.548	28.79	.494	.522
C Beam	P-25-25-112	6061-T6	.241	1.196	21.980	280.19	.025	1.988	1.552	28.86	.550	.564
C Beam	P-15-125-100	2024-0	.124	1.192	22.012	147.56	.015	1.731	0.837	15.57	.921	.945
SS Beam	B-15-125-134	2024-0	.125	1.205	12.012	82.34	.015	0.795	0.361	6.71	1.93	1.80
C Beam	P-20-25-88	2024-0	.249	1.193	22.008	297.60	.020	1.988	1.059	19.69	.572	--
SS Beam	B-15-25-119	2024-0	.252	1.202	12.017	165.55	.015	1.988	0.832	15.47	1.06	--
C Beam	P-20-125-89	1010	.124	1.202	22.005	421.61	.020	1.932	1.043	19.40	.549	--
SS Beam	B-15-125-129	1010	.124	1.203	12.003	230.14	.015	1.731	0.793	14.74	1.84	--
F Ring	F4	6061-T6	.124	1.201	6.01 O.D.	121.46	.015	6.28	2.387	44.40**	--	--
F Ring	F15	6061-T6	.124	1.195	6.00 O.D.	120.62	.020	6.27	3.757	69.87**	--	--
C Ring	C4	6061-T6	.123	1.197	5.99 O.D.	118.30	.0147	6.32	2.639	49.08**	--	--

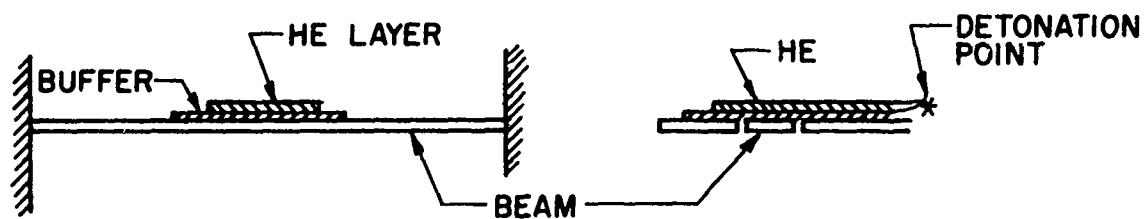
\* Nominal thickness

\*\* Radial impulse

TABLE 4.5											
Summary of Theoretical-Prediction Features and Parameters used to Compare with Experimental Responses of Explosively-Loaded Beams and Rings											
TEST SPECIMEN			DYNAMIC MODEL FEATURES								
Type	Material	No.	No. of Masses per Semispan (d)	No. of Flanges	Type of Support	Material Representations			Results on Figures (No.)		
						EL-PP	EL-SH	EL-SH-SR			
SS Beam	6061-T6	121	22.5 " " " "	6 6 6 6 2	SS-Rolling SS-Rolling SS-Rolling SS-Sliding SS-Rolling	x	x(fit 1)	x(a) x(b) x(a)	4.12, 4.13, 4.40 4.12, 4.13 4.12 4.12 4.12		
SS Beam	6061-T6	131	" " 22.5	6 6 6	SS-Rolling SS-Rolling SS-Sliding		x(fit 2)	x(a) x(b)	4.14 4.14 4.14		
C Beam	6061-T6	111	30 30 30	6 6 6	Clamped Clamped Clamped		x(fit 3)	x(a) x(b)	4.15 4.15 4.15		
C Beam	6061-T6	112	30	6	Clamped			x(a)	4.16		
C Beam	6061-T6	95	30 30	6 6	Clamped Clamped		x(fit 2)	x(a)	4.17 4.17		
C Beam	6061-T6	3	30 30	6 6	Clamped Clamped		x(fit 2)	x(a)	4.18 4.18		
C Beam	6061-T6	2	30 30	6 6	Clamped Clamped		x(fit 2)	x(a)	4.19 4.19		
SS Beam	2024-0	119	22.5 22.5	6 6	SS-Rolling SS-Rolling		x(fit 4)	x(a)	4.20 4.20		
SS Beam	2024-0	134	22.5 22.5 22.5	6 6 6	SS-Rolling SS-Rolling SS-Sliding		x(fit 4)	x(a) x(a) x(a)	4.21 4.21 4.21		
C Beam	2024-0	88	30 30 30 30	6 6 6 6	Clamped Clamped Clamped Clamped		x(fit 4) x(fit 9)	x(a) x(b)	4.22, 4.23 4.22, 4.23 4.22 4.22		
C Beam	2024-0	100	30 30	6 6	Clamped Clamped		x(fit 4)	x(a)	4.24 4.24		
SS Beam	1010	129	22.5 22.5 22.5	6 6 6	SS-Rolling SS-Rolling SS-Sliding		x(fit 7)	x(c) x(c)	4.25 4.25 4.25		
C Beam	1010	89	30 30	6 6	Clamped Clamped		x(fit 7)	x(c)	4.26, 4.27 4.26, 4.27		

TABLE 4.5 (Concluded)									
TEST SPECIMEN			DYNAMIC MODEL FEATURES						Results on Figures (No.)
Type	Material	No.	No. of Masses per Semi-span (d)	No. of Flanges	Type of Support	Material Representations			
						EL-PP	EL-SH	EL-SH-SR	
Free Ring	6061-T6	F4	31 31	6 6	None None		x(fit 8)	x(a)	4.28, 4.29 4.28, 4.29, 4.30, 4.31
Free Ring	6061-T6	F15	30 30	6 6	None None		x(fit 8)	x(a)	4.32, 4.33 4.32, 4.33, 4.34, 4.35
C Ring	6061-T6	C4	31 31	6 6	Clamped Clamped		x(fit 8)	x(a)	4.36, 4.37 4.36, 4.37, 4.38, 4.39
(a) Used rate constants $D = 6500 \text{ sec}^{-1}$ , $p = 4$ from reference 14									
(b) Used rate constants $D = 7000 \text{ sec}^{-1}$ , $p = 2.13$ from present tests									
(c) Used rate constants $D = 40.4 \text{ sec}^{-1}$ , $p = 5$ from reference 14									
(d) This number represents the number of masses from the centerline of the beam to its support									

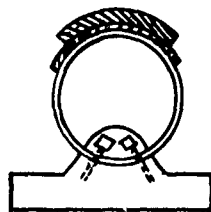
<p align="center"><b>TABLE 4.6</b>  <b>Comparison Between Experimental and Predicted Permanent</b>  <b>Midspan Beam Deflections Obtained by an Approximate</b>  <b>Energy Method</b></p>				
TEST SPECIMEN	MATERIAL	PERMANENT MIDSPAN DEFLECTION		
		$\delta_{\text{theor}}$ (in)	$\delta_{\text{expt}}$ (in)	$\delta_{\text{theor}}/\delta_{\text{expt}}$
<u>Simply-Supported Beams</u>				
B-20-25-121	6061-T6	1.48	0.78	1.90
B-20-25-123	6061-T6	1.29	0.55	2.35
B-15-125-131	6061-T6	2.62	1.00	2.62
B-15-125-134	2024-0	6.89	1.87	3.68
B-15-25-119	2024-0	1.81	1.06	1.71
B-15-125-129	1010 Steel	6.25	1.84	3.40
<u>Clamped Beams</u>				
P-15-125-95	6061-T6	0.73	0.64	1.14
P-30-125-2	6061-T6	1.34	0.99	1.35
P-15-125-3	6061-T6	0.65	0.46	1.41
P-25-25-111	6061-T6	0.67	0.51	1.31
P-25-25-112	6061-T6	0.67	0.56	1.20
P-15-125-100	2024-0	1.14	0.93	1.23
P-20-25-88	2024-0	0.67	0.57	1.18
P-20-125-89	1010 Steel	0.84	0.55	1.53
<p>* Simply-supported beam: <math>\delta_{\text{theor}} = 0.159(T_0 \ell / M_0)</math>  Clamped beam: <math>\delta_{\text{theor}} = 0.612 \sqrt{T_0 \ell / N_0}</math>  where <math>\ell</math> = length between supports  <math>N_0</math> = axial yield force  <math>M_0</math> = yield moment  <math>T_0</math> = initially imparted kinetic energy</p>				



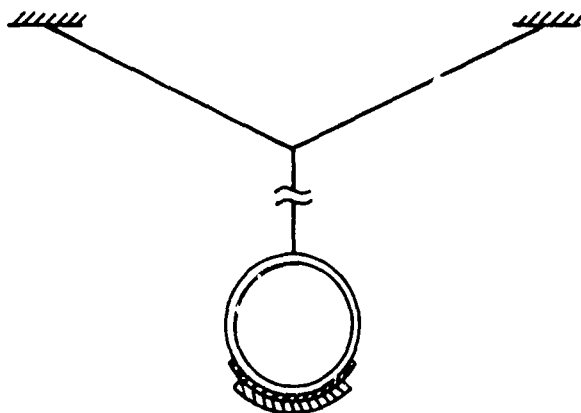
(a) CLAMPED BEAM



(b) SIMPLY SUPPORTED BEAM



(c) CLAMPED SINGLE-LAYER RING



(d) FREELY-SUSPENDED SINGLE-LAYER RING

FIG. 2.1. SCHEMATICS OF EXPLOSIVELY-LOADED SIMPLE STRUCTURES

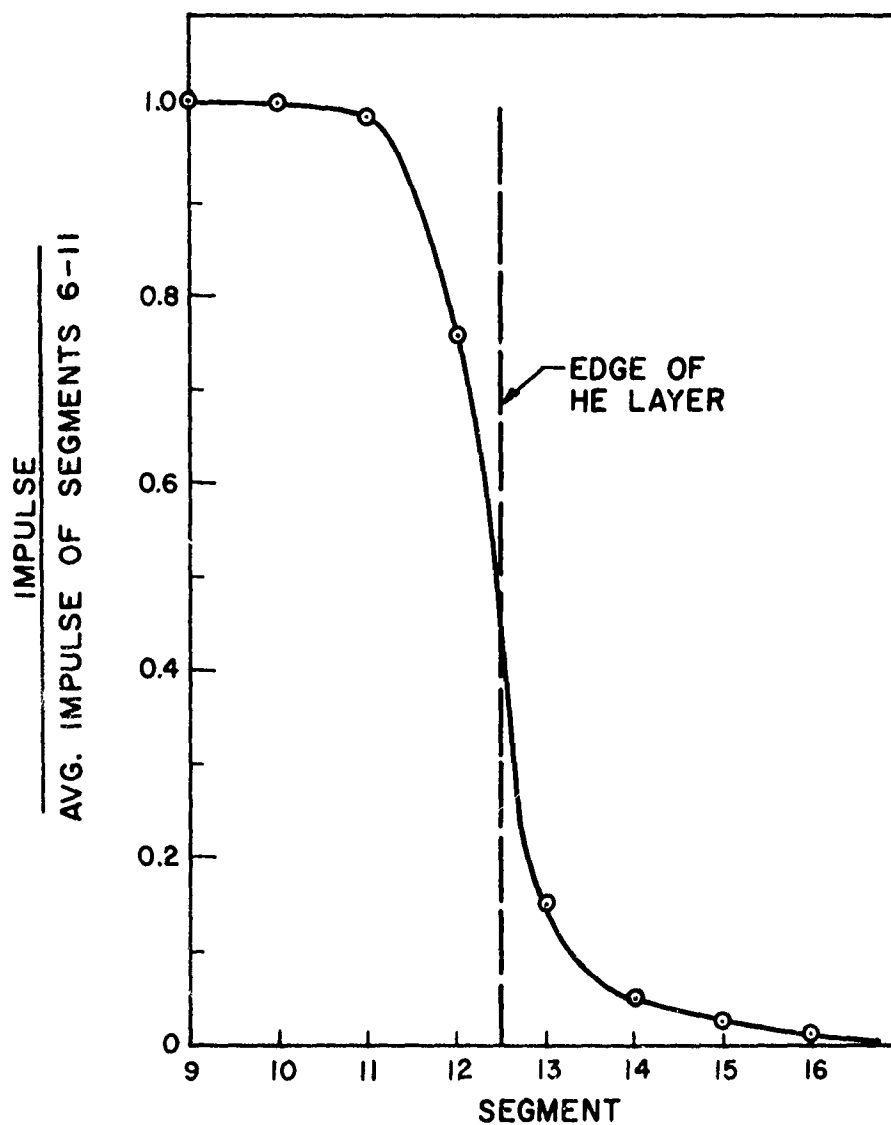
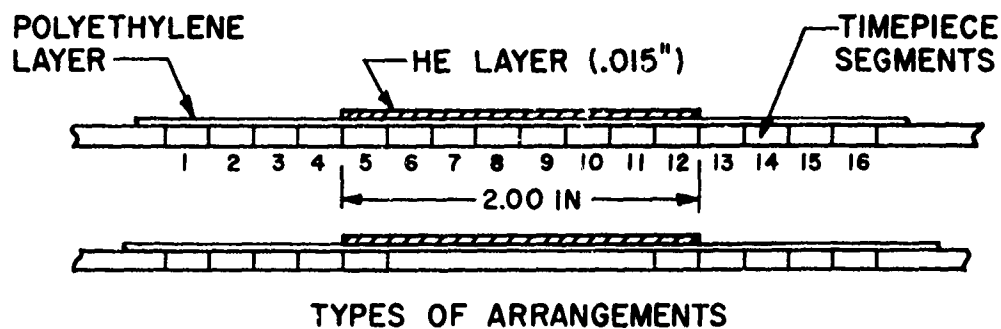
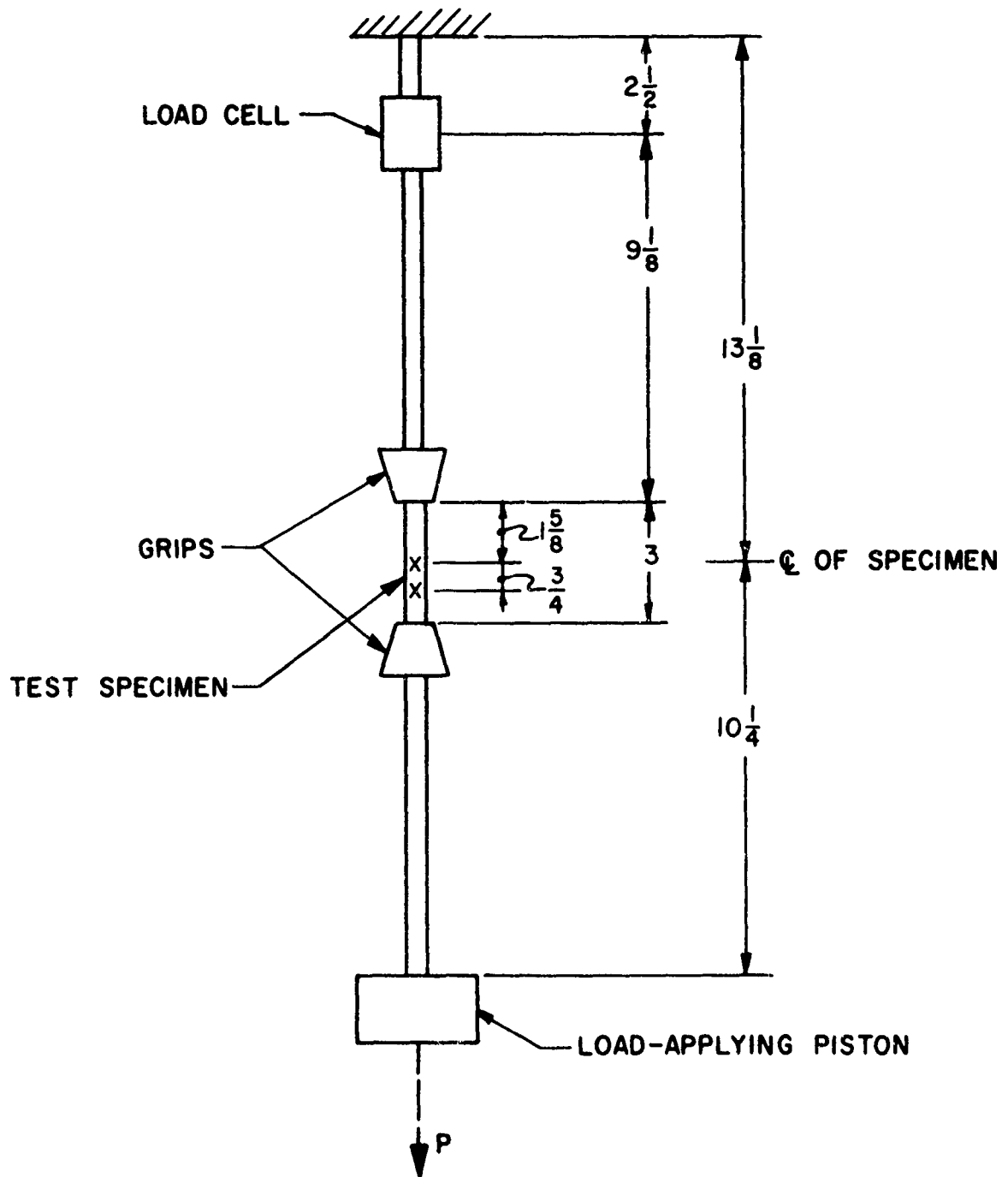
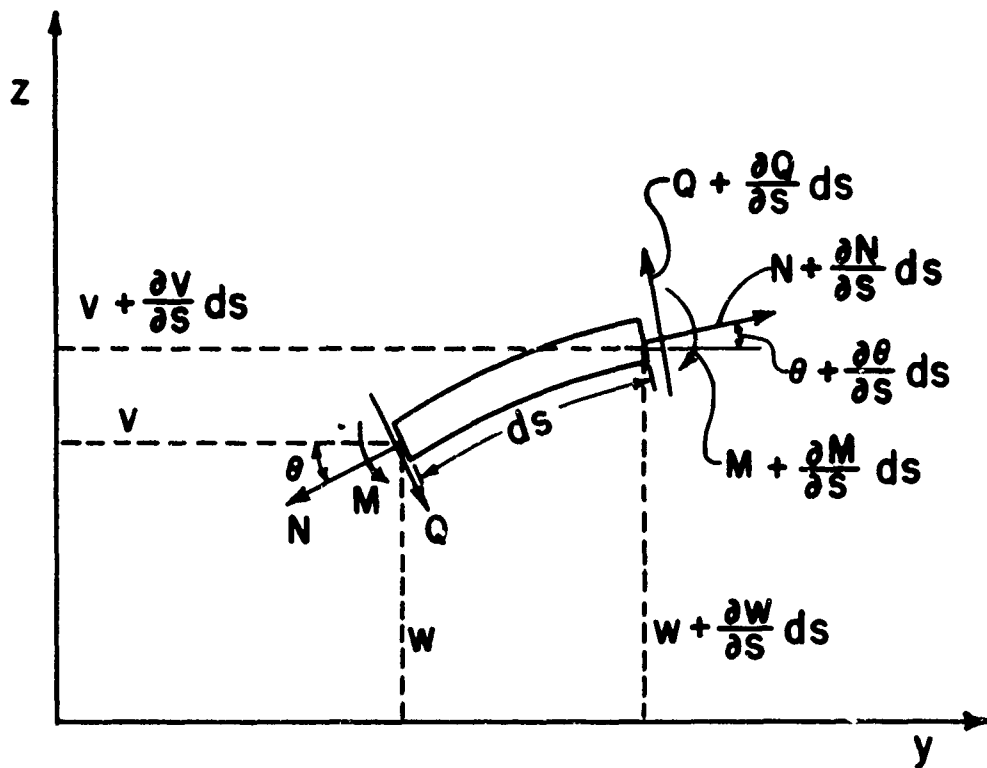


FIG. 2.2. HE EDGE EFFECTS ON THE SPANWISE DISTRIBUTION OF IMPARTED IMPULSE

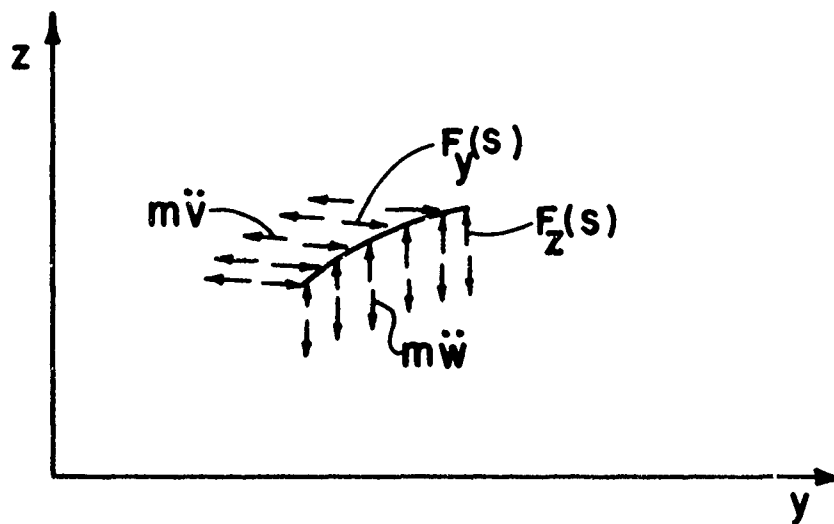


X DENOTES LOCATIONS OF  
STRAIN GAGE PAIRS

FIG. 2.3. SCHEMATIC OF ARRANGEMENT FOR MEASURING DYNAMIC  
STRESS-STRAIN PROPERTIES



(a) INTERNAL FORCES



(b) EXTERNAL FORCES

FIG. 3.1. NOMENCLATURE FOR A TWO-DIMENSIONAL STRUCTURE

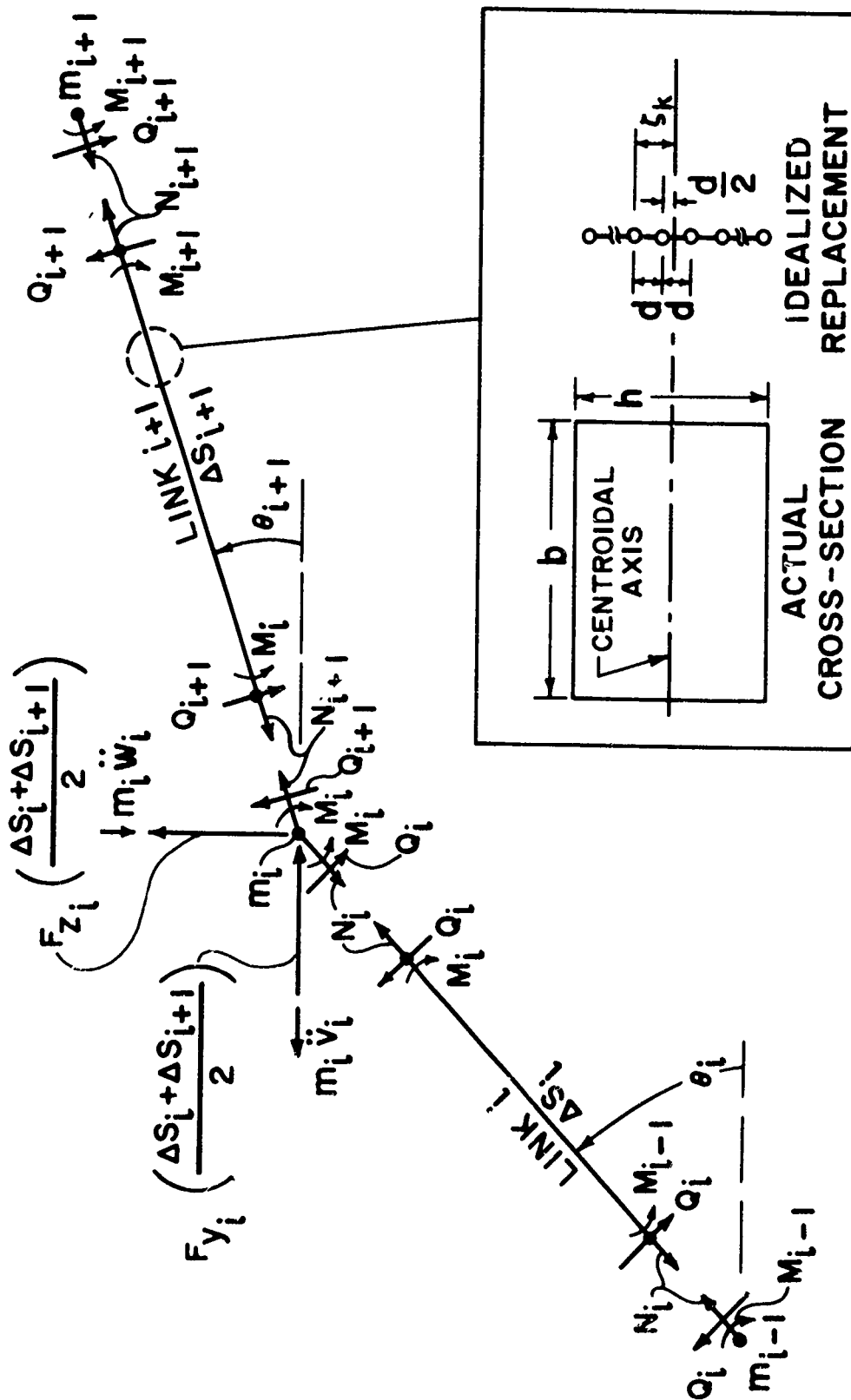


FIG. 3.2. LUMPED-PARAMETER AND IDEALIZED-THICKNESS MODEL

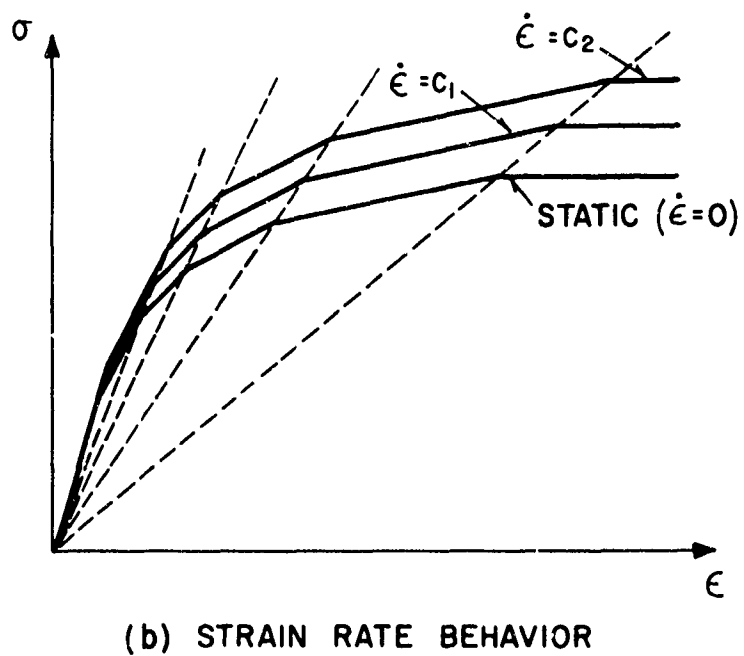
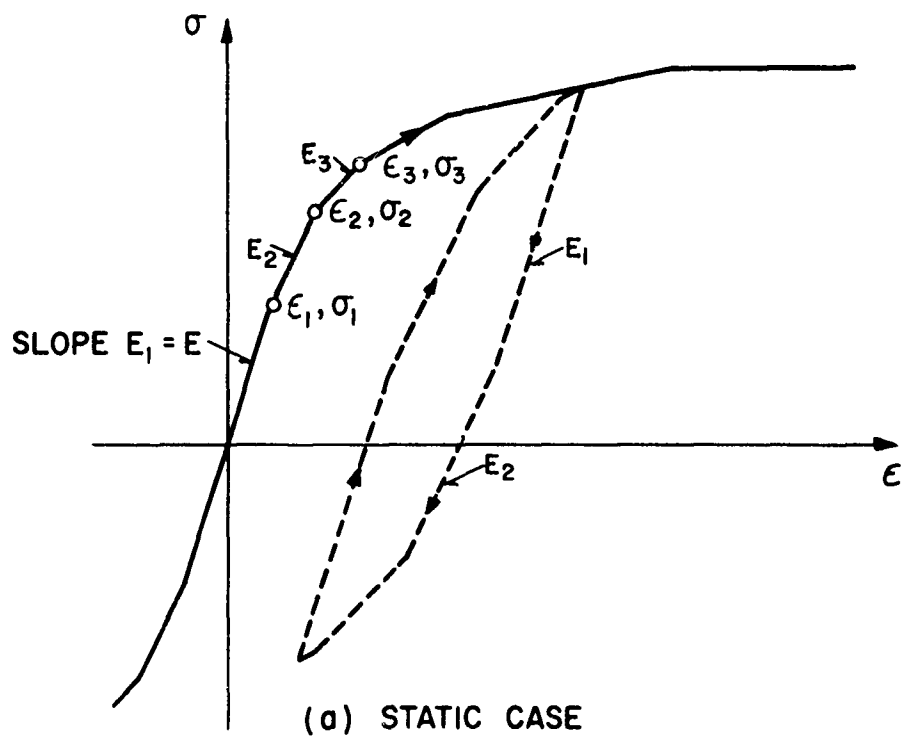
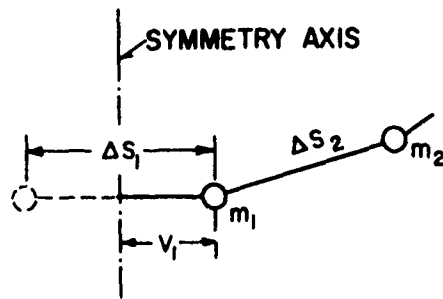
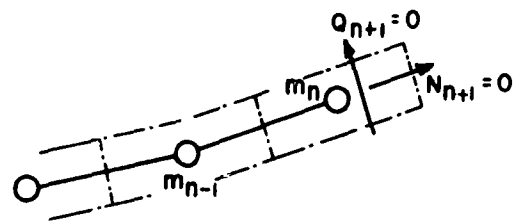


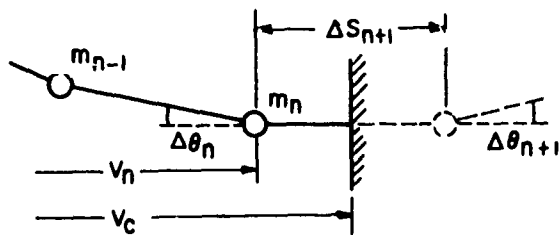
FIG. 3.3. IDEALIZED STRESS-STRAIN RELATIONS



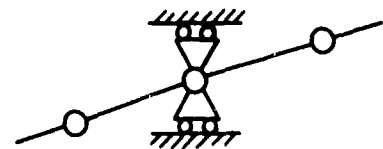
(a) SYMMETRY CONDITION



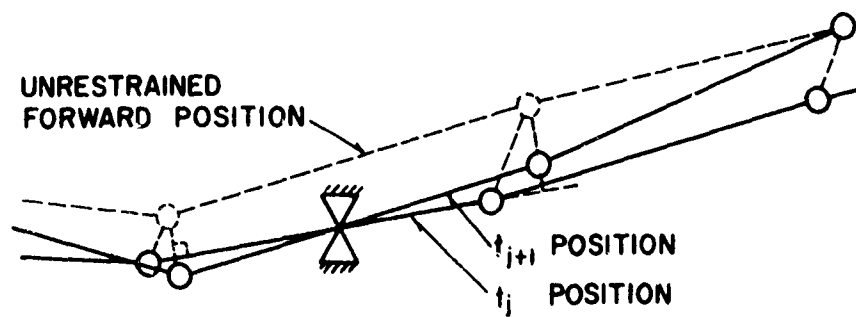
(b) FREE-END



(c) CLAMPED END

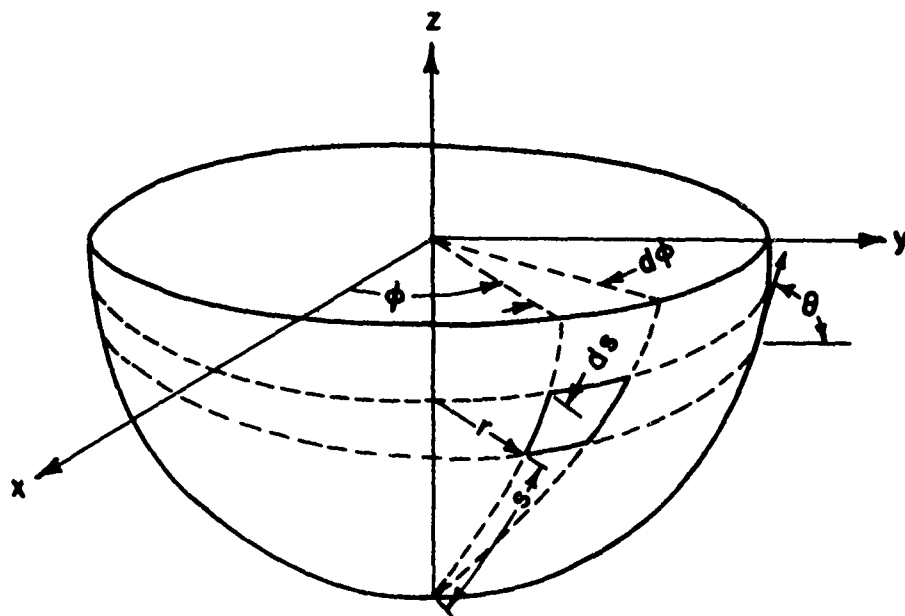


(d) SIMPLE SUPPORT

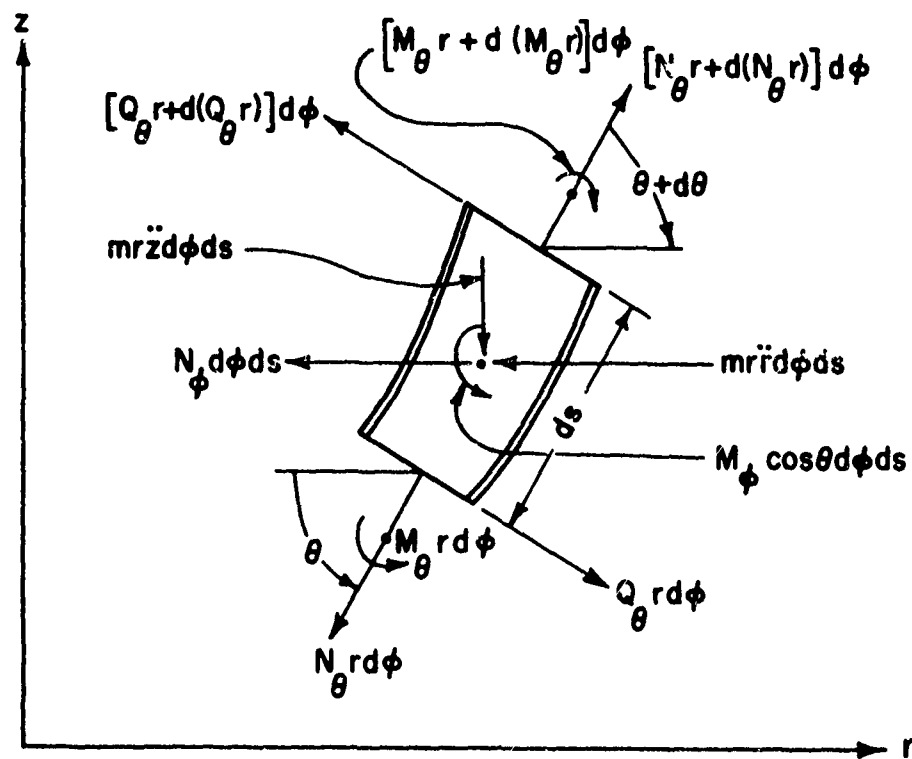


(e) FIXED KNIFE EDGES

FIG. 3.4. BOUNDARY CONDITIONS



(a) SHELL OF REVOLUTION



(b) EQUILIBRIUM OF A SHELL ELEMENT

FIG. 3.5. NOMENCLATURE FOR A SHELL OF REVOLUTION

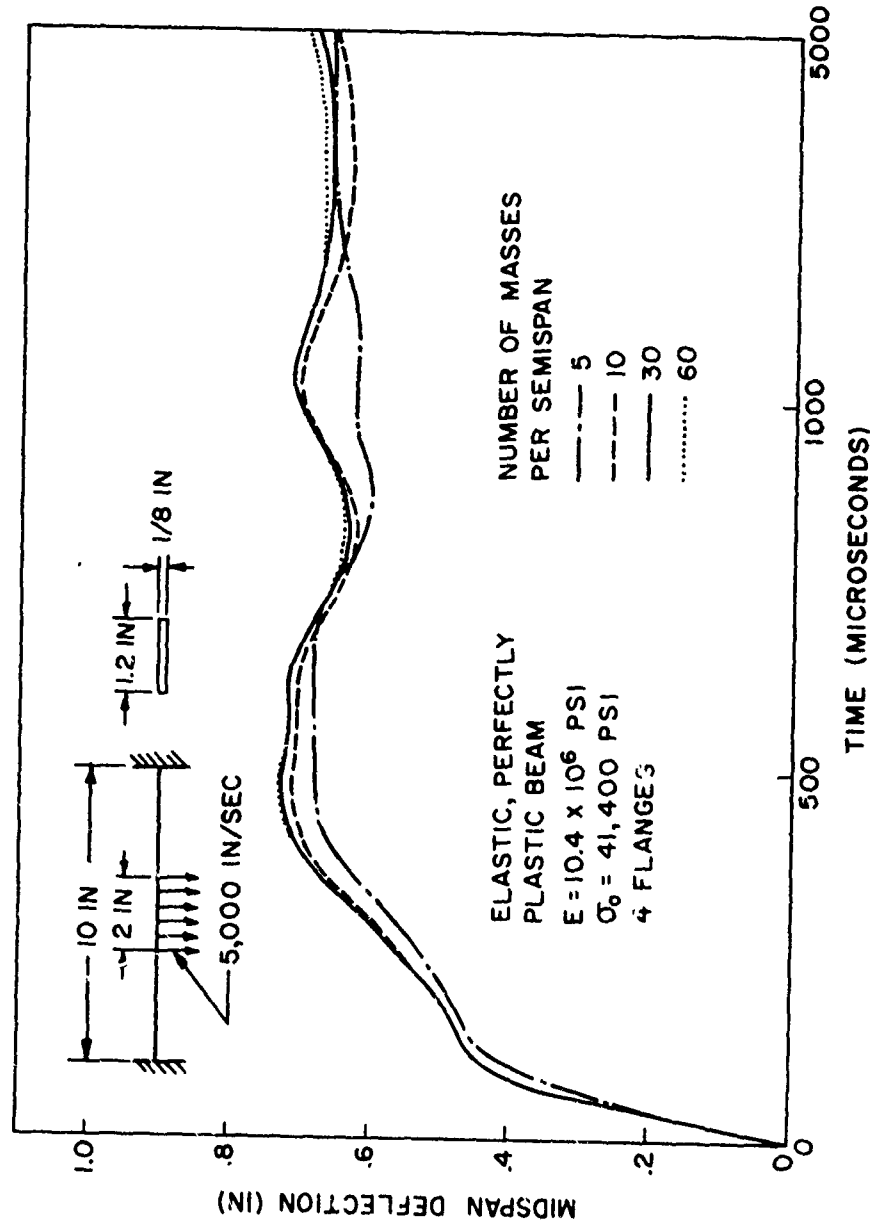


FIG. 3.6. EFFECT OF SPACE MESH SIZE ON DYNAMIC RESPONSE OF A CLAMPED BEAM

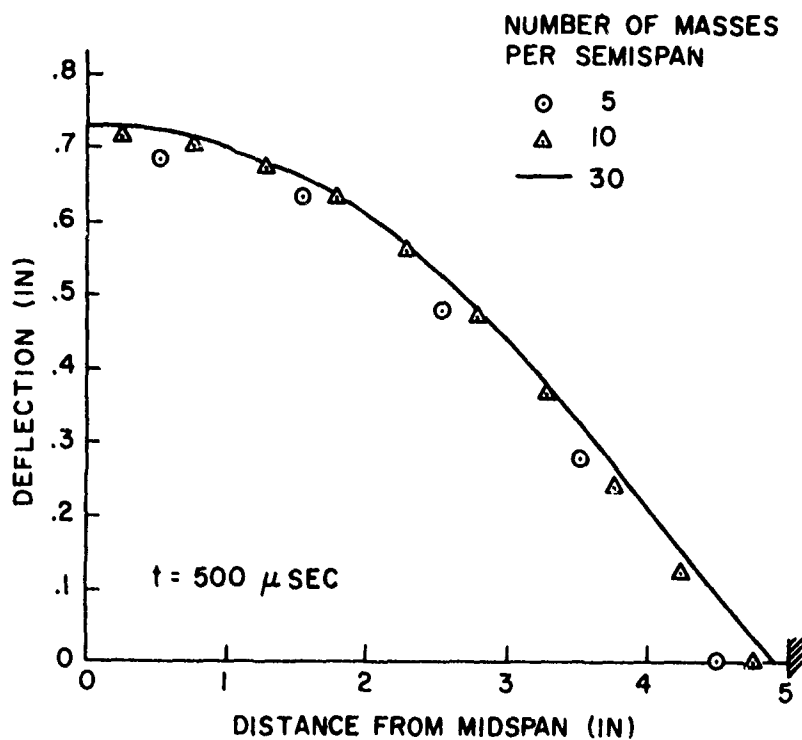
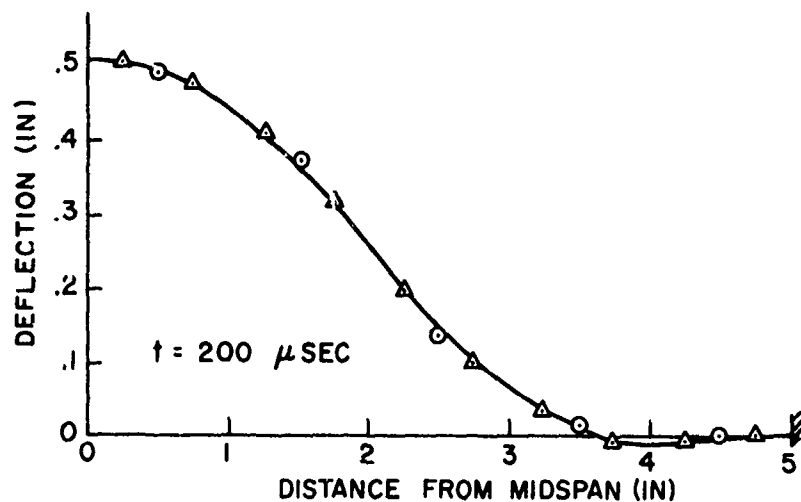


FIG. 3.7. EFFECT OF SPACE MESH SIZE ON DEFLECTION PROFILES OF A CLAMPED BEAM

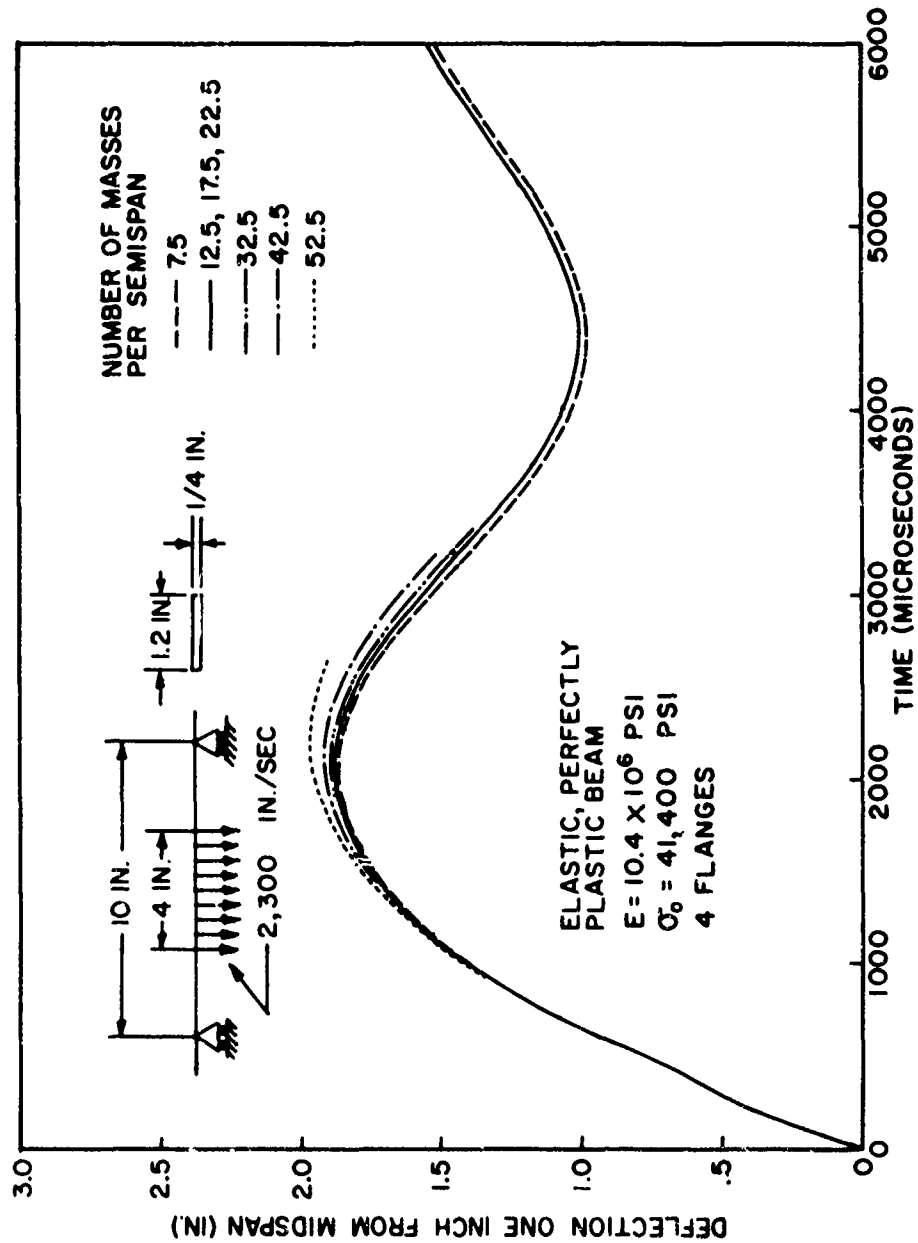


FIG. 3.8. EFFECT OF SPACE MESH SIZE ON DYNAMIC RESPONSE OF A SIMPLY-SUPPORTED BEAM

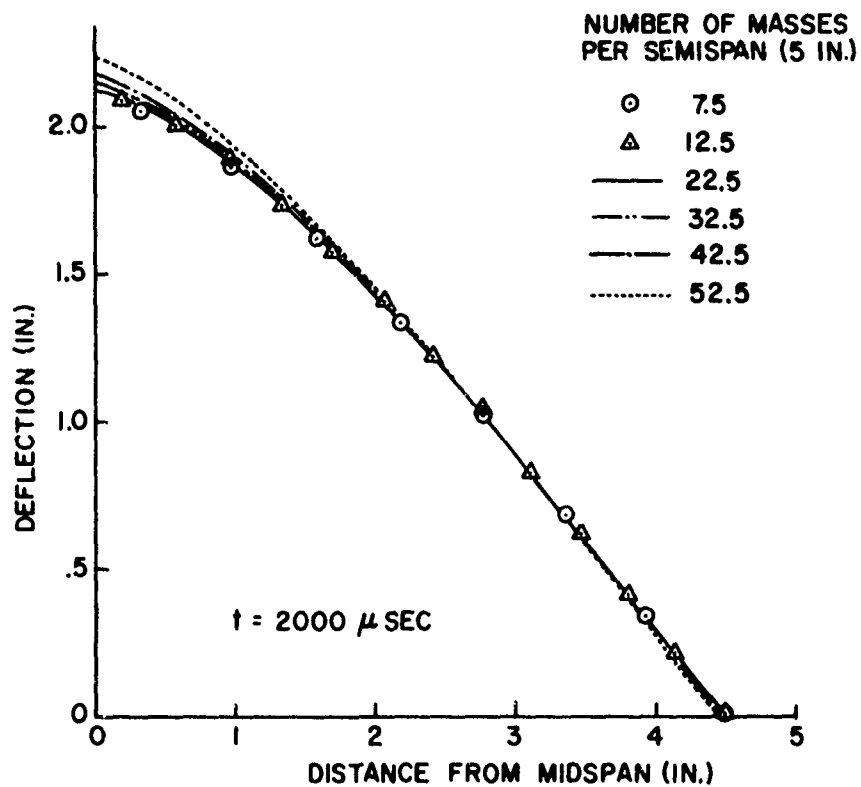
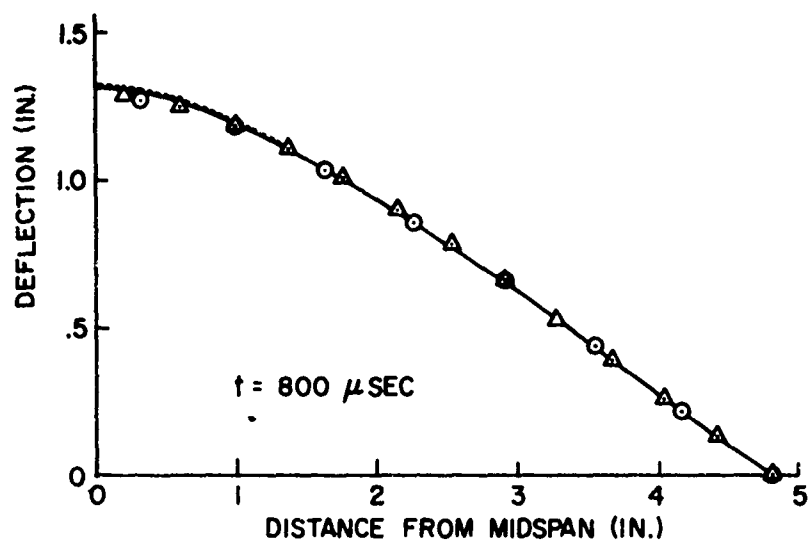


FIG. 3.9. EFFECT OF SPACE MESH SIZE ON DEFLECTION PROFILES OF A SIMPLY-SUPPORTED BEAM

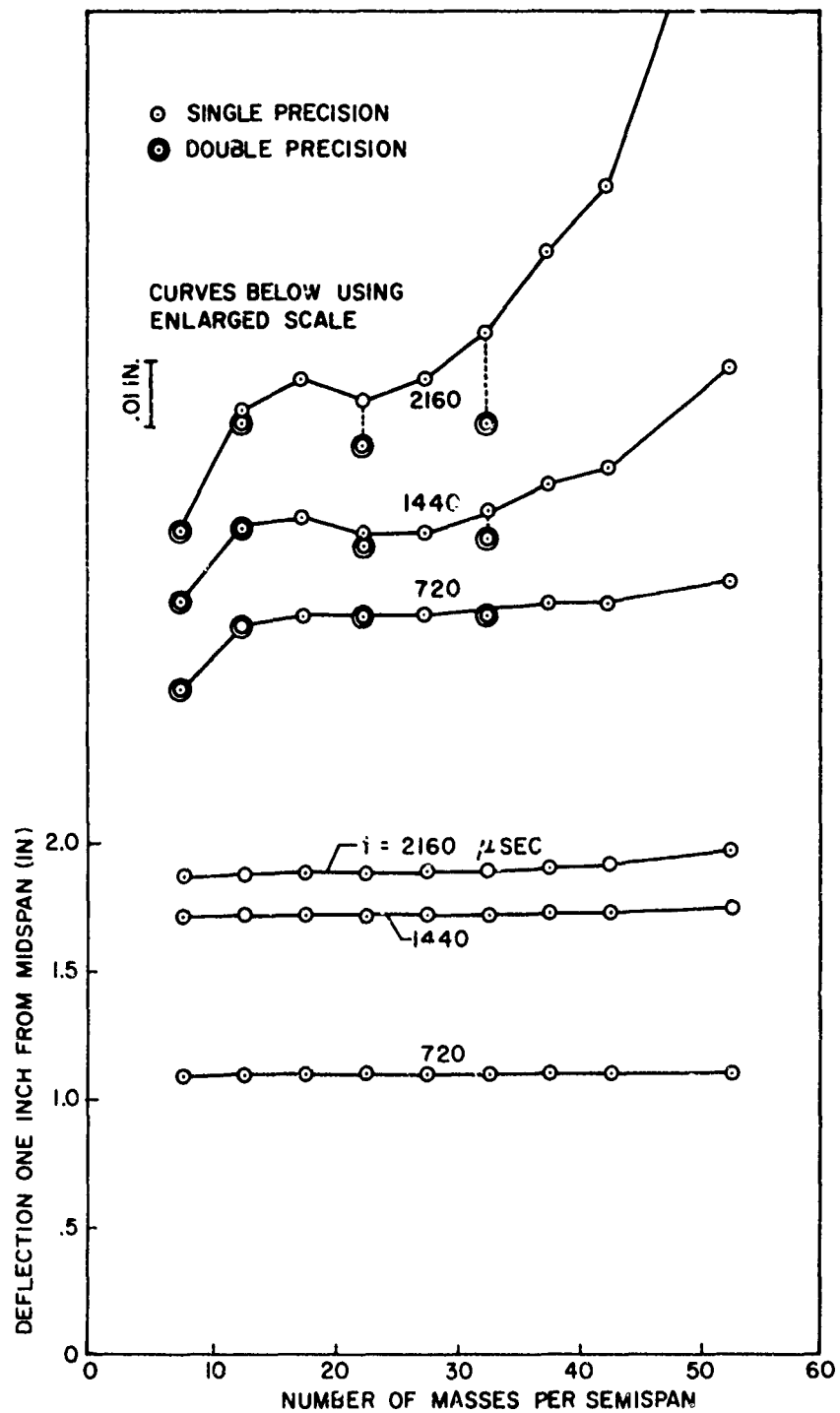


FIG. 3.10. DEFLECTION OF A SELECTED SPANWISE POINT AS A FUNCTION OF NUMBER OF MASSES FOR A SIMPLY-SUPPORTED BEAM

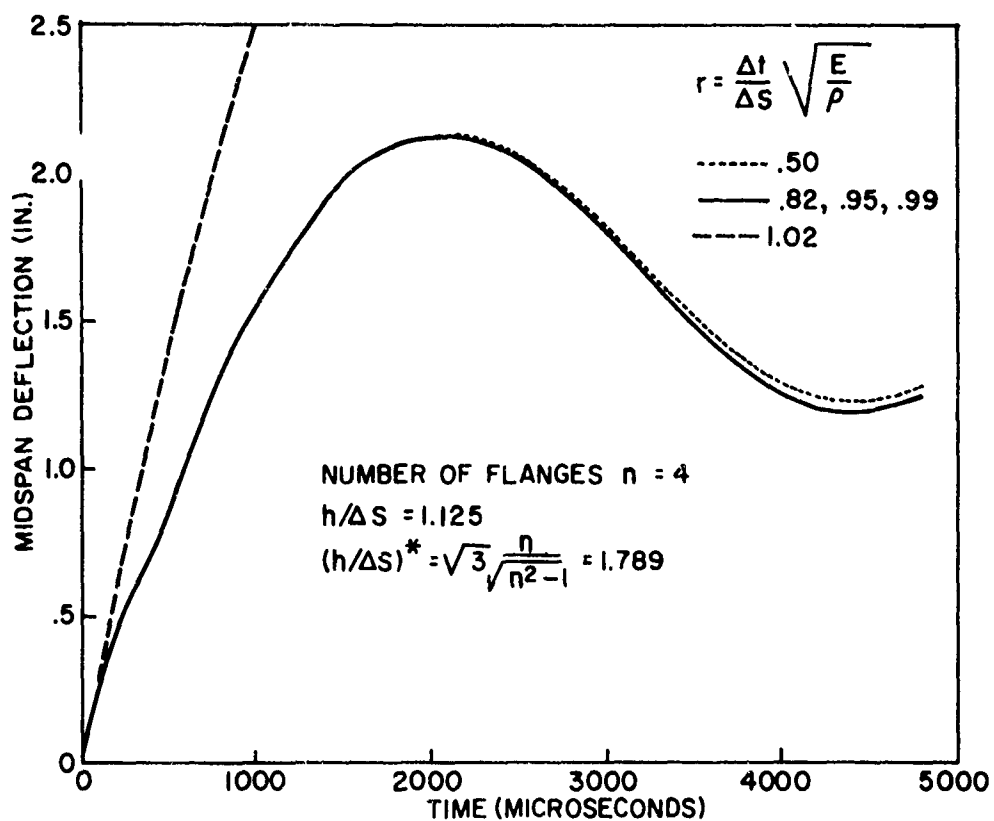


FIG. 3.11. EFFECT OF CALCULATION TIME INTERVAL ON DYNAMIC RESPONSE OF A SIMPLY-SUPPORTED BEAM

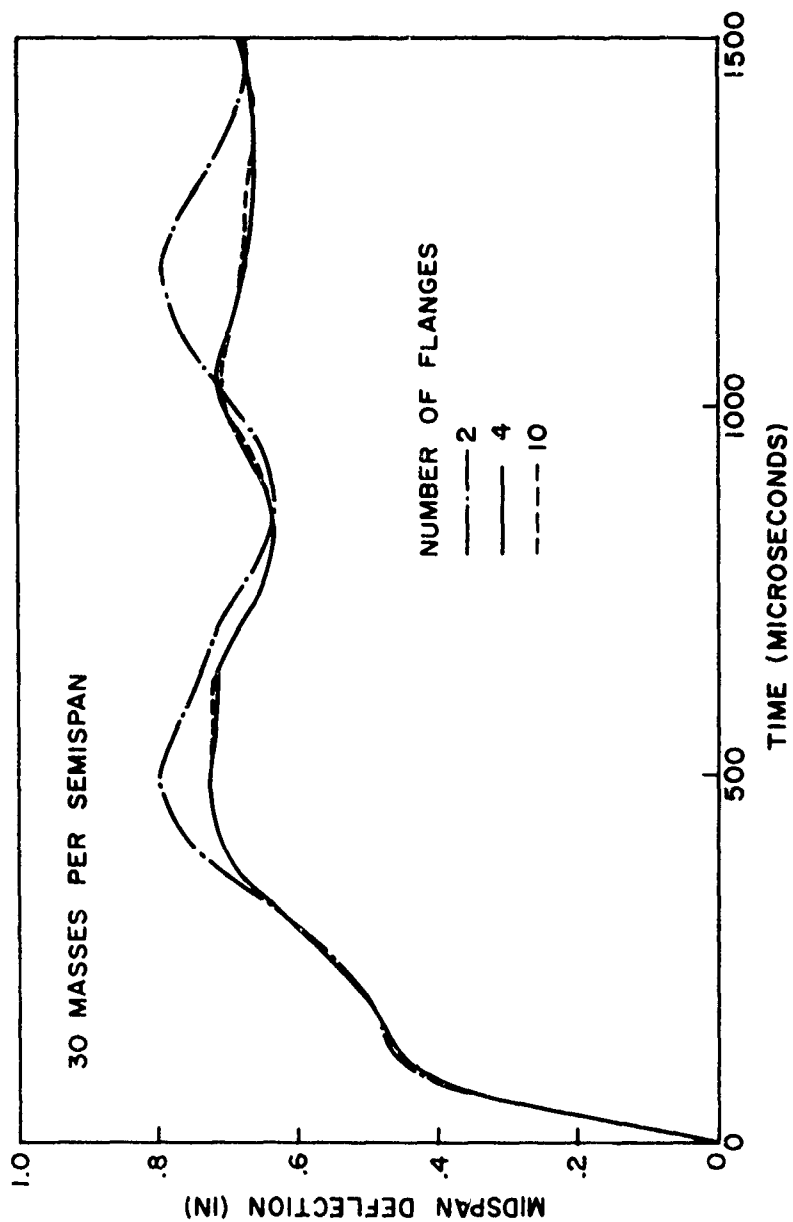


FIG. 3.12. EFFECT OF NUMBER OF FLANGES OF IDEALIZED-THICKNESS MODEL ON DYNAMIC RESPONSE OF A CLAMPED BEAM

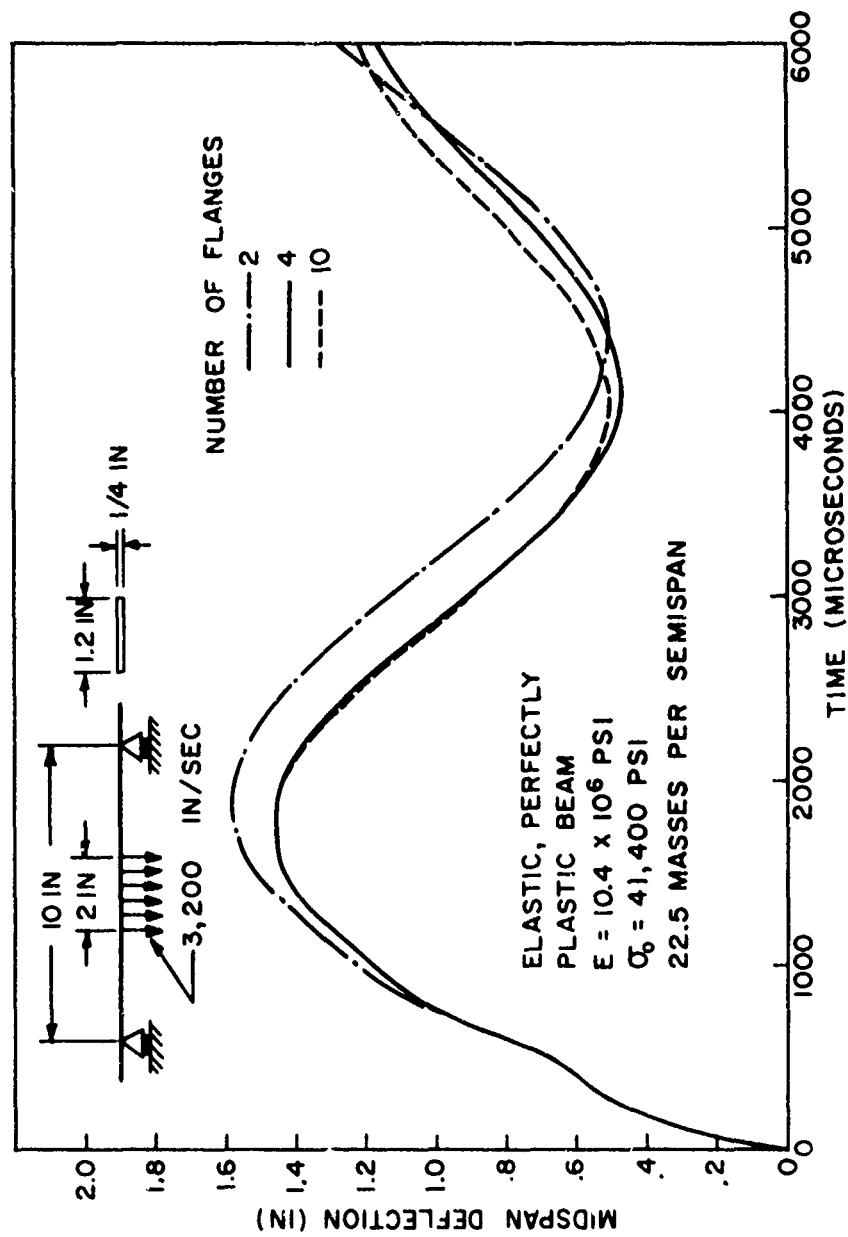


FIG. 3.13. EFFECT OF NUMBER OF FLANGES OF IDEALIZED-THICKNESS MODEL ON DYNAMIC RESPONSE OF A SIMPLY-SUPPORTED BEAM

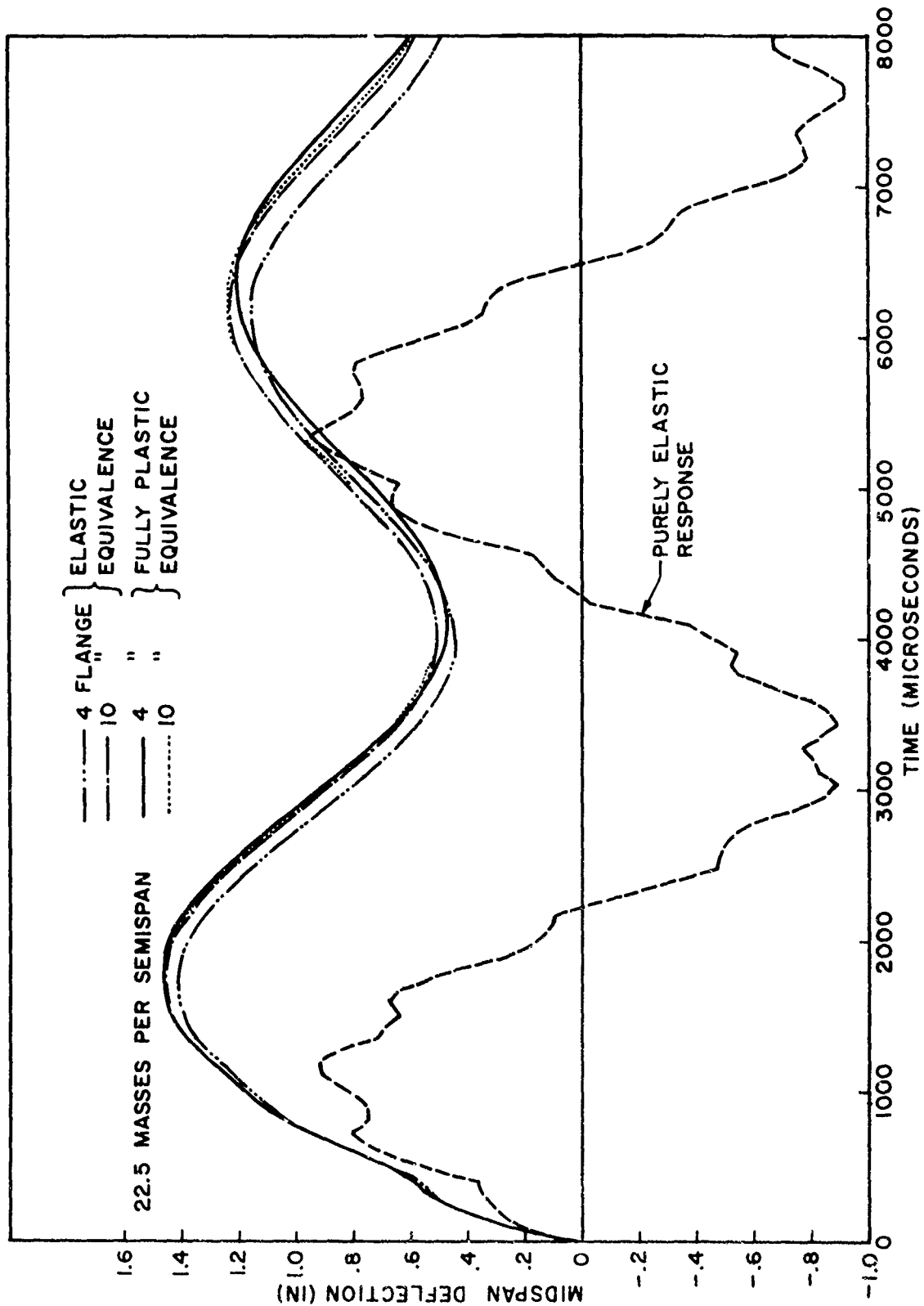
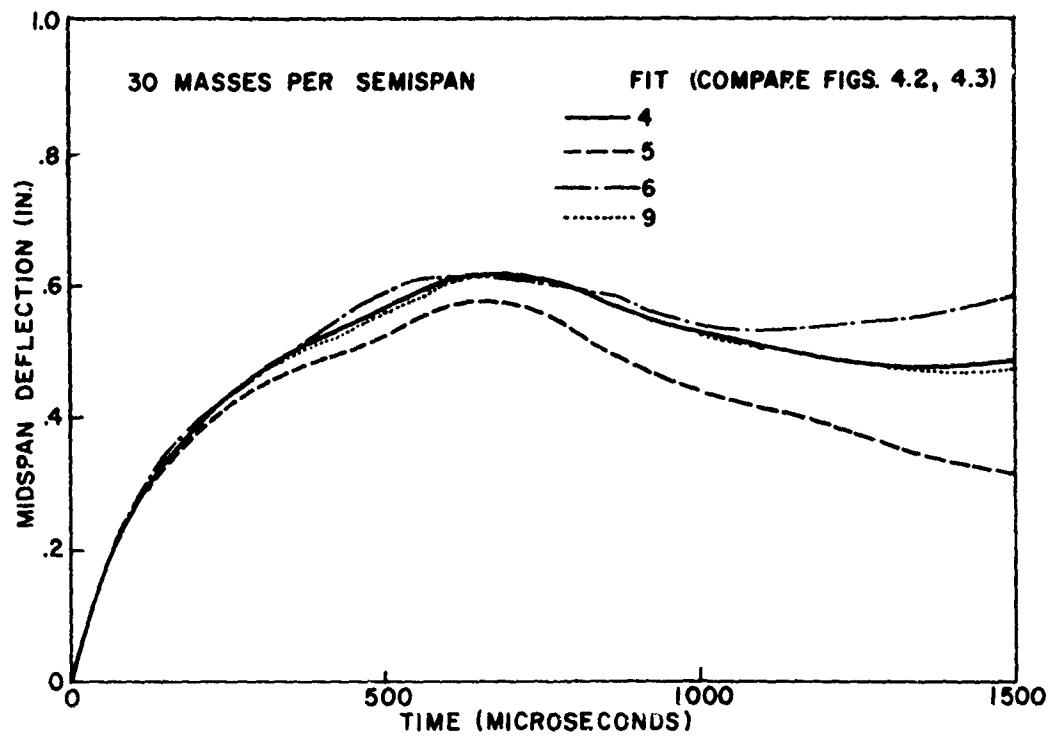
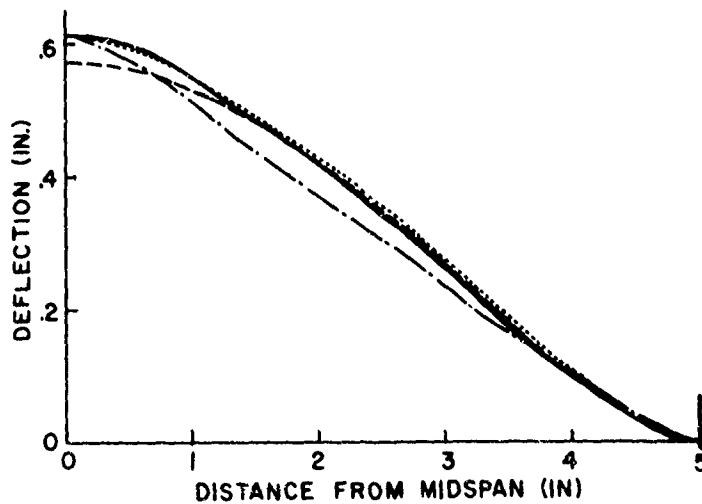


FIG. 3.14. EFFECT OF FLANGE SPACING ON DYNAMIC RESPONSE OF A SIMPLY-SUPPORTED BEAM

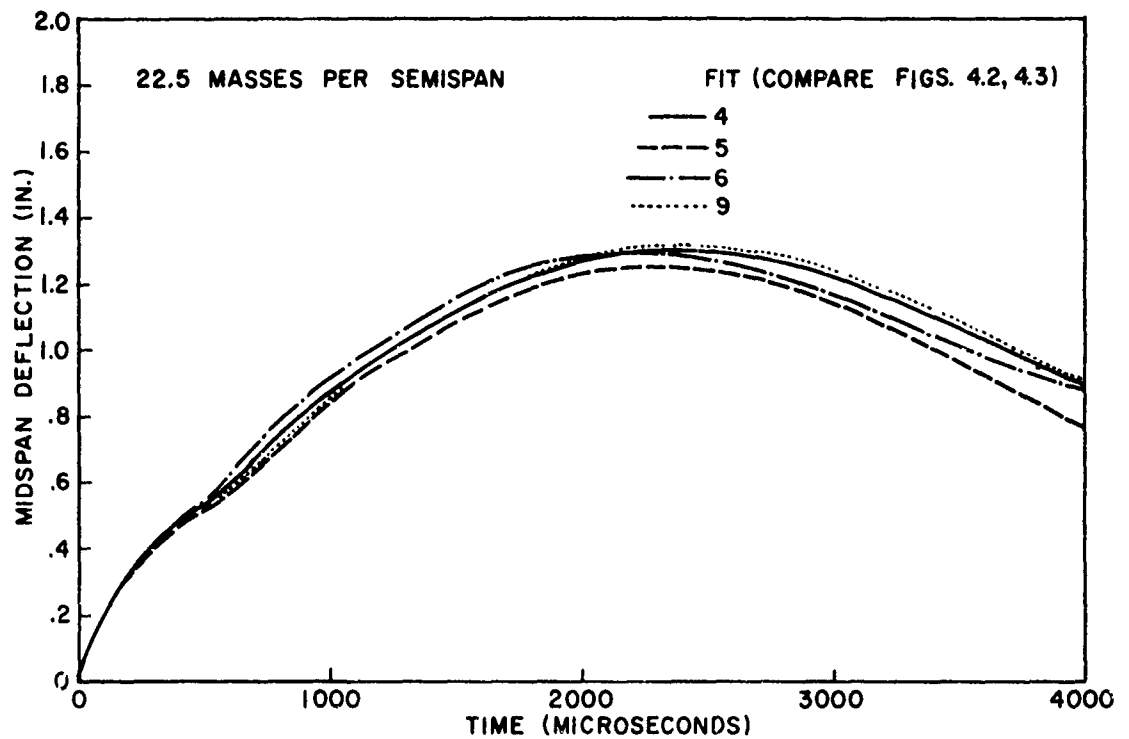


(a) MIDSPAN DEFLECTION TIME HISTORY

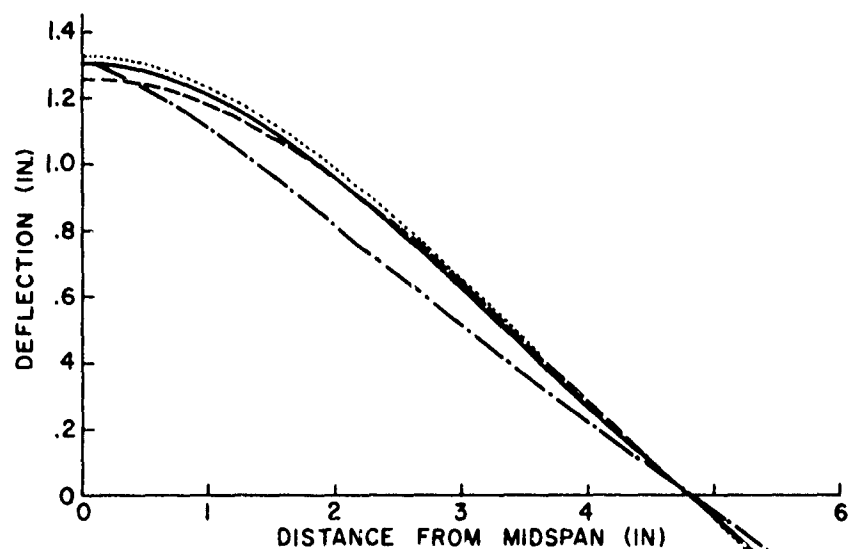


(b) DEFLECTION PROFILE AT TIME OF  
MAXIMUM MIDSPAN DEFLECTION

FIG. 3.15 EFFECT OF DIFFERENT STRESS-STRAIN CURVE FITS ON  
DYNAMIC RESPONSE OF A CLAMPED BEAM

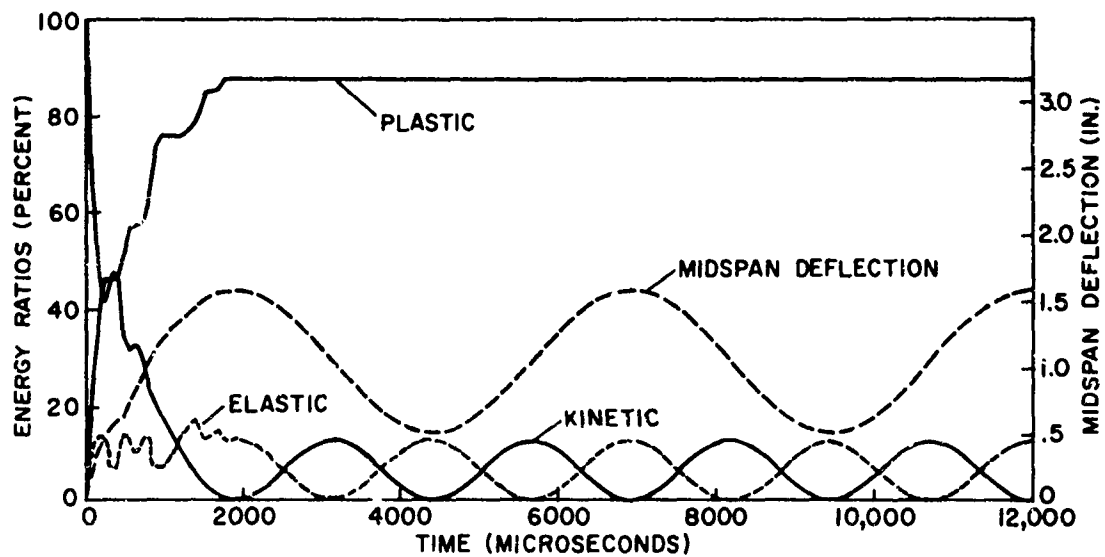


(a) MIDSPAN DEFLECTION TIME HISTORY

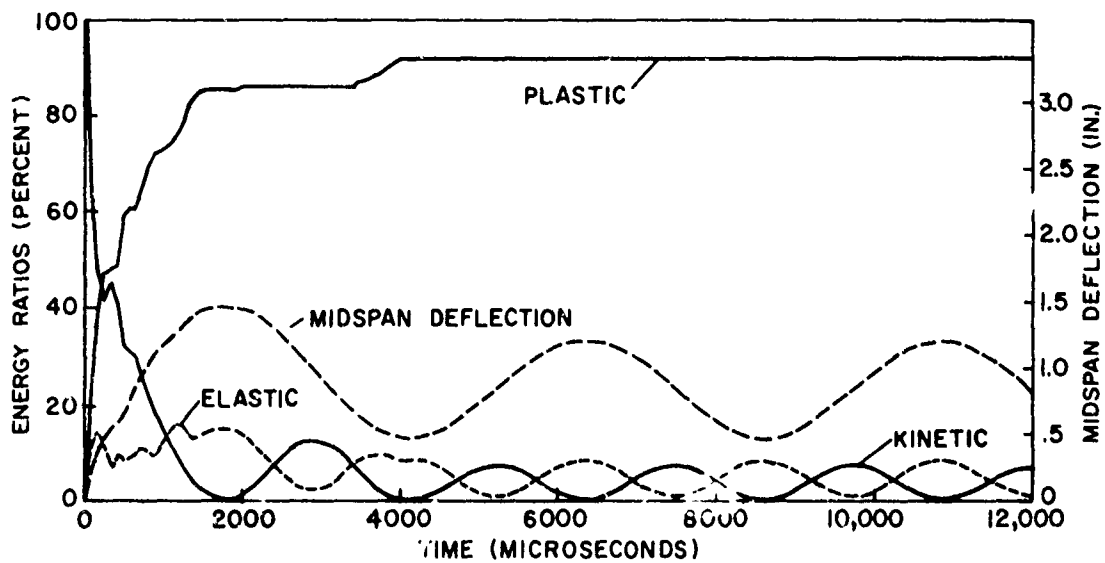


(b) DEFLECTION PROFILE AT TIME OF  
 MAXIMUM MIDSPAN DEFLECTION

FIG. 3.16. EFFECT OF DIFFERENT STRESS-STRAIN CURVE FITS ON  
 DYNAMIC RESPONSE OF A SIMPLY-SUPPORTED BEAM



(a) 2-FLANGE MODEL



(b) 4-FLANGE MODEL

FIG. 3.17. RATIOS OF ENERGIES TO INITIALLY-IMPARTED KINETIC ENERGY FOR A SIMPLY-SUPPORTED BEAM

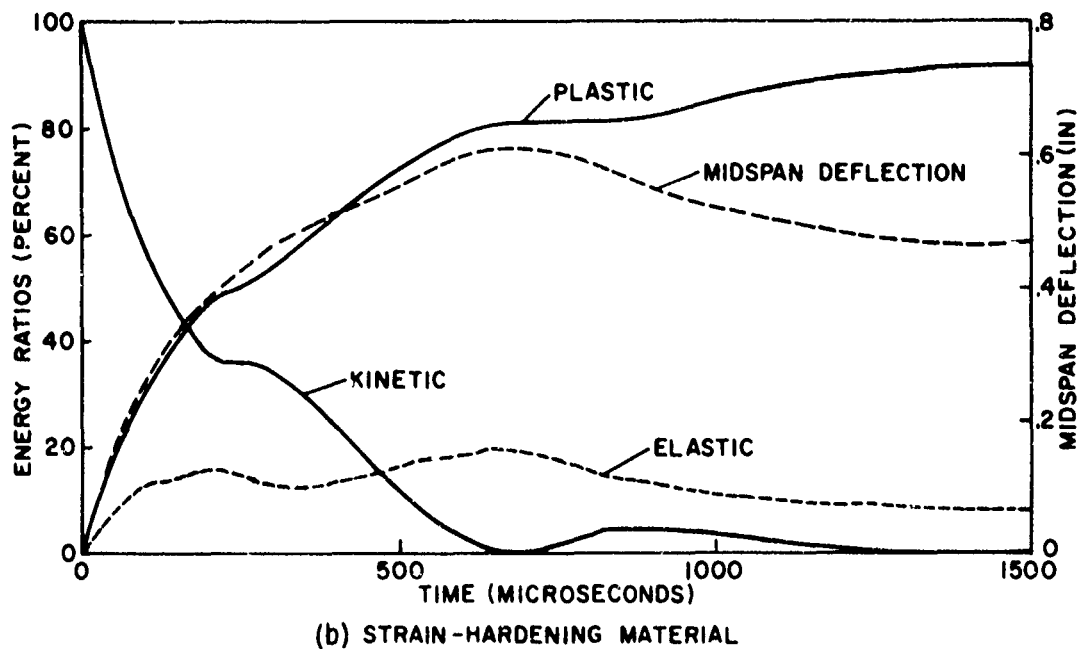
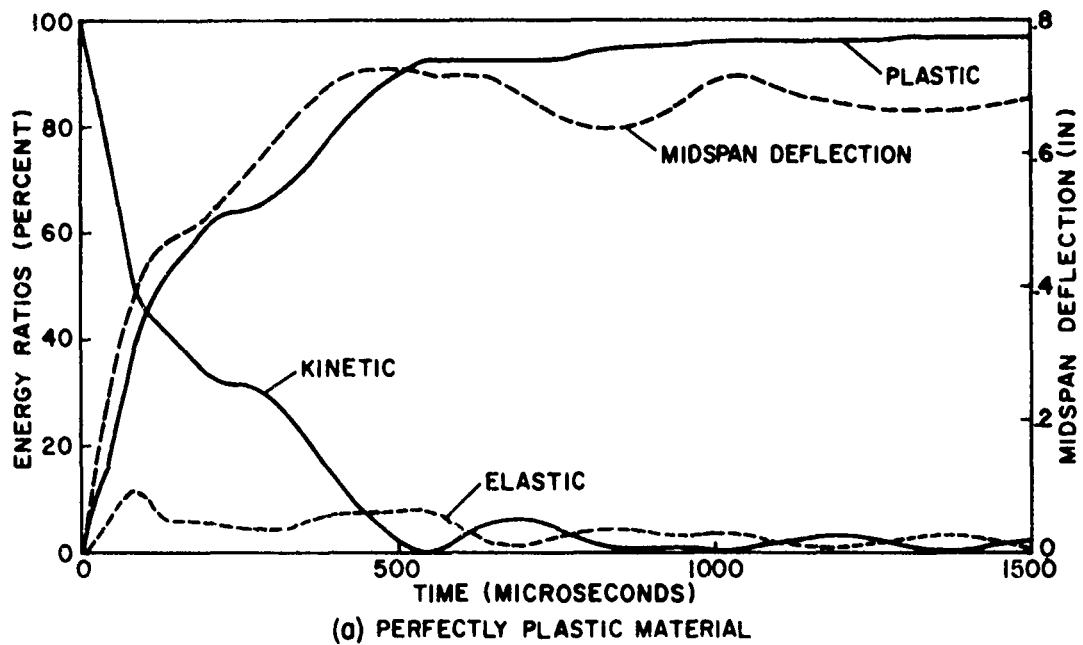


FIG. 3.18. RATIOS OF ENERGIES TO INITIALLY-IMPARTED KINETIC ENERGY FOR A CLAMPED BEAM

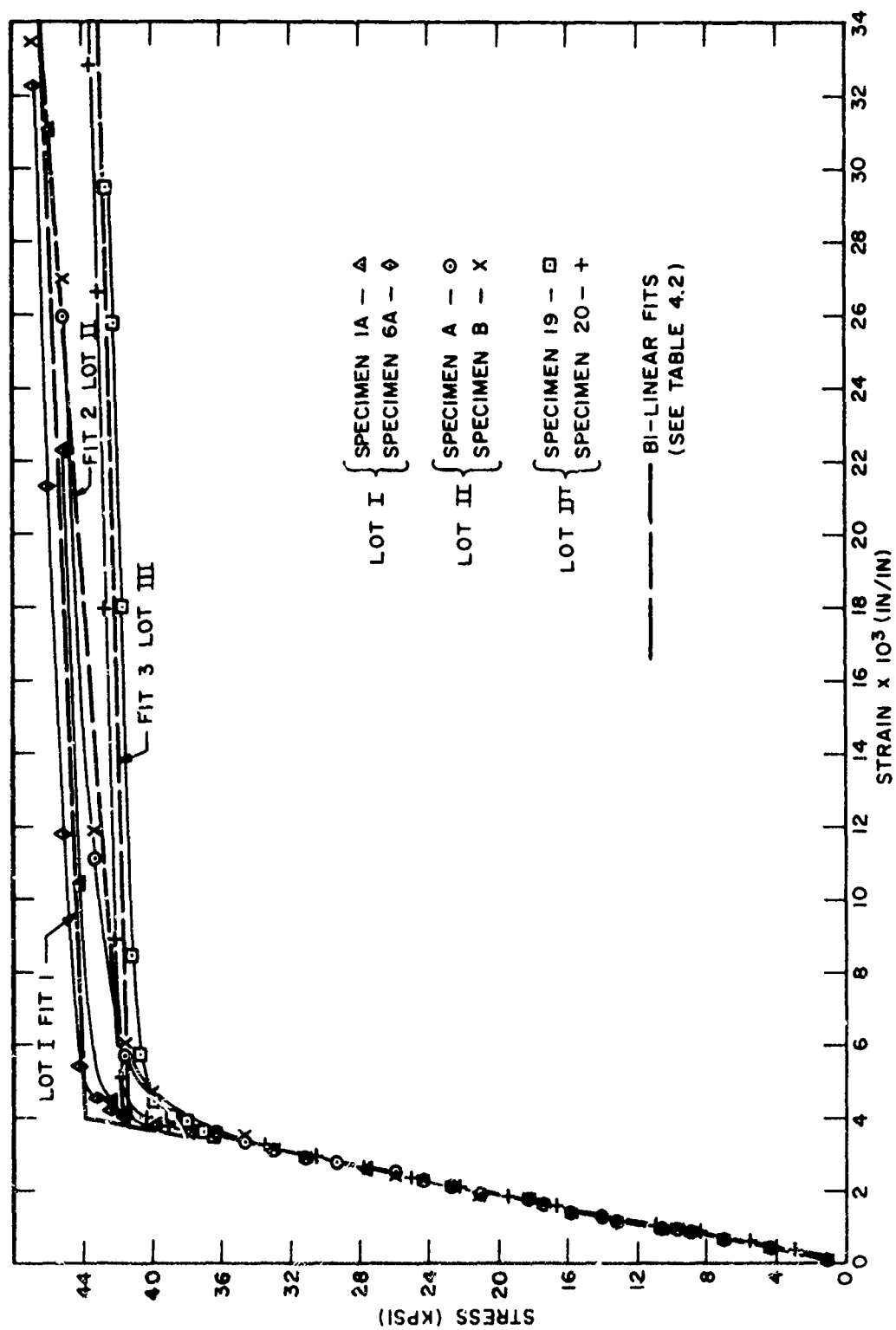


FIG. 4.1. MEASURED AND FITTED STATIC STRESS-STRAIN PROPERTIES OF 6061-T6 ALUMINUM BEAM MATERIALS

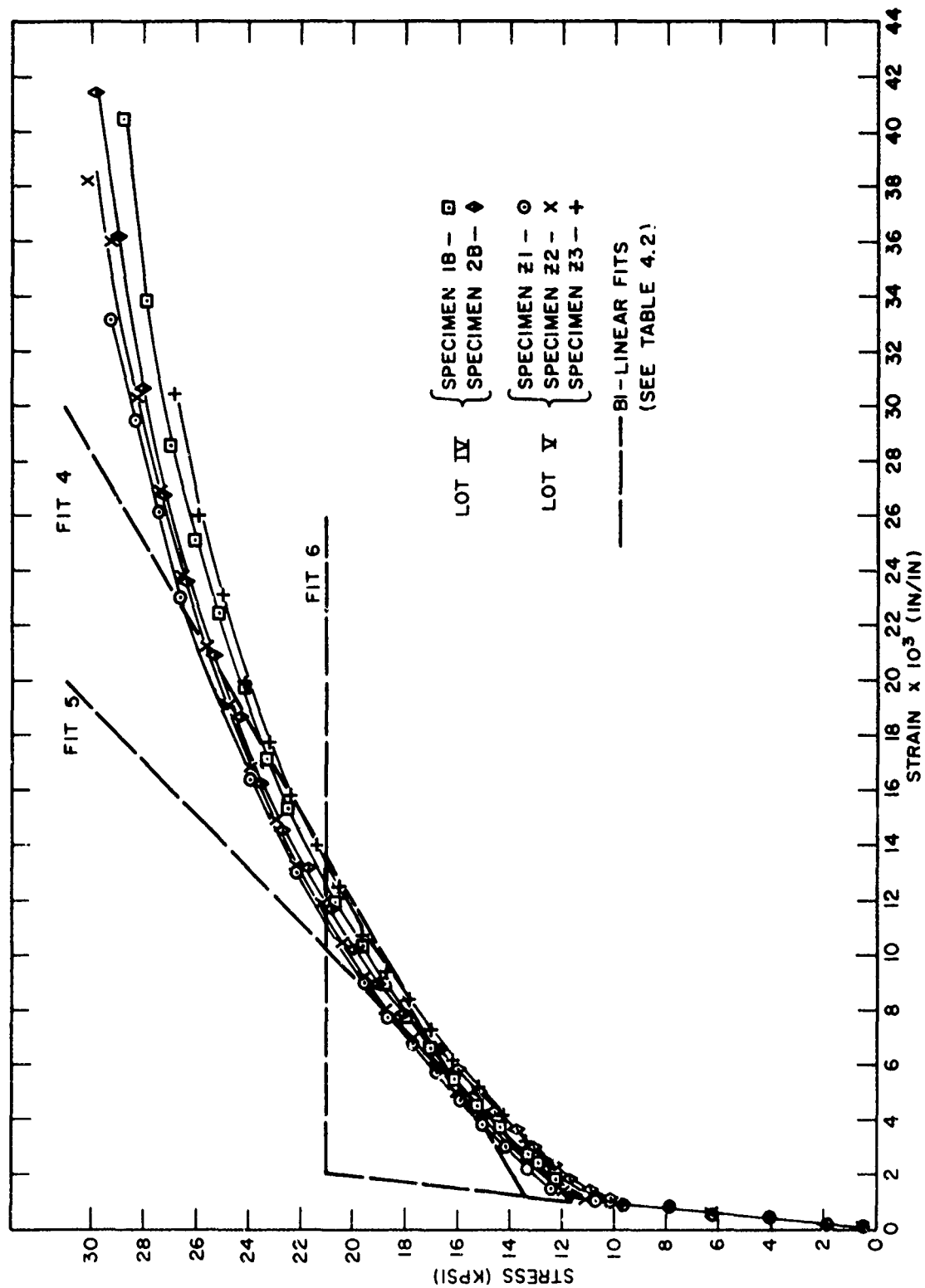


FIG. 4.2. MEASURED AND FITTED STATIC STRESS-STRAIN PROPERTIES OF 2024-T3 ALUMINUM BEAM MATERIALS

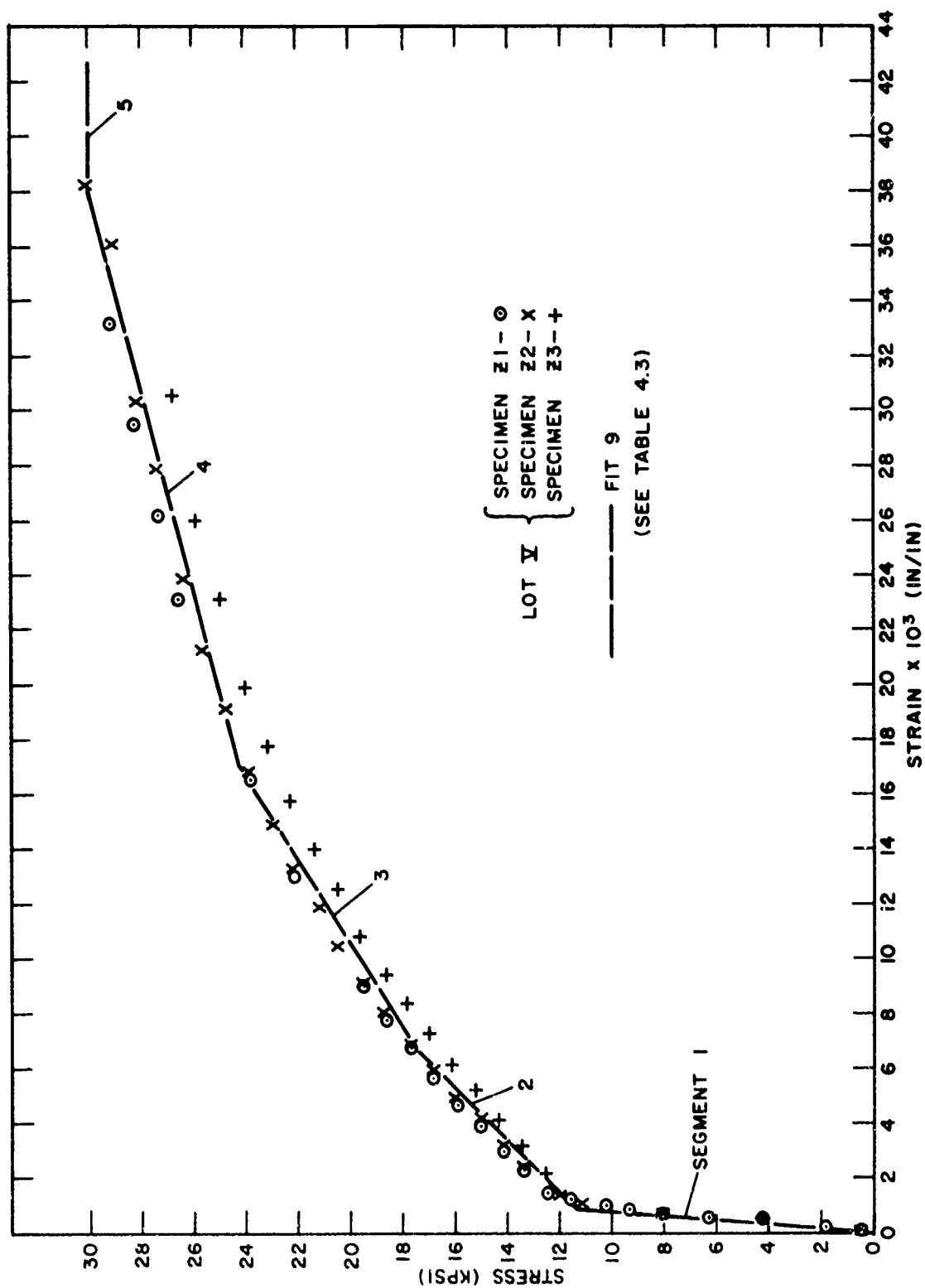


FIG. 4.3. FIVE-SEGMENT FIT OF STATIC STRESS-STRAIN PROPERTIES OF 2024-0 BEAM MATERIAL

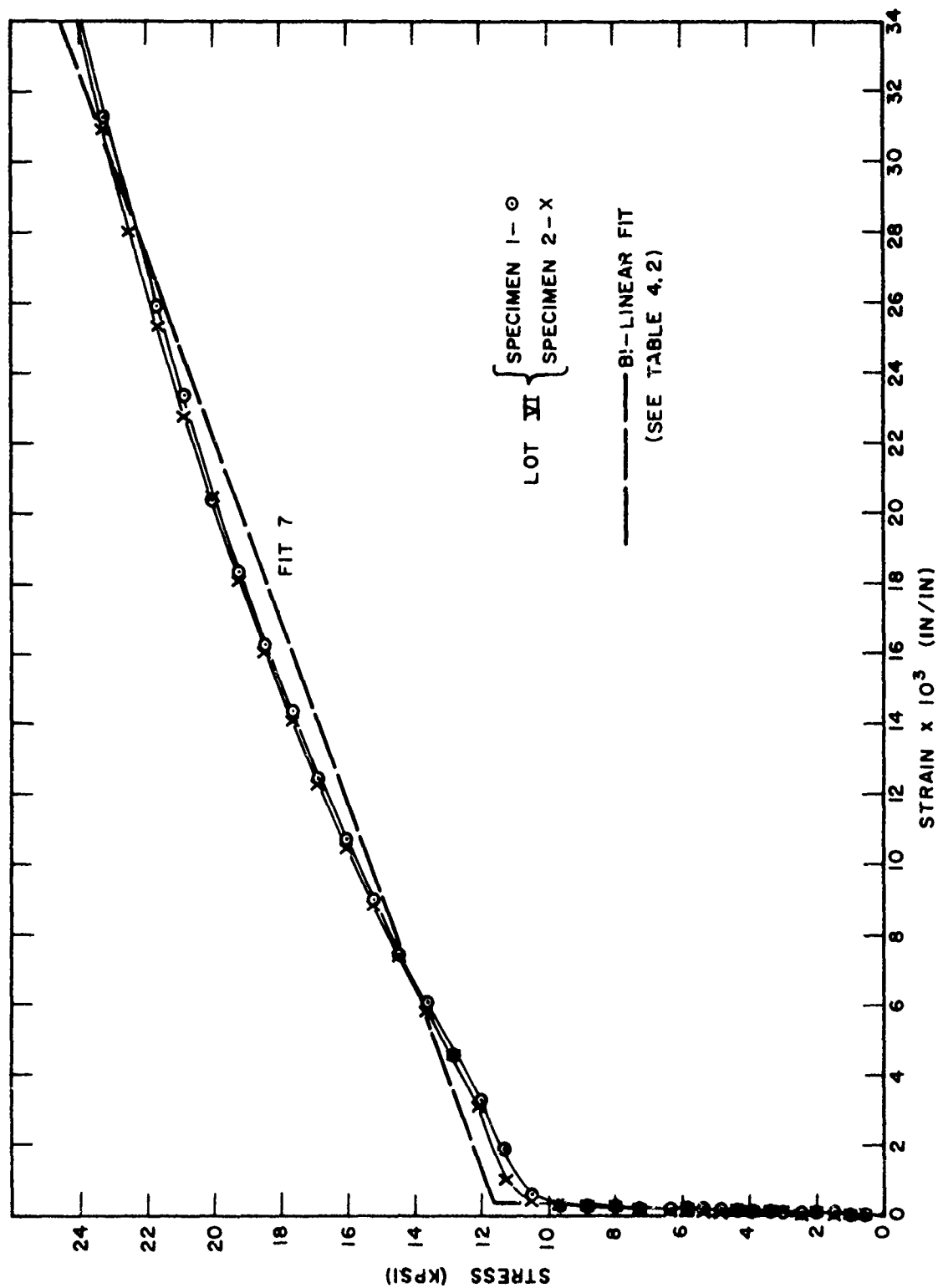


FIG. 4.4. MEASURED AND FITTED STATIC STRESS-STRAIN PROPERTIES OF 1010 STEEL BEAM MATERIAL

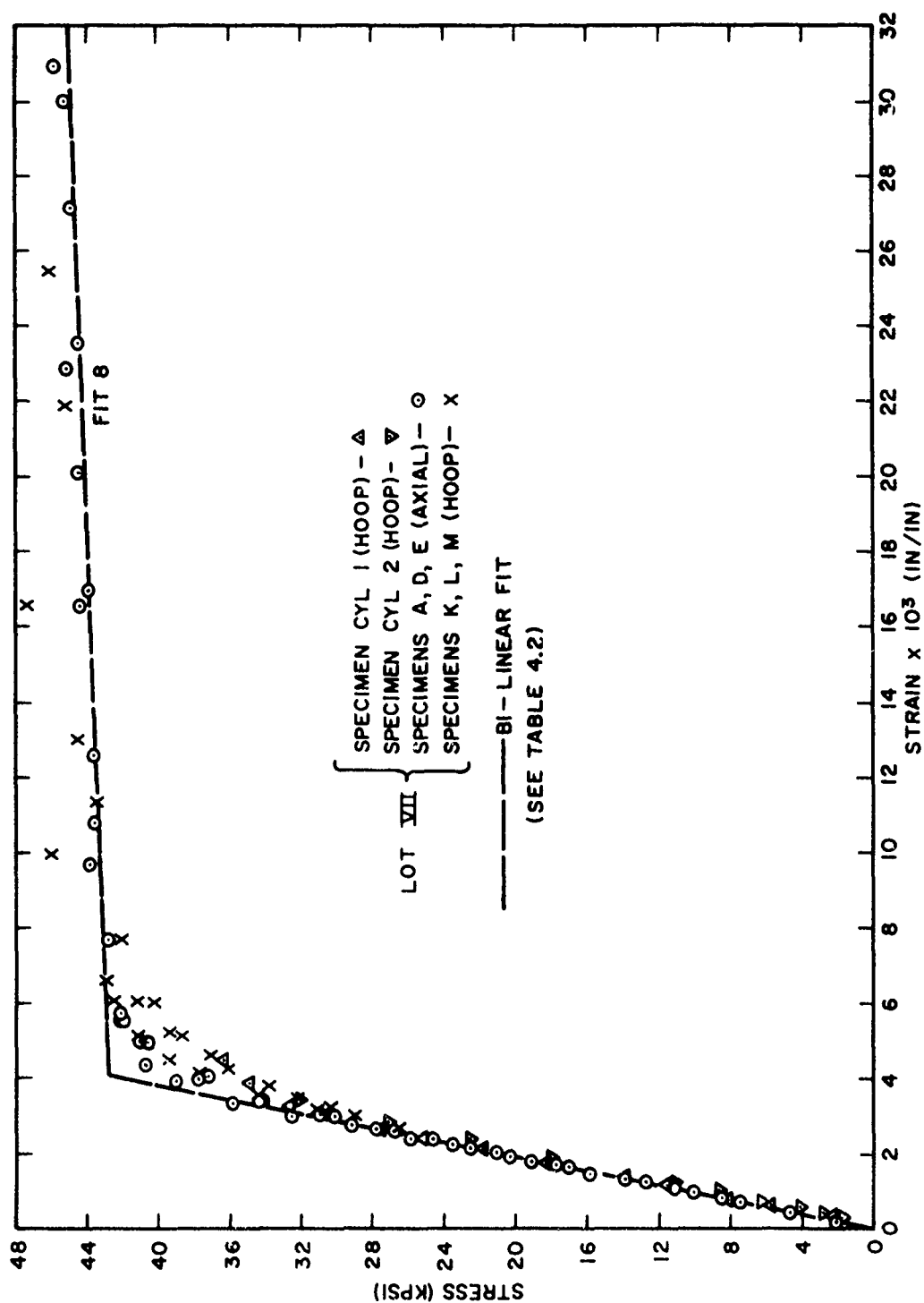


FIG. 4.5. MEASURED AND FITTED STATIC STRESS-STRAIN PROPERTIES OF 6061-T6 RING MATERIAL

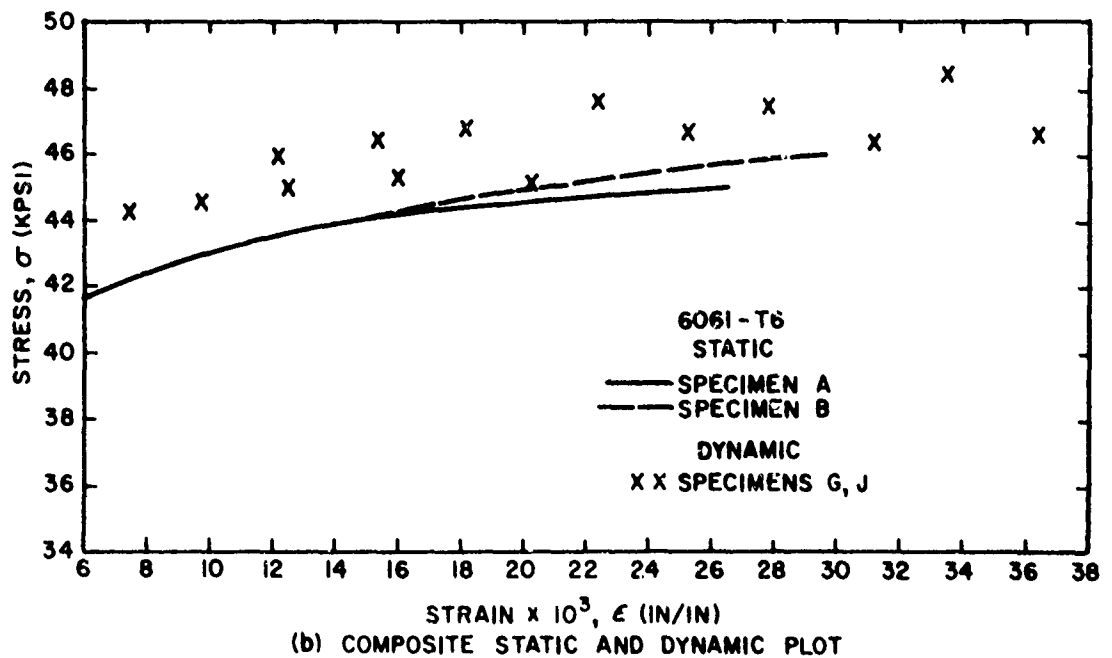
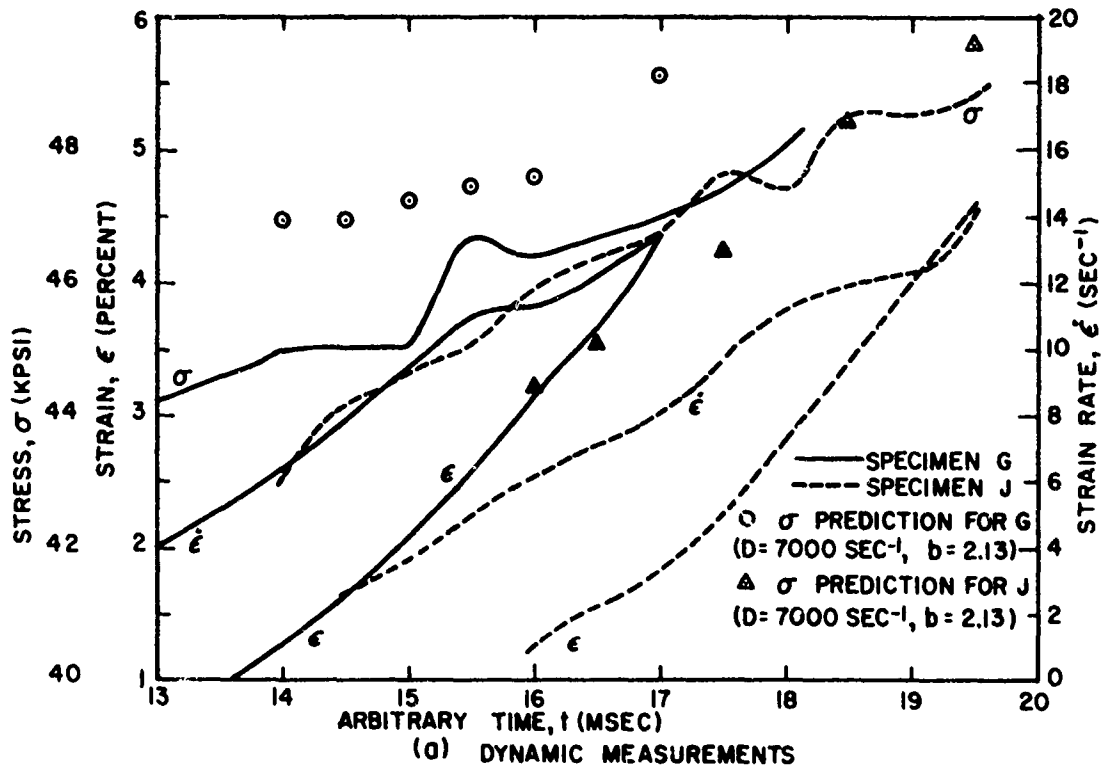


FIG. 4.6. MEASURED STATIC AND DYNAMIC STRESS-STRAIN PROPERTIES OF 6061-T6 BEAM MATERIAL

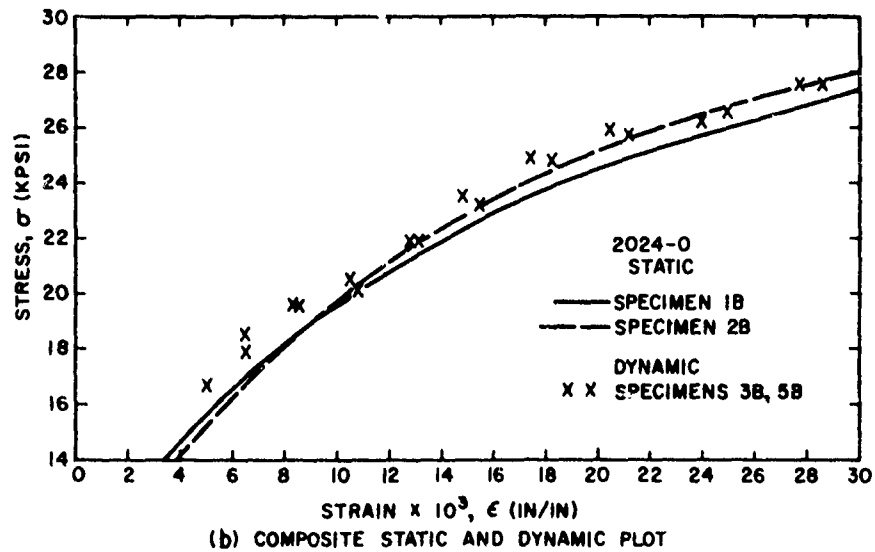
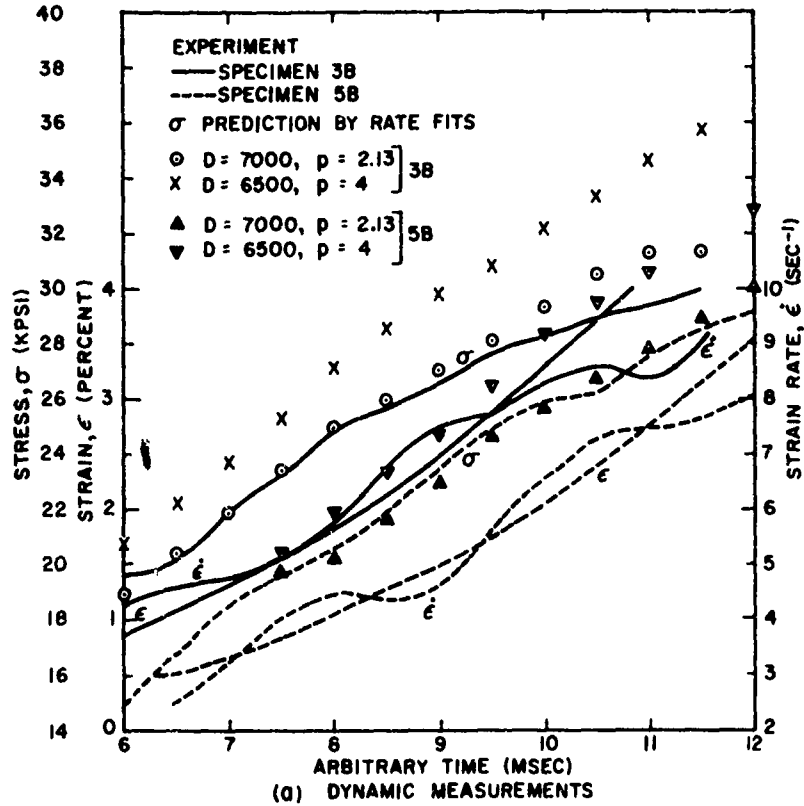


FIG. 4.7. MEASURED STATIC AND DYNAMIC STRESS-STRAIN PROPERTIES OF 2024-O BEAM MATERIAL

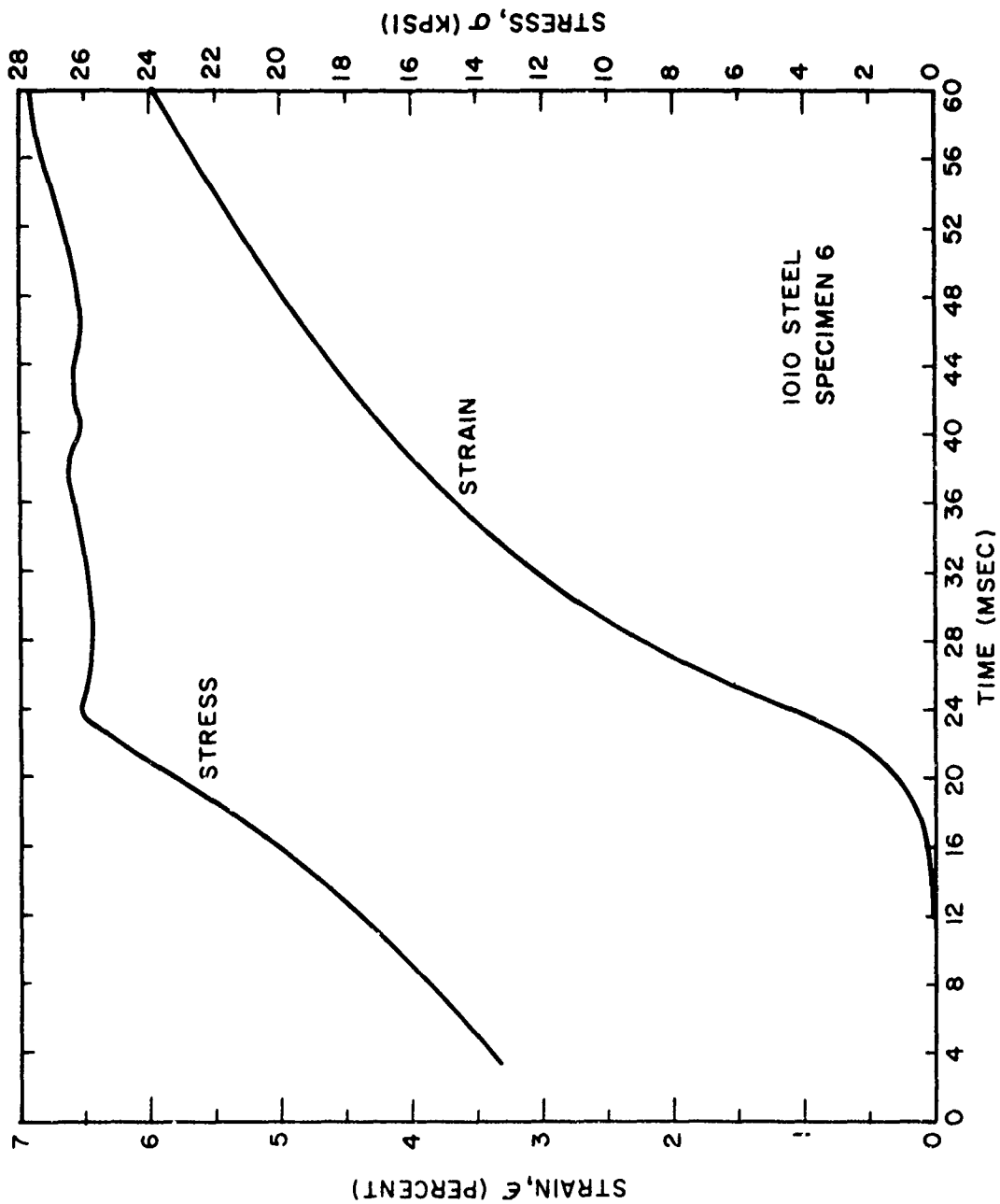


FIG. 4.8a. ILLUSTRATIVE TIME HISTORIES OF STRESS AND STRAIN  
OF 1010 STEEL SPECIMENS

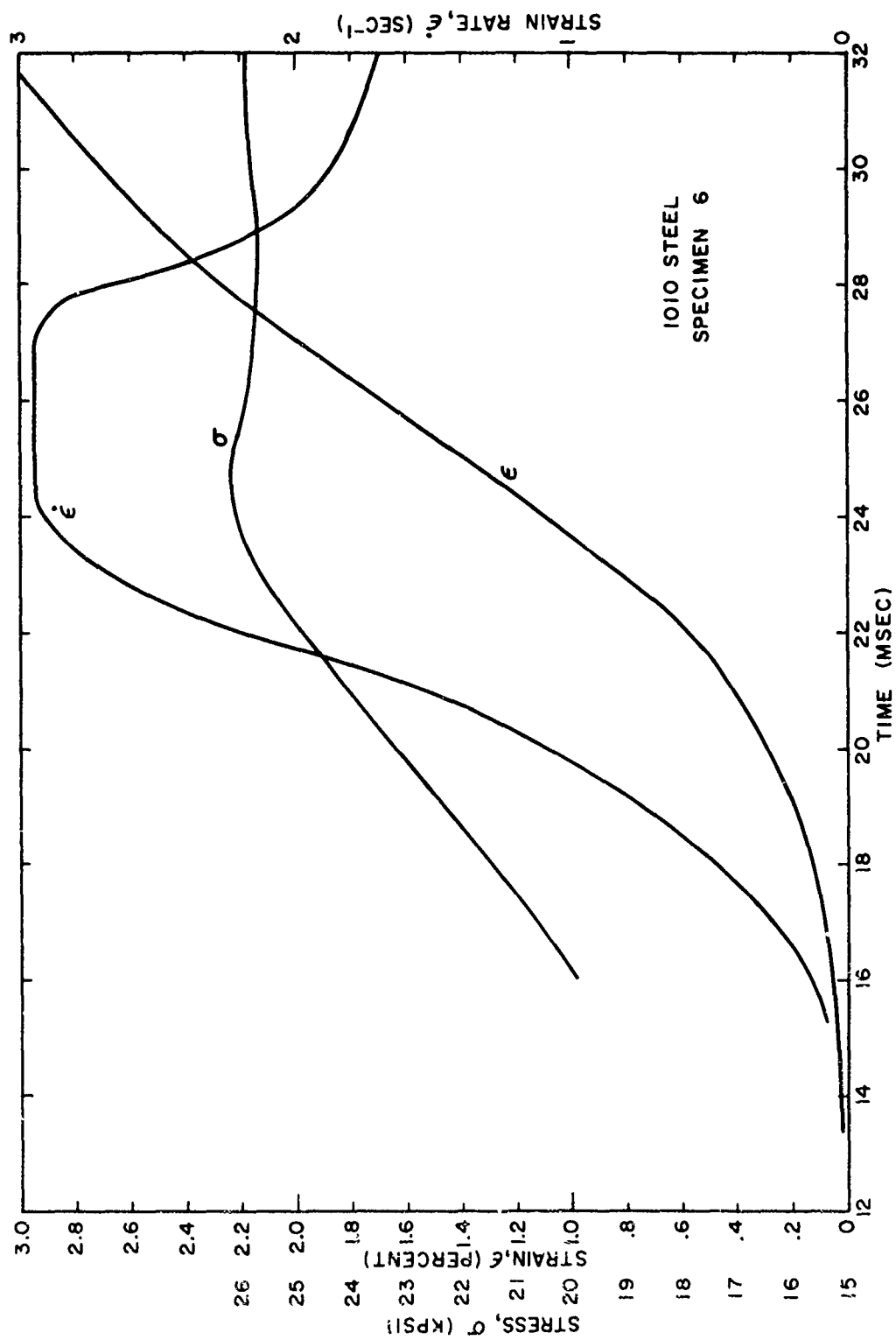


FIG. 4.8b. DYNAMIC STRESS-STRAIN CHARACTERISTICS OF 1010 STEEL SPECIMEN 6

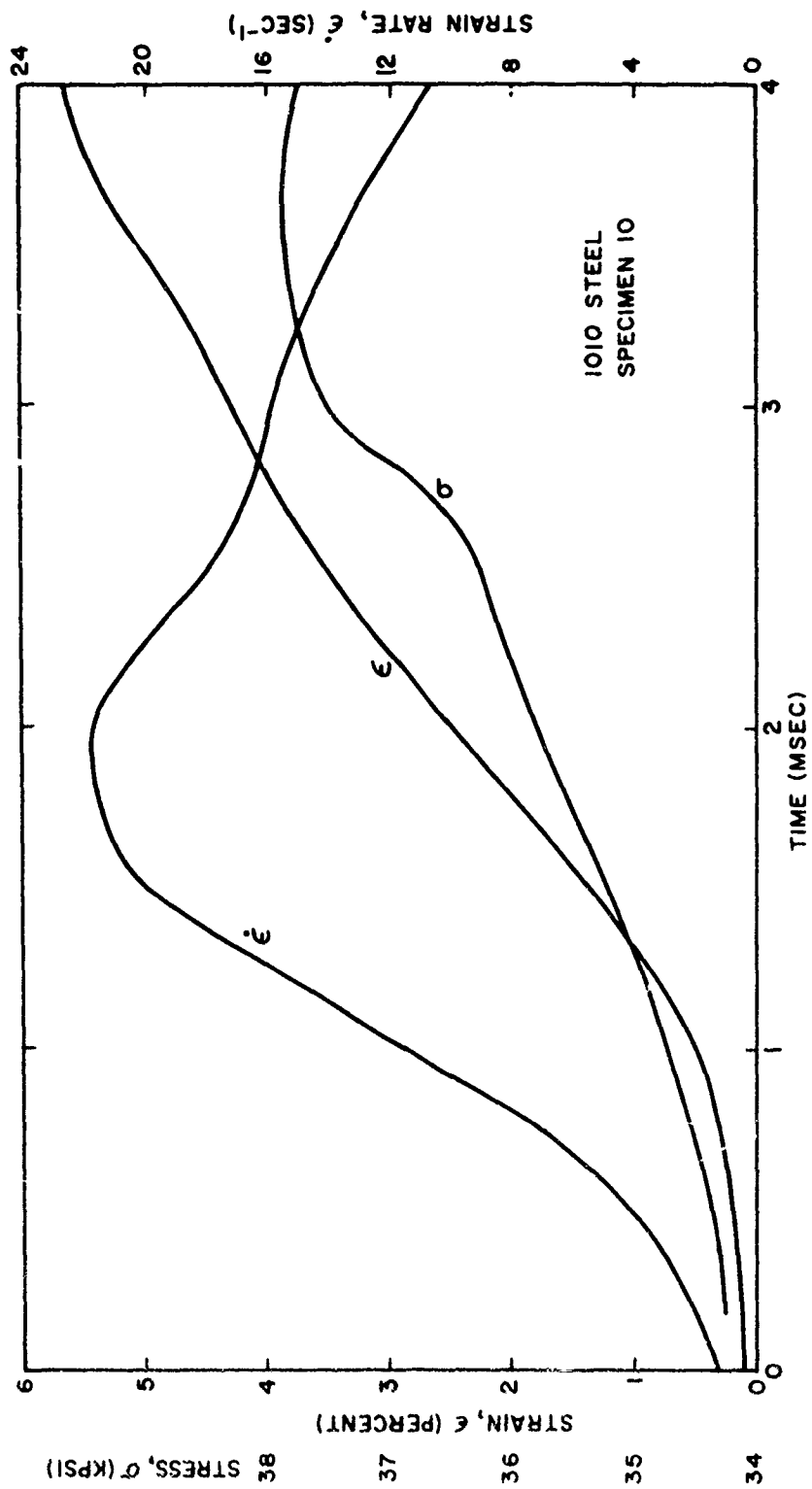


FIG. 4.8c. DYNAMIC STRESS-STRAIN CHARACTERISTICS OF 1010 STEEL SPECIMEN 10

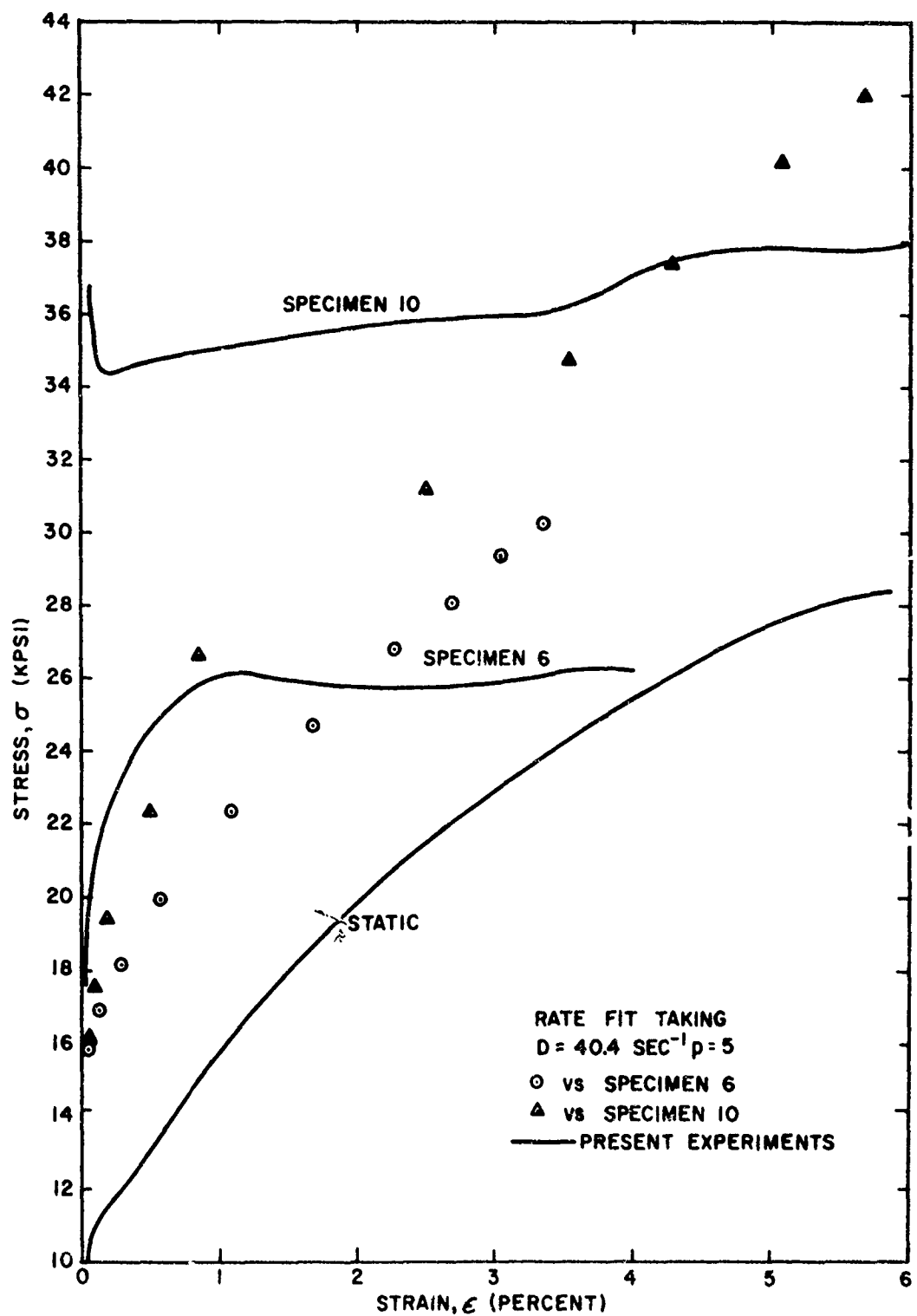


FIG. 4.9. STATIC AND DYNAMIC MEASUREMENTS OF STRESS-STRAIN PROPERTIES OF 1010 STEEL SPECIMENS

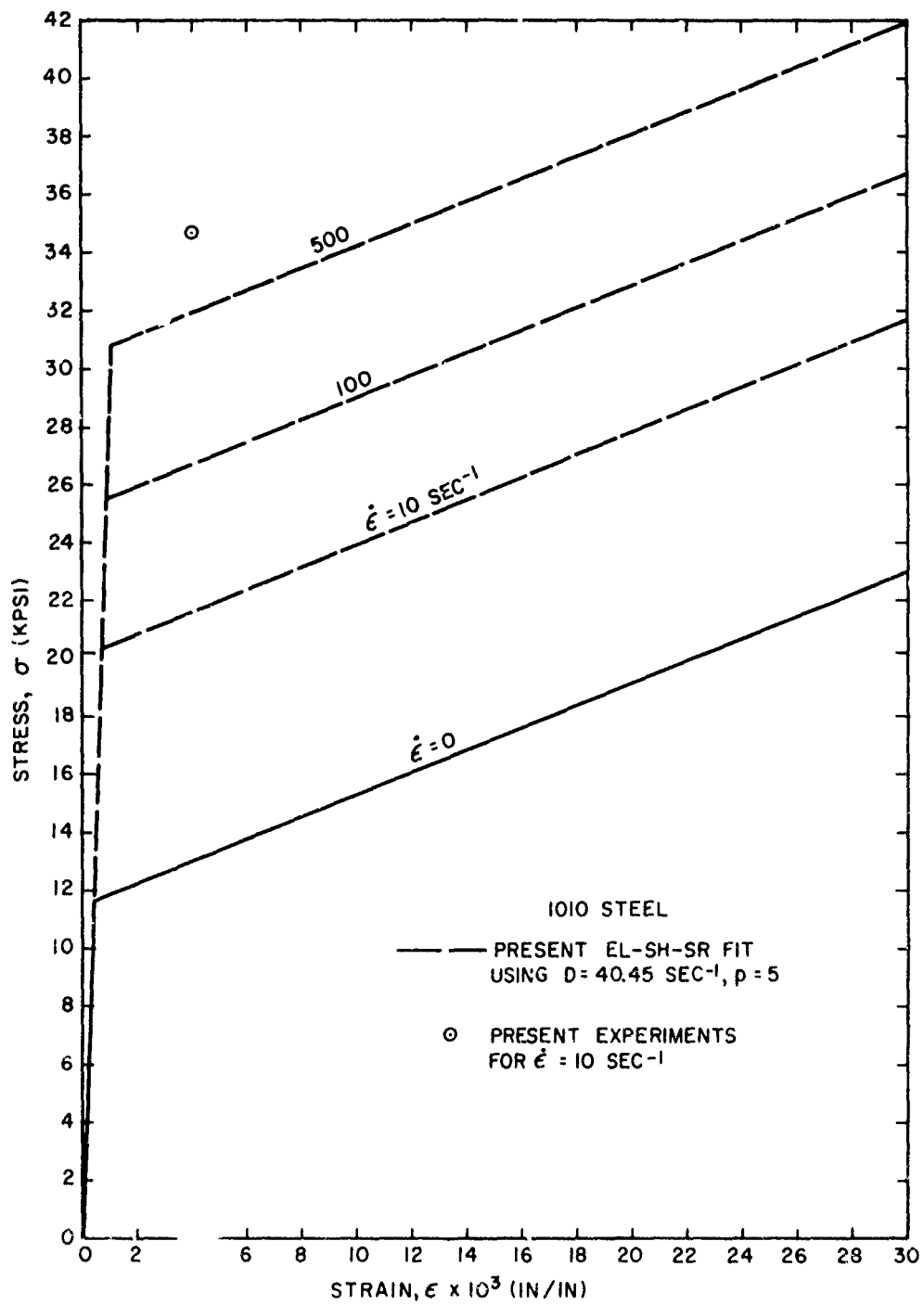


FIG. 4.10. IDEALIZED REPRESENTATION OF STATIC AND DYNAMIC STRESS-STRAIN PROPERTIES OF THE PRESENT 1010 STEEL MATERIAL

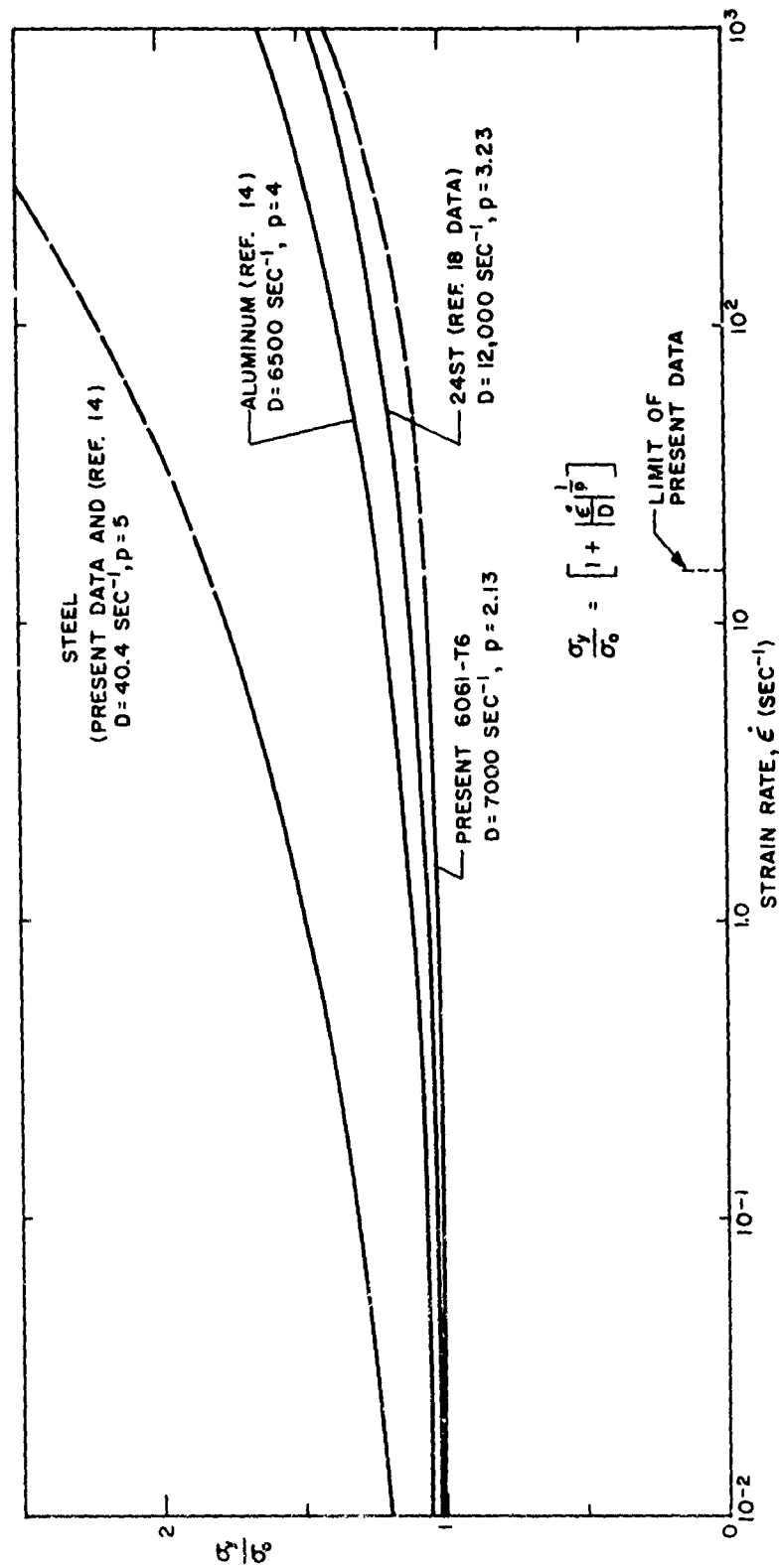


FIG. 4.11. COMPARISON OF DATA ON STRAIN-RATE EFFECT ON YIELD STRESS OF STEEL AND ALUMINUM

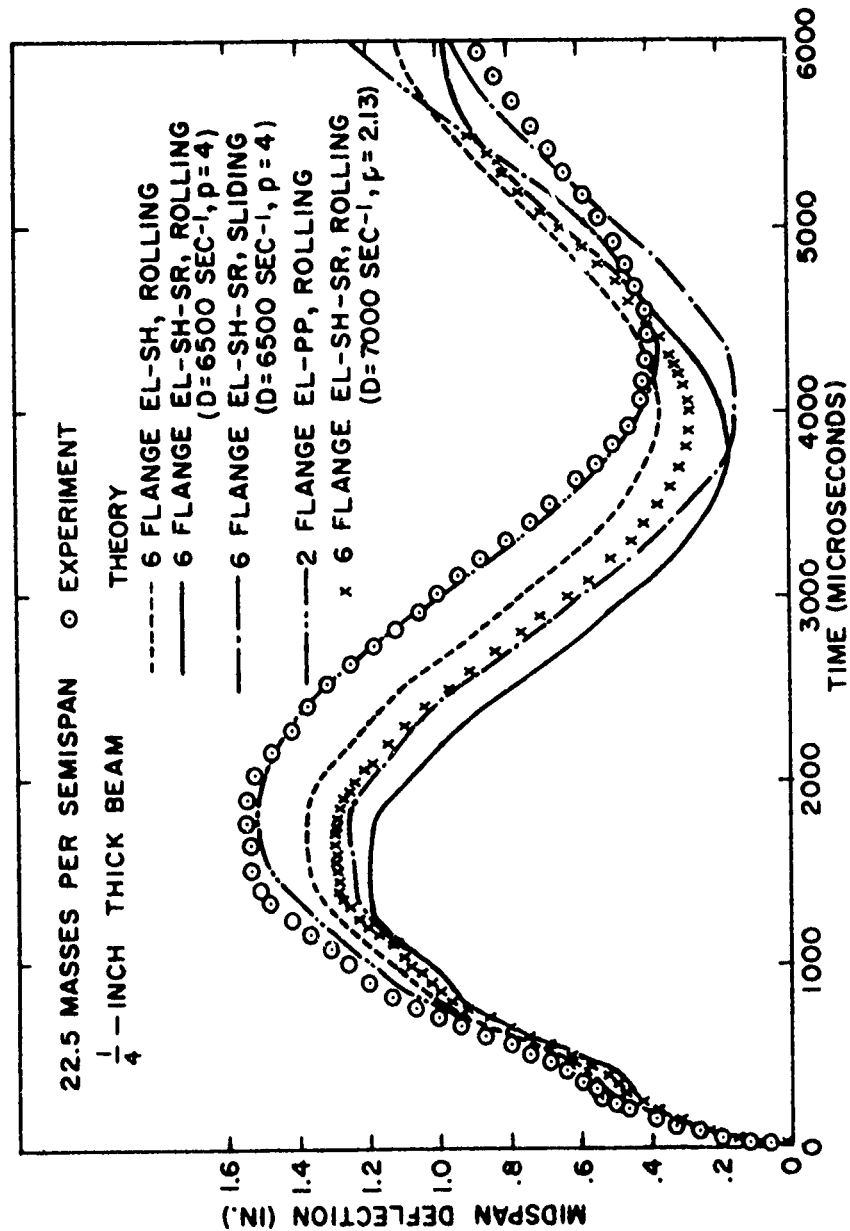


FIG. 4.12. COMPARISON OF PREDICTED AND EXPERIMENTAL MIDSPAN-DEFLECTION RESPONSES FOR EXPLOSIVELY-LOADED SIMPLY-SUPPORTED 6061-T6 BEAM 121

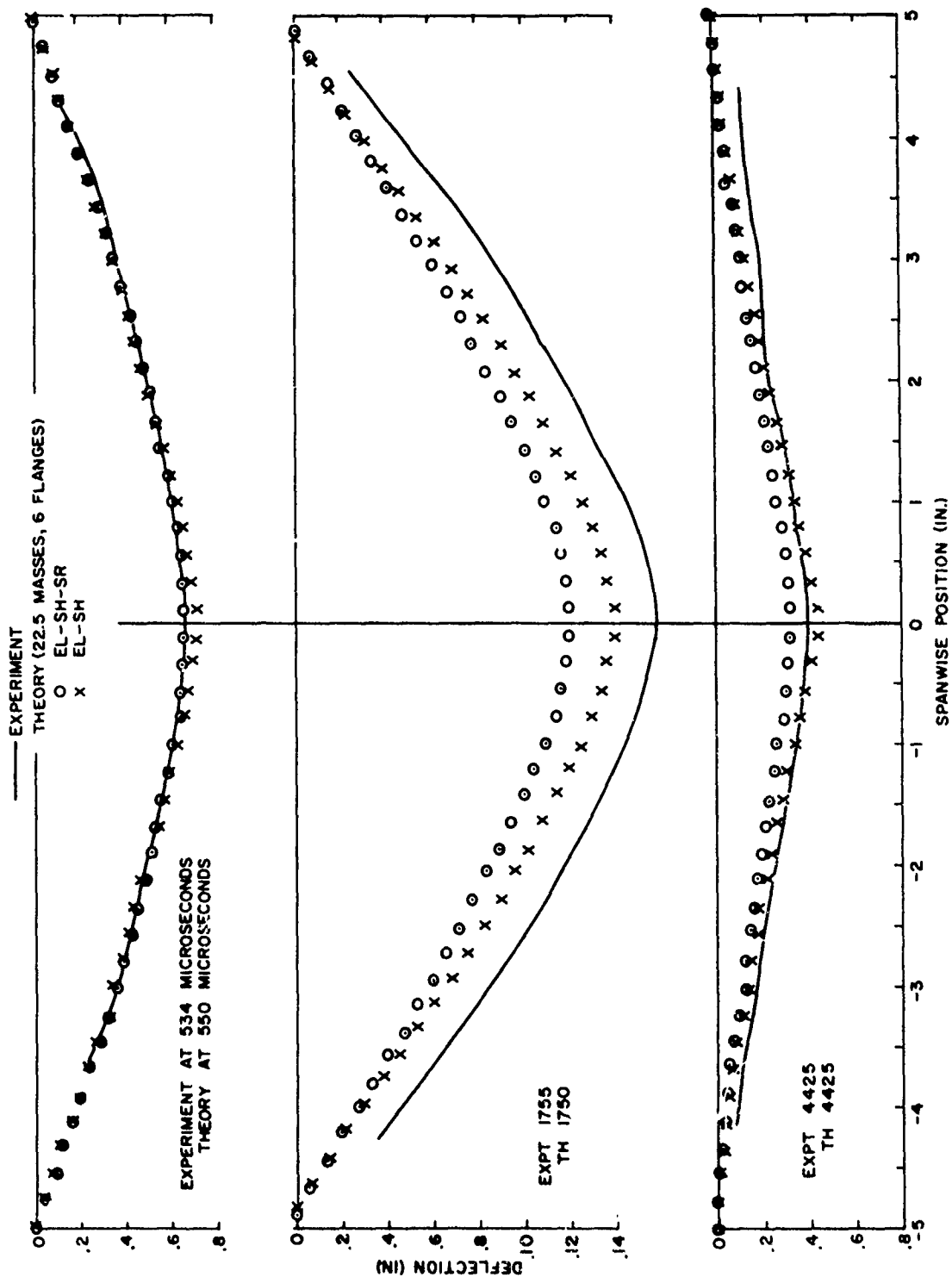


FIG. 4.13. COMPARISON OF PREDICTED AND EXPERIMENTAL DEFORMATION PROFILES FOR EXPLOSIVELY-LOADED SIMPLY-SUPPORTED 6061-T6 BEAM 121

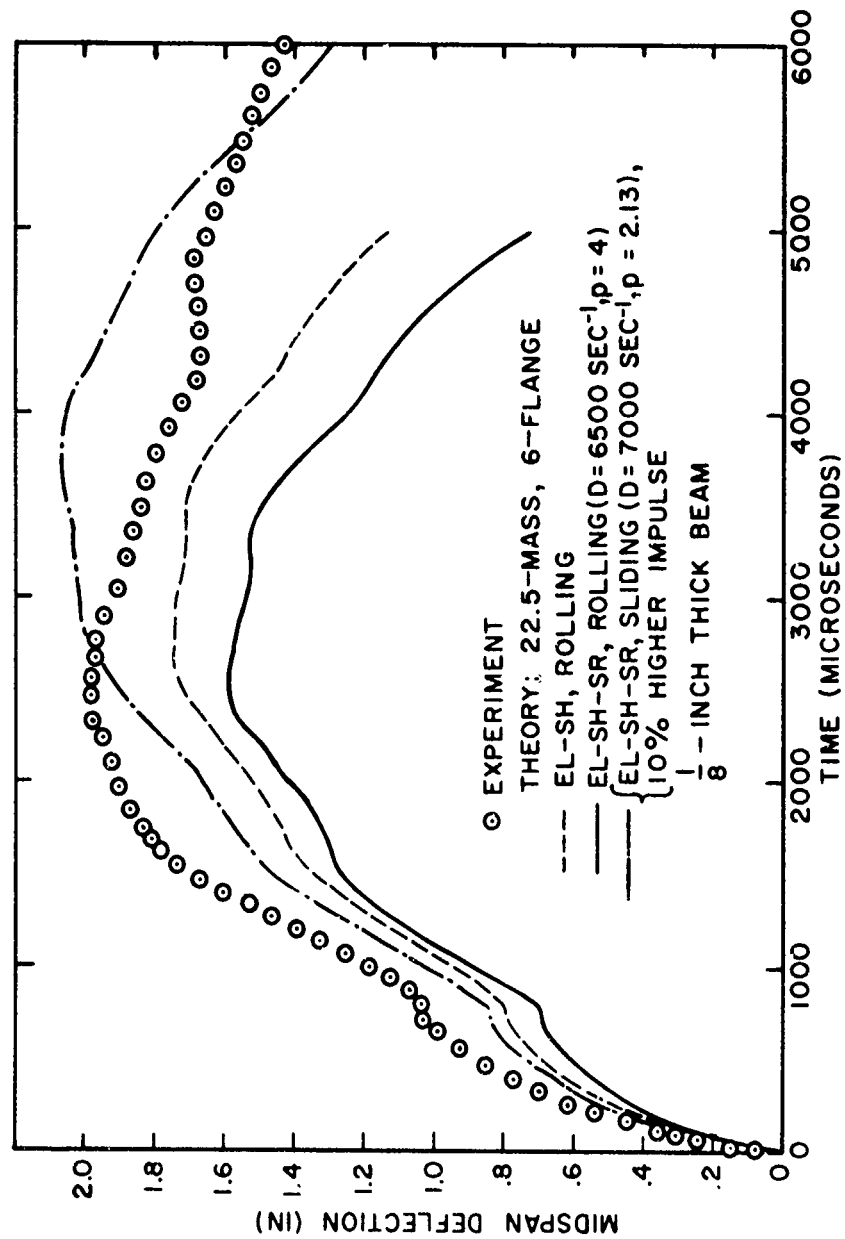


FIG. 4.14. COMPARISON OF PREDICTED AND EXPERIMENTAL MIDSPAN-DEFLECTION RESPONSES FOR EXPLOSIVELY-LOADED SIMPLY-SUPPORTED 6061-T6 BEAM 131

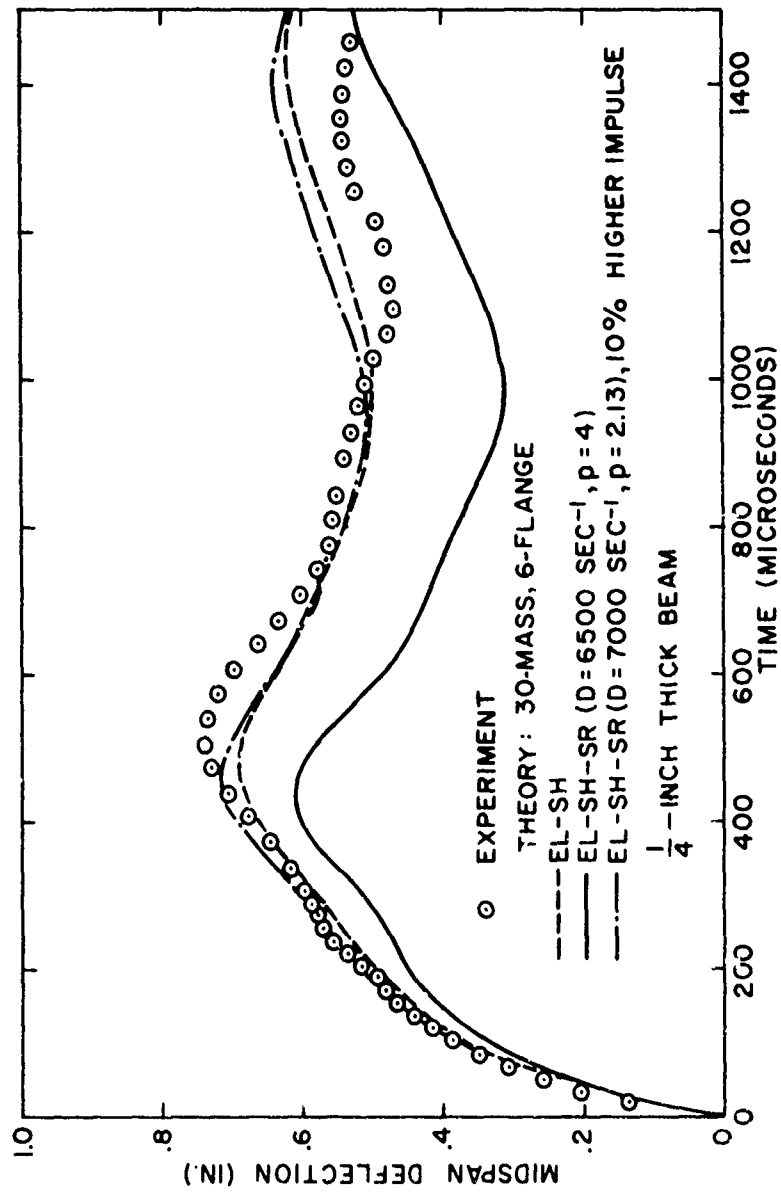


FIG. 4.15. COMPARISON OF PREDICTED AND EXPERIMENTAL MIDSPAN-DEFLECTION RESPONSES FOR EXPLOSIVELY-LOADED CLAMPED 6061-T6 BEAM 111

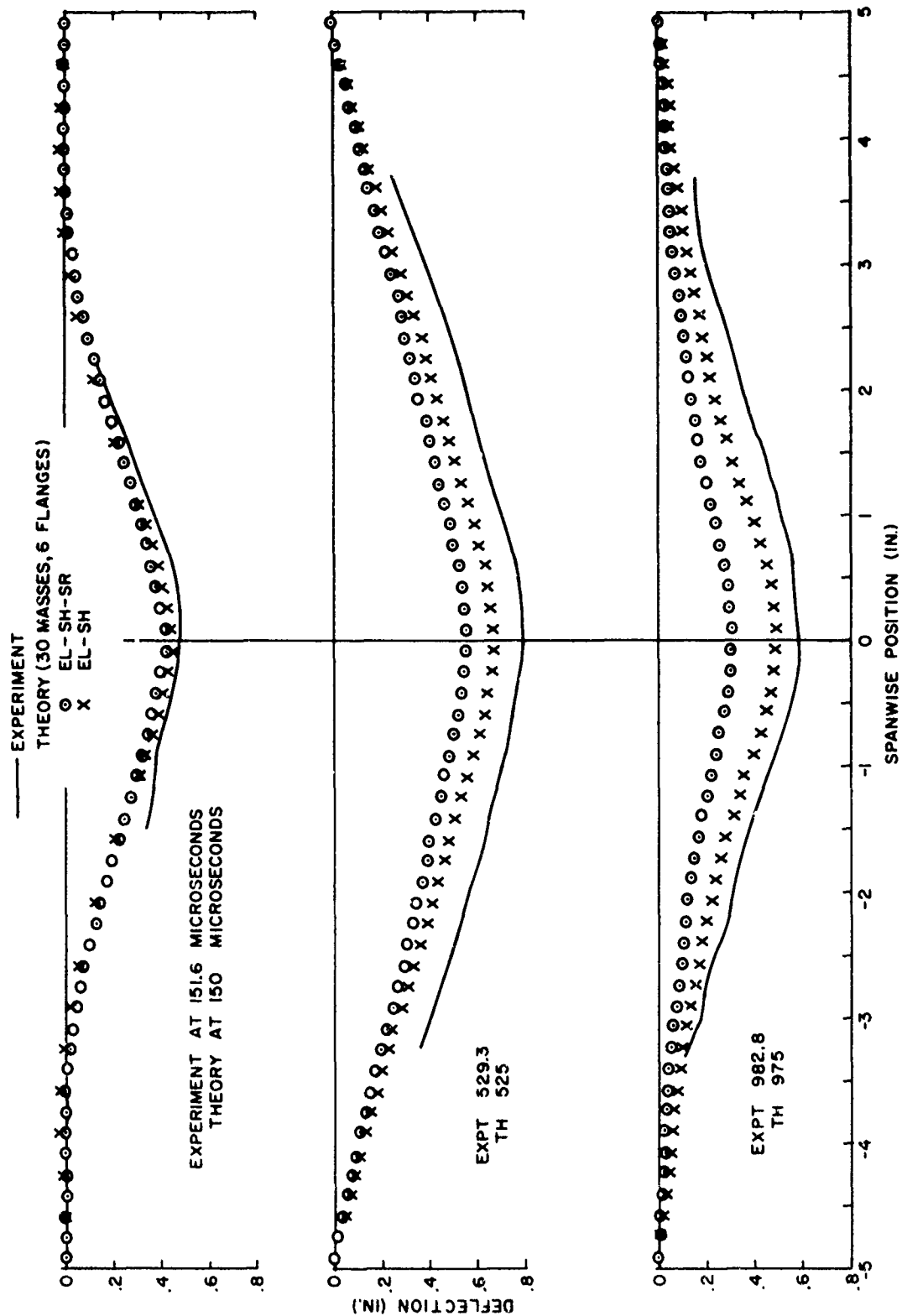


FIG. 4.16. COMPARISON OF PREDICTED AND EXPERIMENTAL DEFORMATION PROFILES FOR EXPLOSIVELY-LOADED CLAMPED 6061-T6 BEAM 112

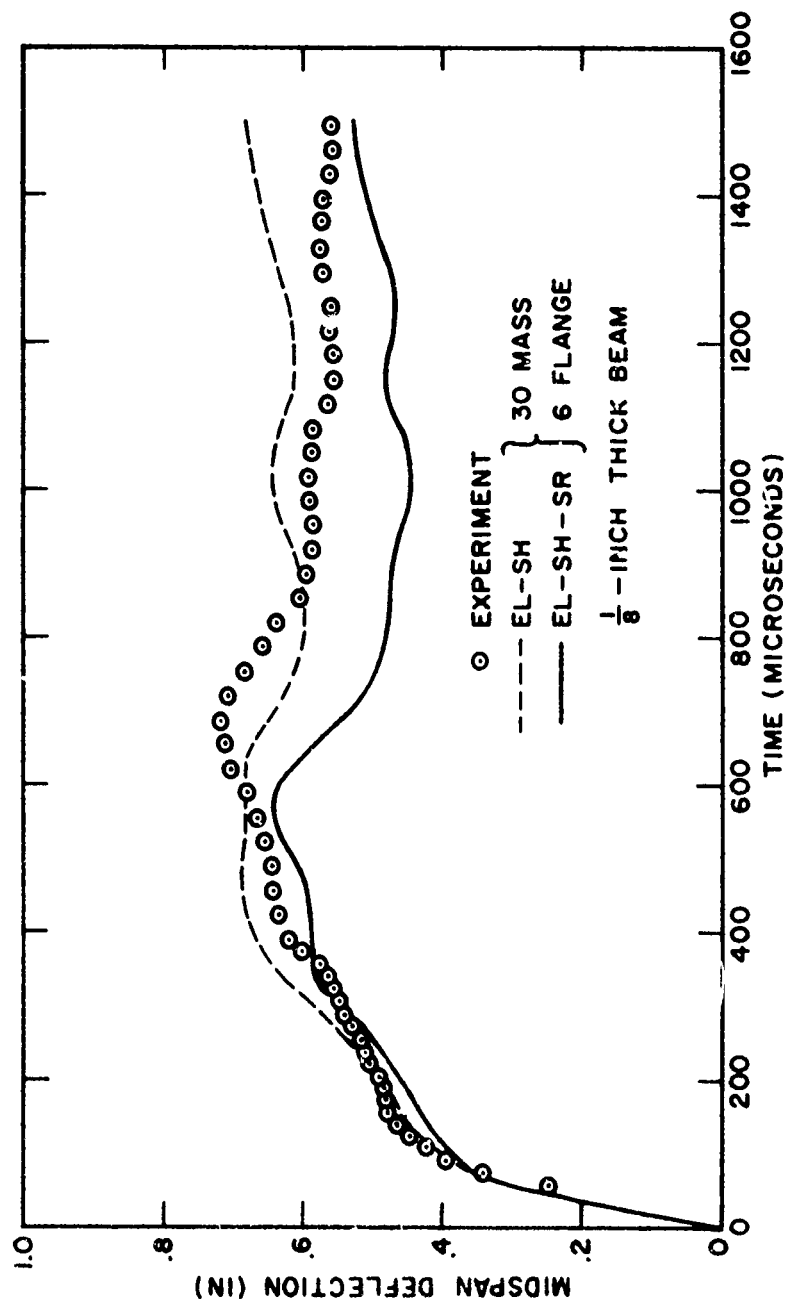


FIG. 4.17. COMPARISON OF PREDICTED AND EXPERIMENTAL MIDSPAN-DEFLECTION RESPONSES FOR EXPLOSIVELY-LOADED CLAMPED 6061-T6 BEAM 95

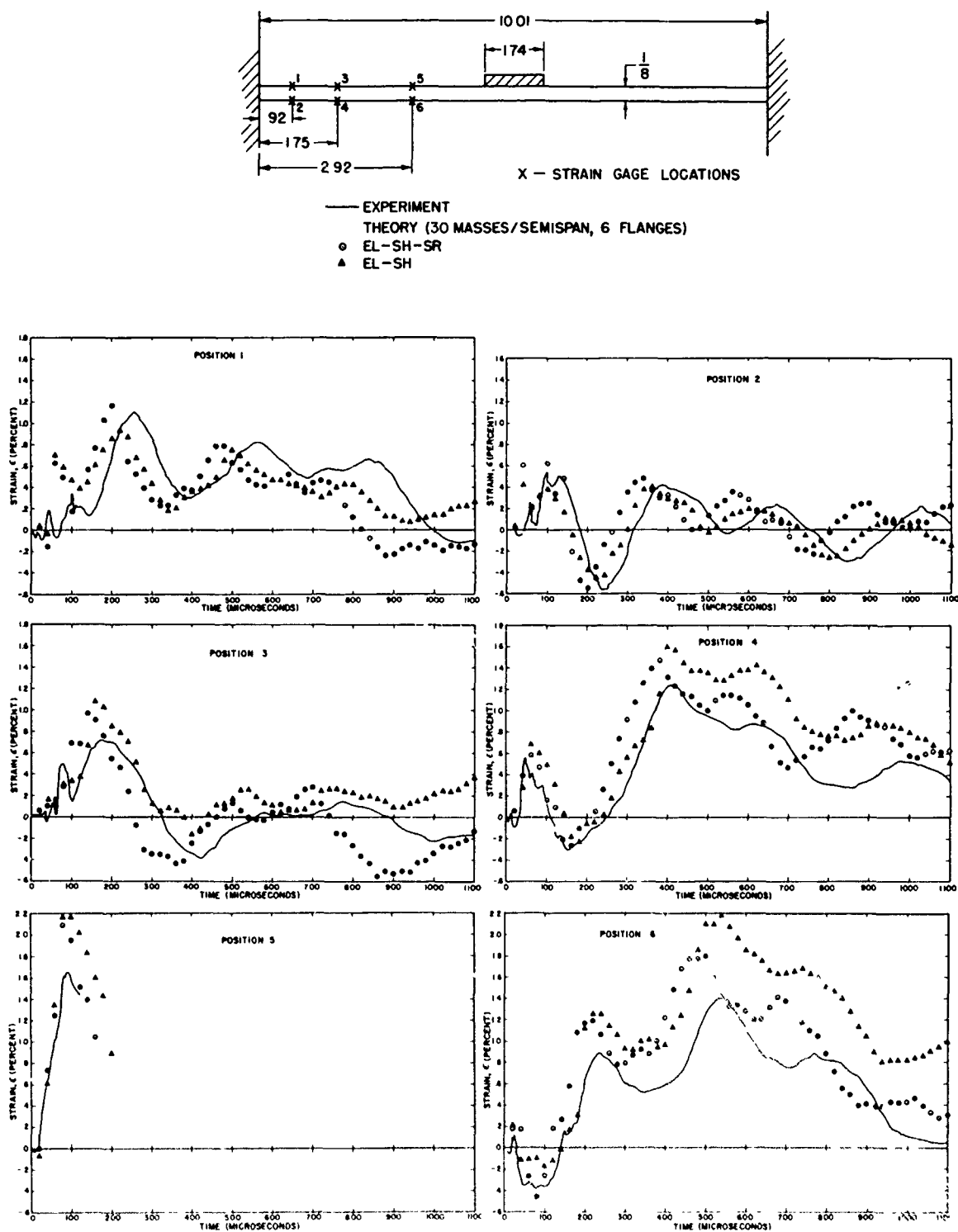


FIG. 4.18. COMPARISON OF PREDICTED AND EXPERIMENTAL STRAIN-TIME HISTORIES FOR EXPLOSIVELY-LOADED CLAMPED 6061-T6 BEAM 3

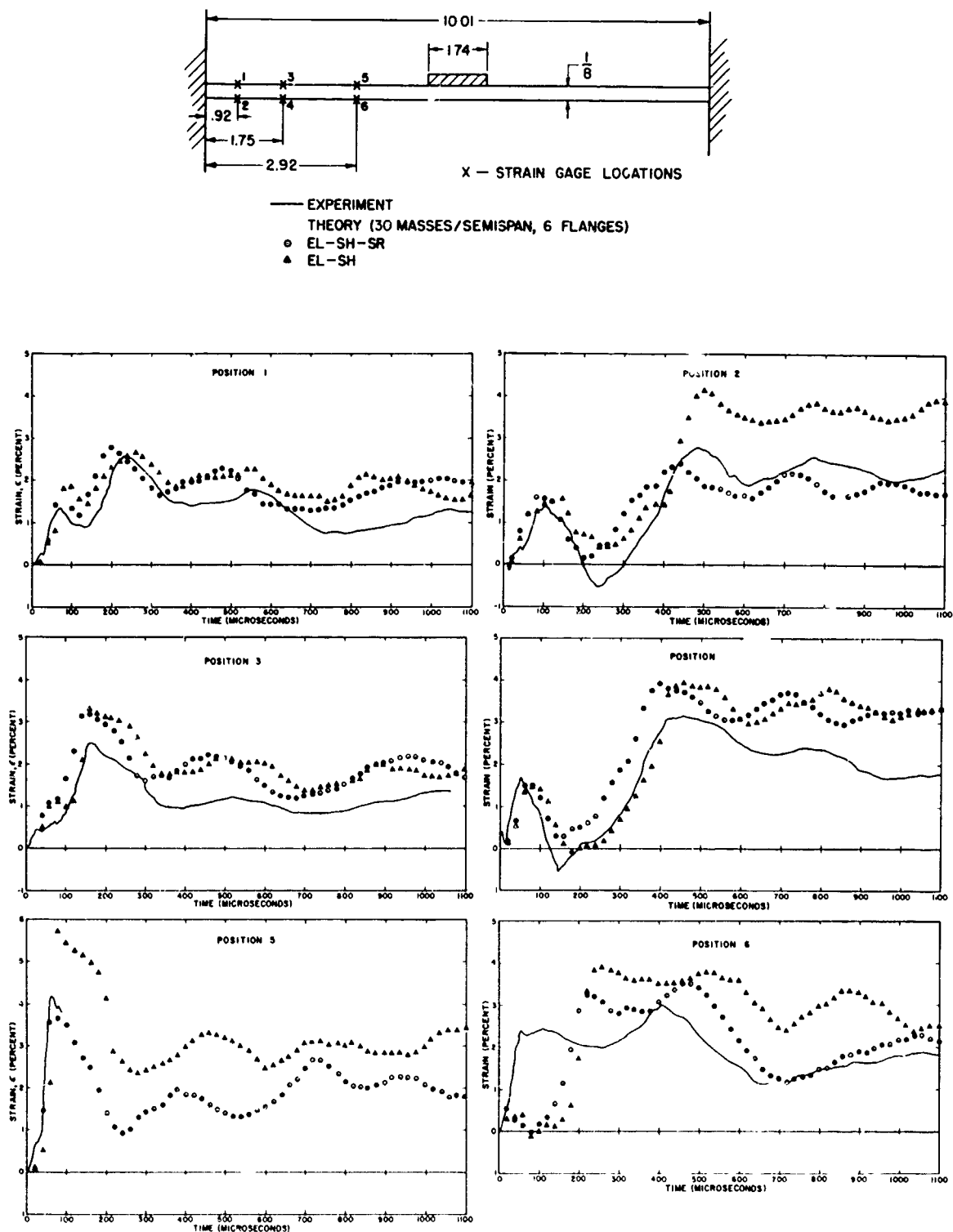


FIG. 4.19. COMPARISON OF PREDICTED AND EXPERIMENTAL STRAIN-TIME HISTORIES FOR EXPLOSIVELY-LOADED CLAMPED 6061-T6 BEAM 2

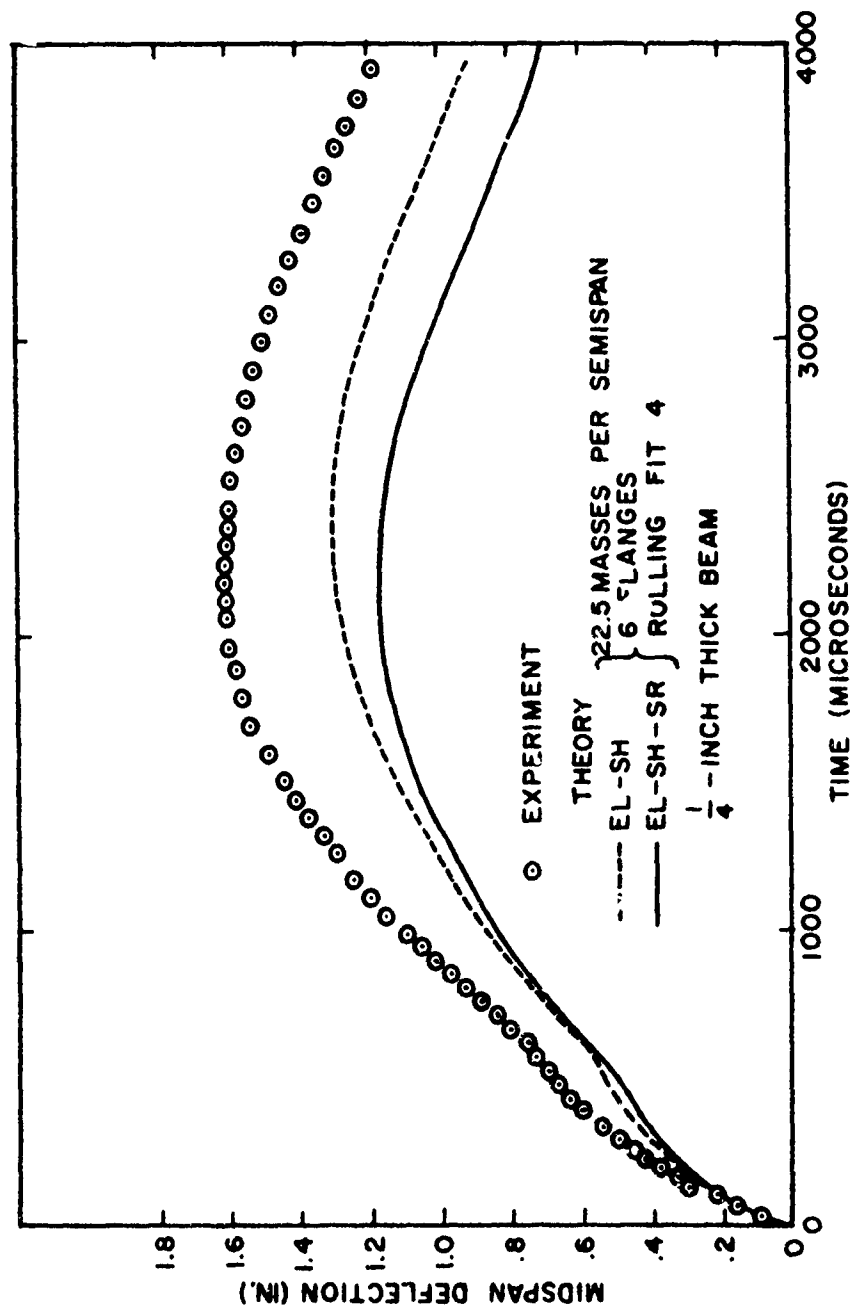


FIG. 4.20. COMPARISON OF PREDICTED AND EXPERIMENTAL MIDSPAN-DEFLECTION RESPONSES FOR EXPLOSIVELY-LOADED SIMPLY-SUPPORTED 2024-0 BEAM 119

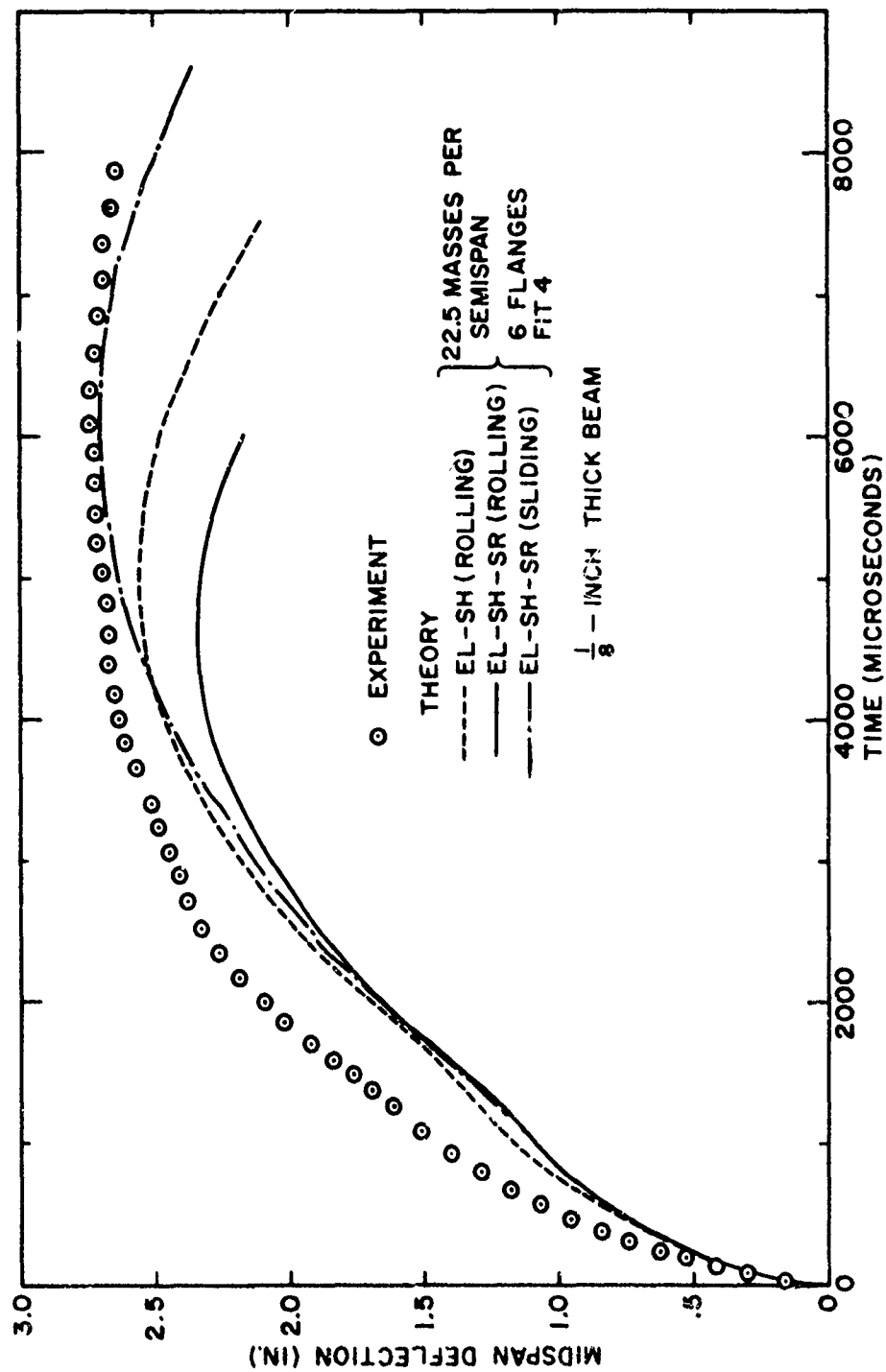


FIG. 4.21. COMPARISON OF PREDICTED AND EXPERIMENTAL MIDSPAN-DEFLECTION RESPONSES FOR EXPLOSIVELY-LOADED SIMPLY-SUPPORTED 2024-0 BEAM 134

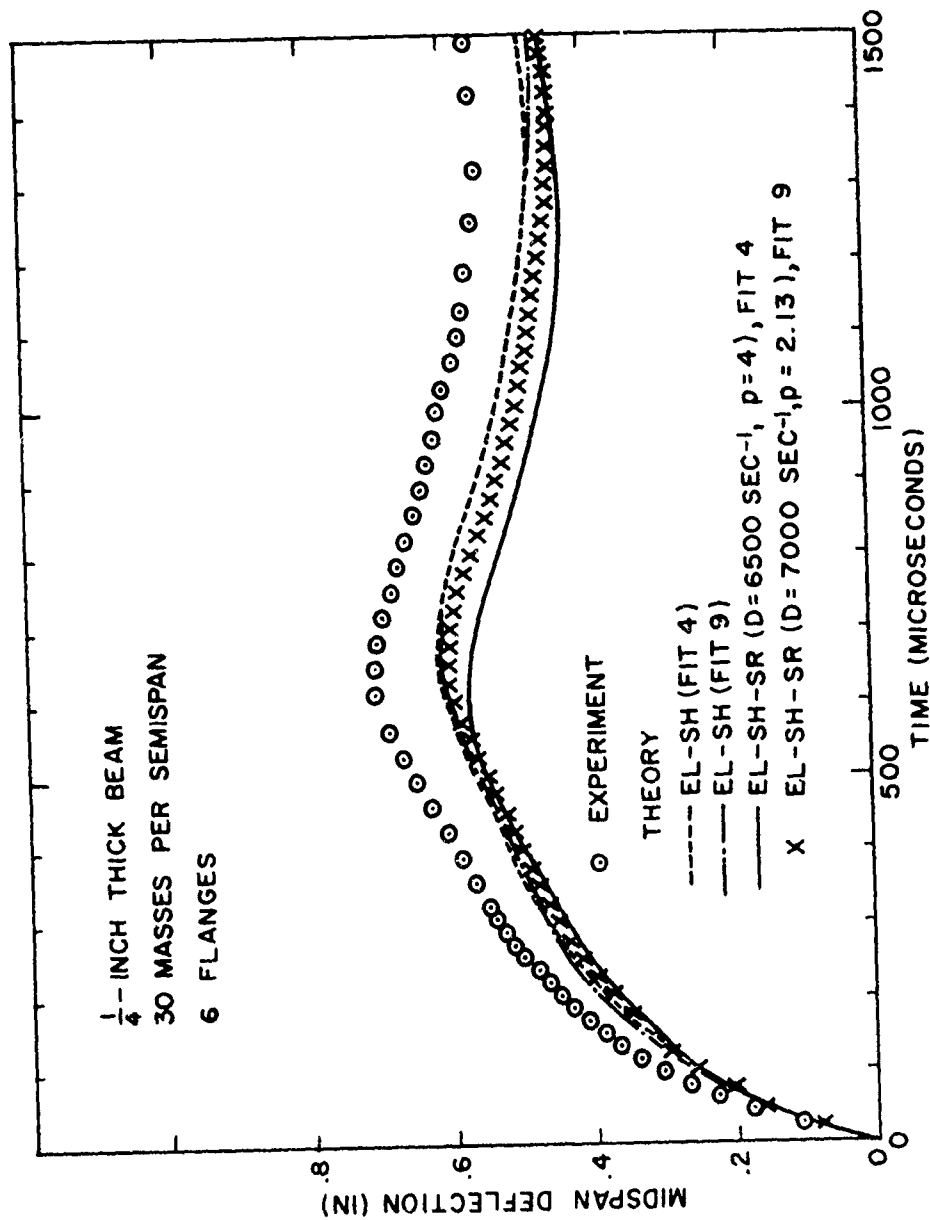


FIG. 4.22. COMPARISON OF PREDICTED AND EXPERIMENTAL MIDSPAN-DEFLECTION RESPONSES FOR EXPLOSIVELY-LOADED CLAMPED 2024-0 BEAM 88

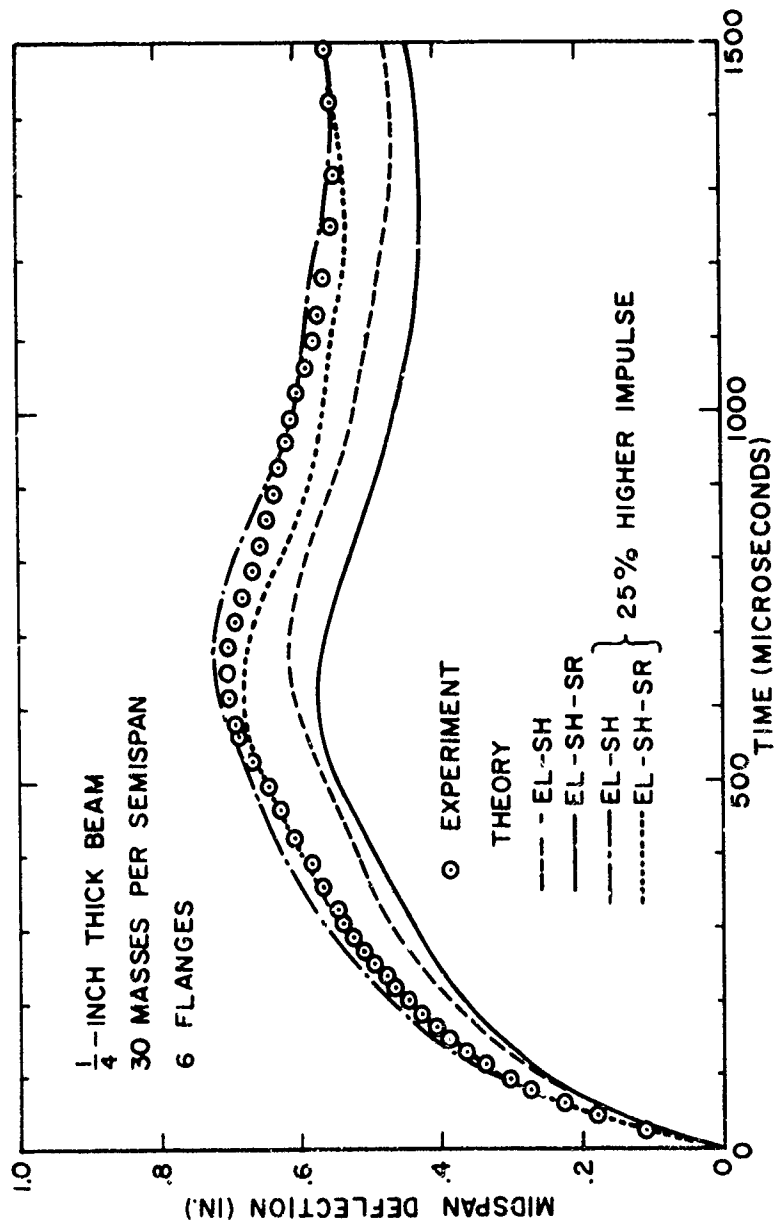


FIG. 4.23. FURTHER COMPARISONS OF CLAMPED 2024-0 BEAM 88

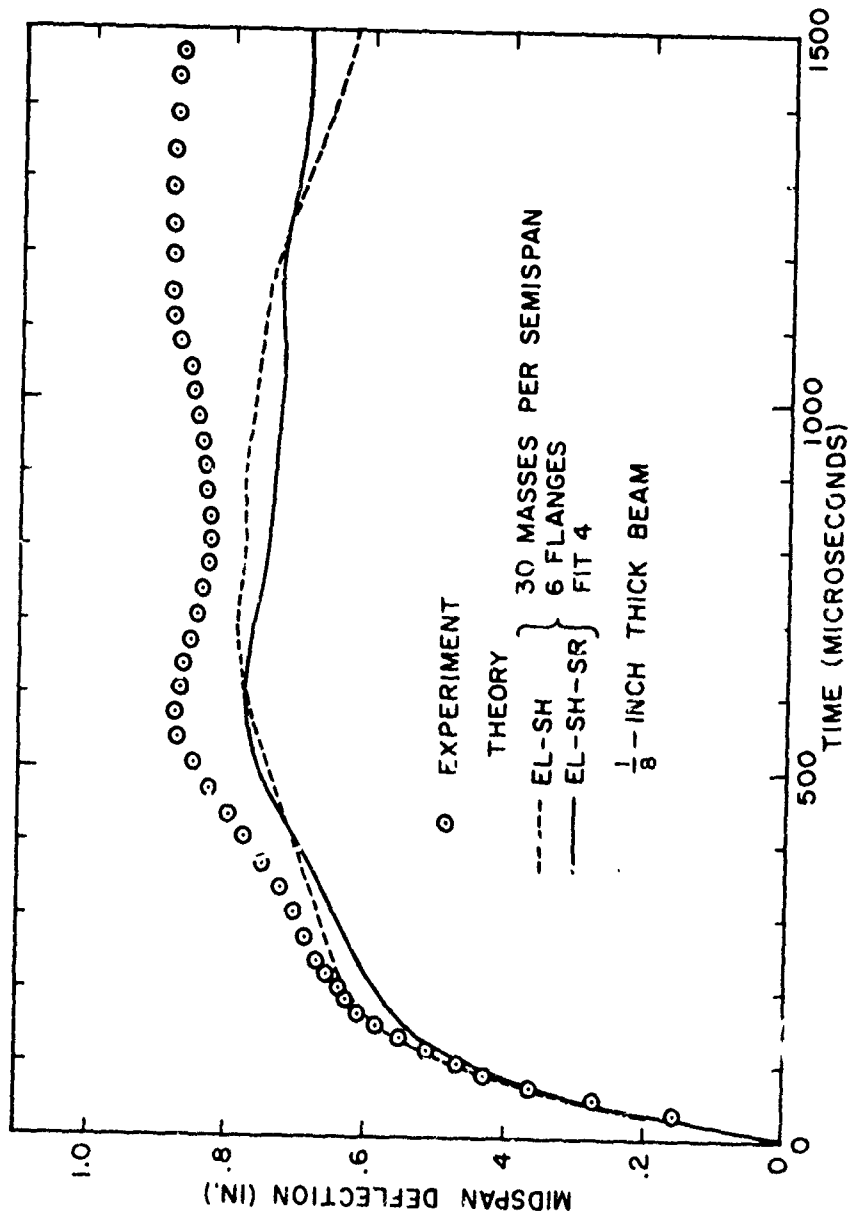


FIG. 4.24. COMPARISON OF PREDICTED AND EXPERIMENTAL MIDSPAN-DEFLECTION RESPONSES FOR EXPLOSIVELY-LOADED CLAMPED 2024-0 BEAM 100

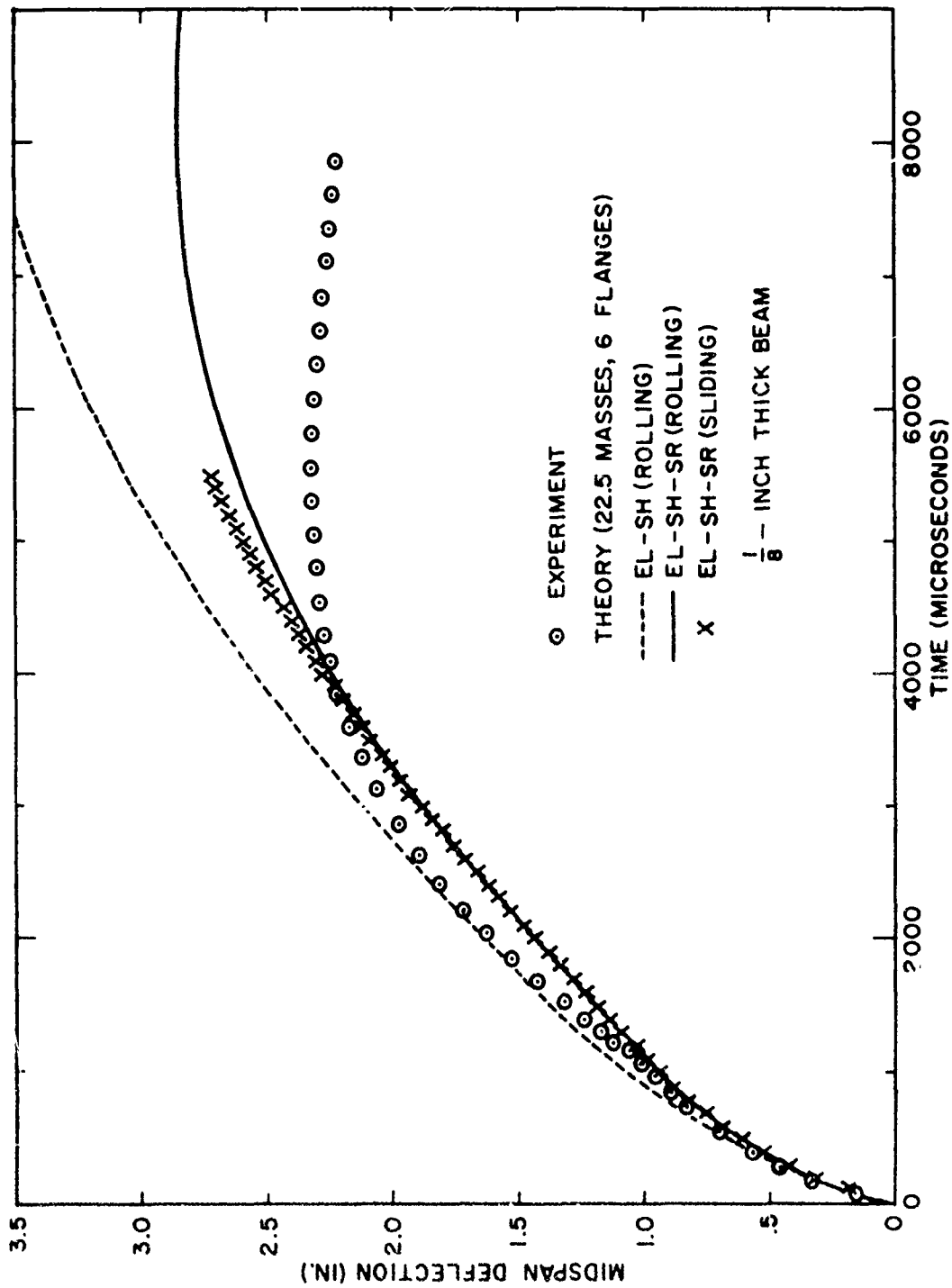


FIG. 4.25. COMPARISON OF PREDICTED AND EXPERIMENTAL MIDSPAN-DEFLECTION RESPONSES FOR EXPLOSIVELY-LOADED SIMPLY-SUPPORTED 1010 STEEL BEAM 129

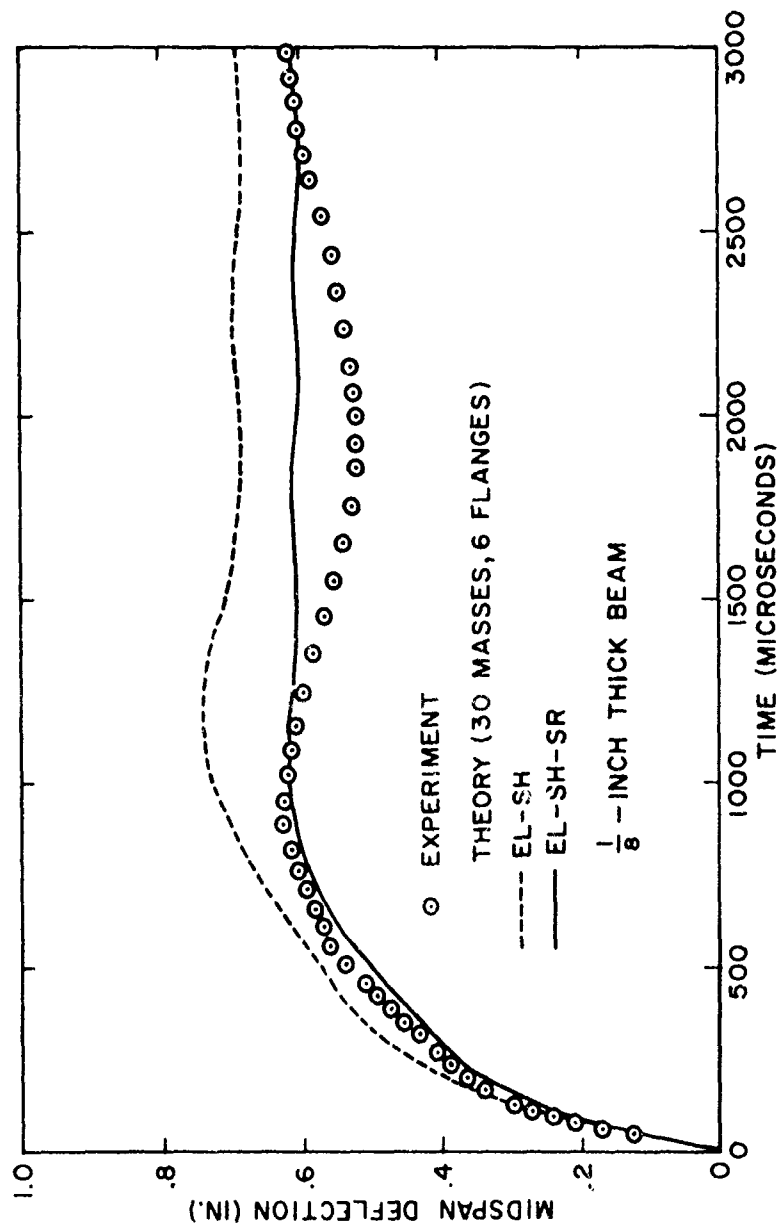


FIG. 4.26. COMPARISON OF PREDICTED AND EXPERIMENTAL MIDSPAN-DEFLECTION RESPONSES FOR EXPLOSIVELY-LOADED CLAMPED 1010 STEEL BEAM 89

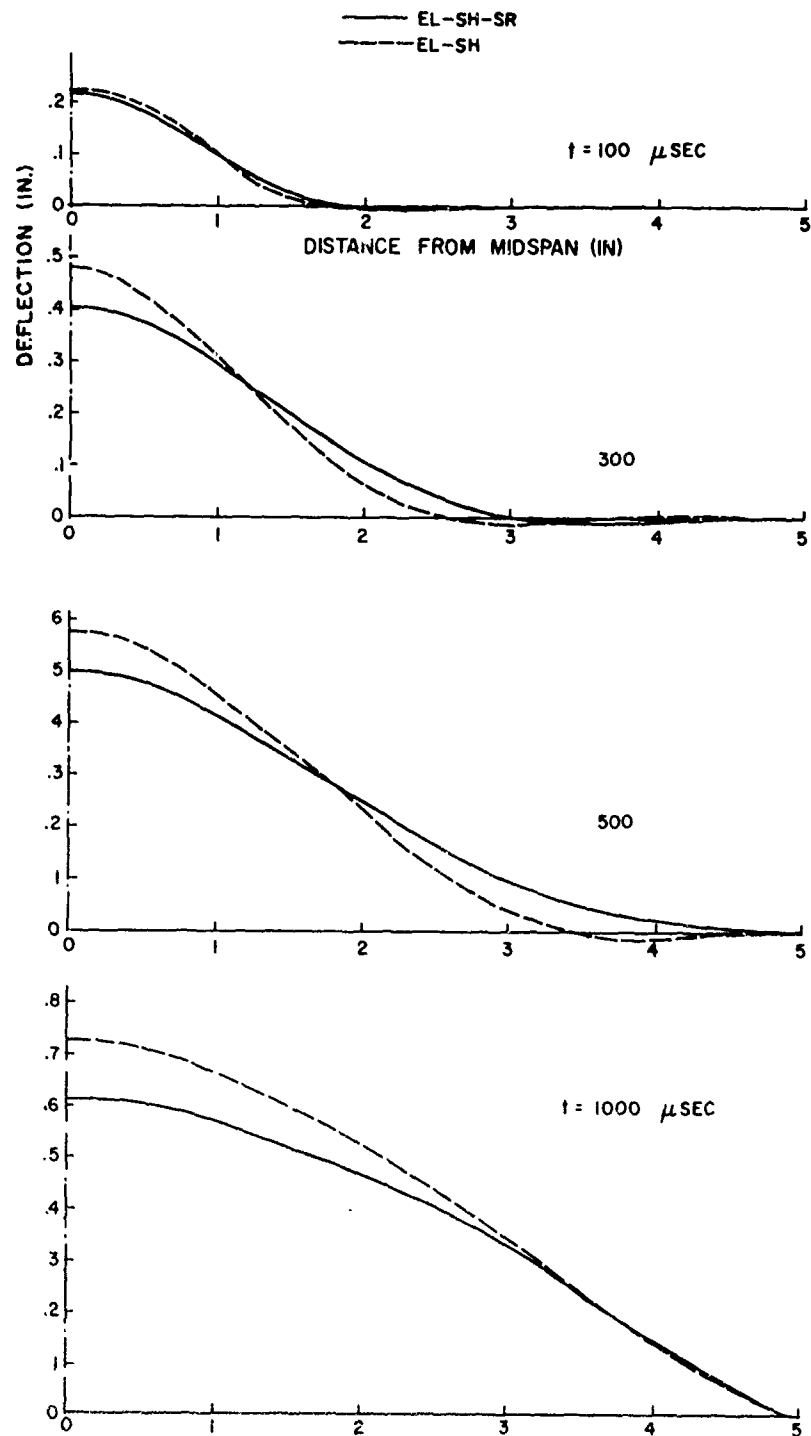


FIG. 4.27. ILLUSTRATION OF PREDICTED DEFLECTION PROFILES FOR CLAMPED 1010 STEEL BEAM 89 AT SEVERAL INSTANTS OF TIME

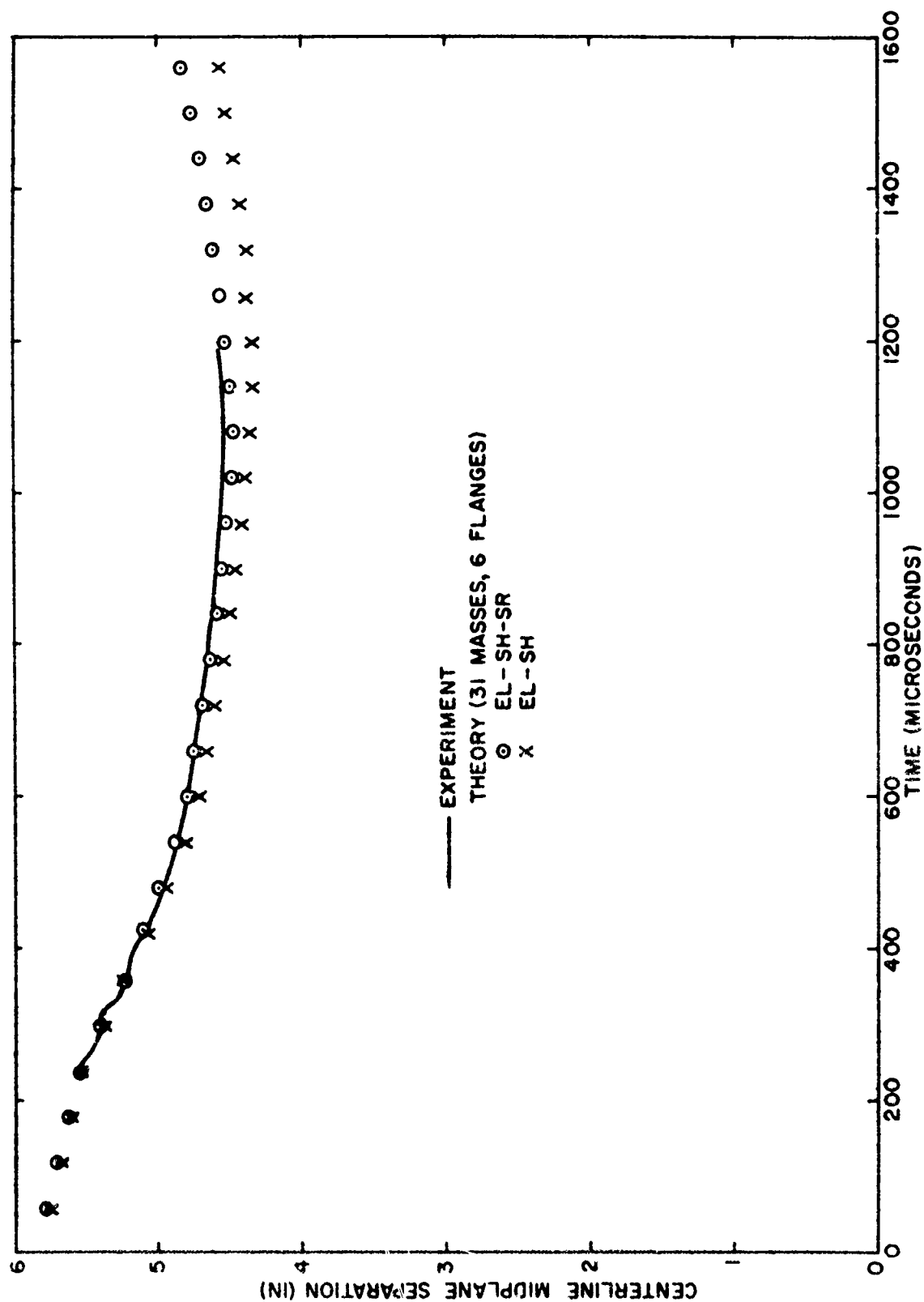


FIG. 4.28. COMPARISON OF PREDICTED AND EXPERIMENTAL CENTRAL SEPARATION RESPONSES FOR EXPLOSIVELY-LOADED 6061-T6 FREE CIRCULAR RING F4

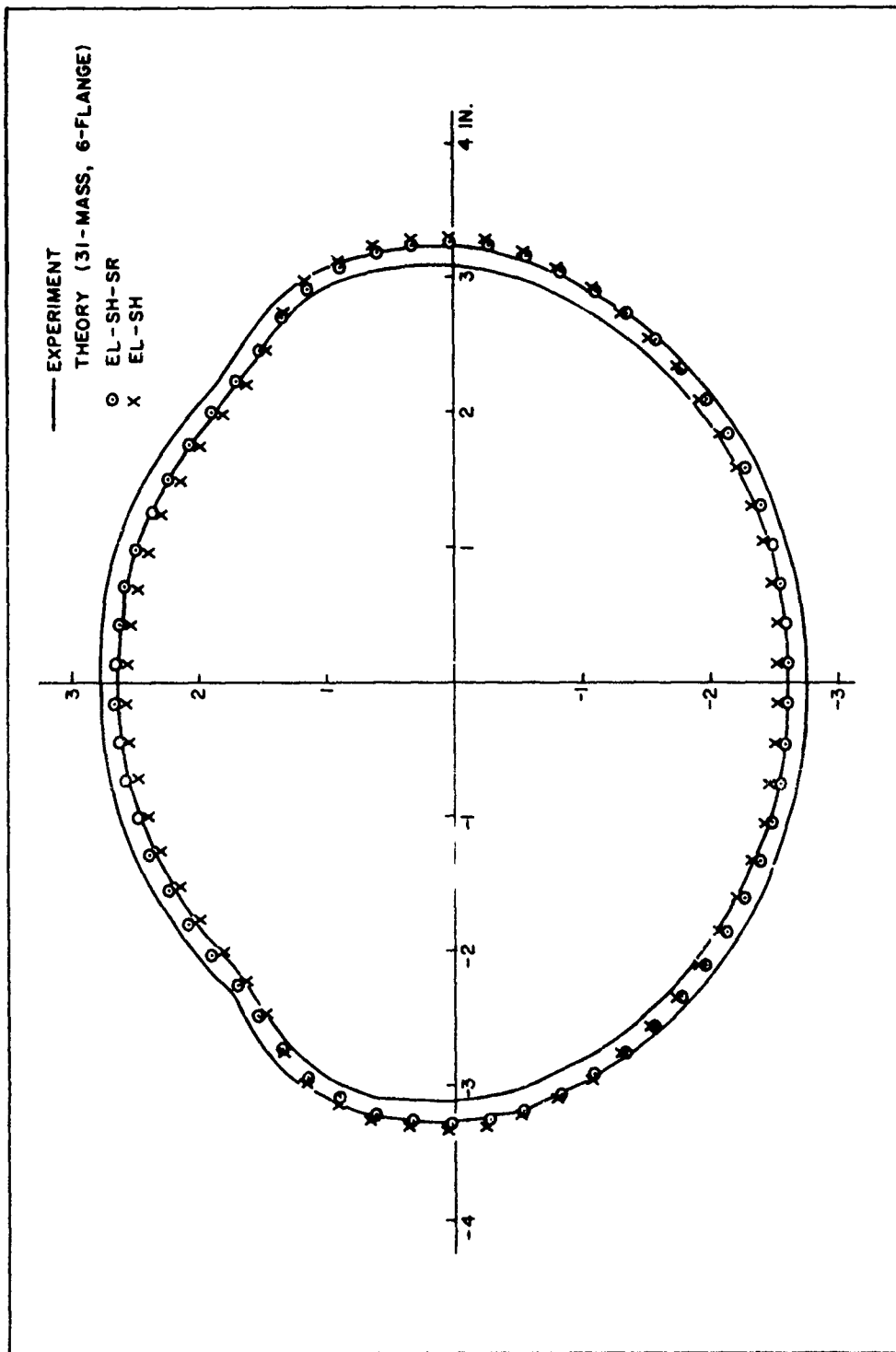


FIG. 4.29. COMPARISON OF PREDICTED AND EXPERIMENTAL PERMANENT DEFORMATION PE FOR EXPLOSIVELY-LOADED 6061-T6 FREE CIRCULAR RING F4

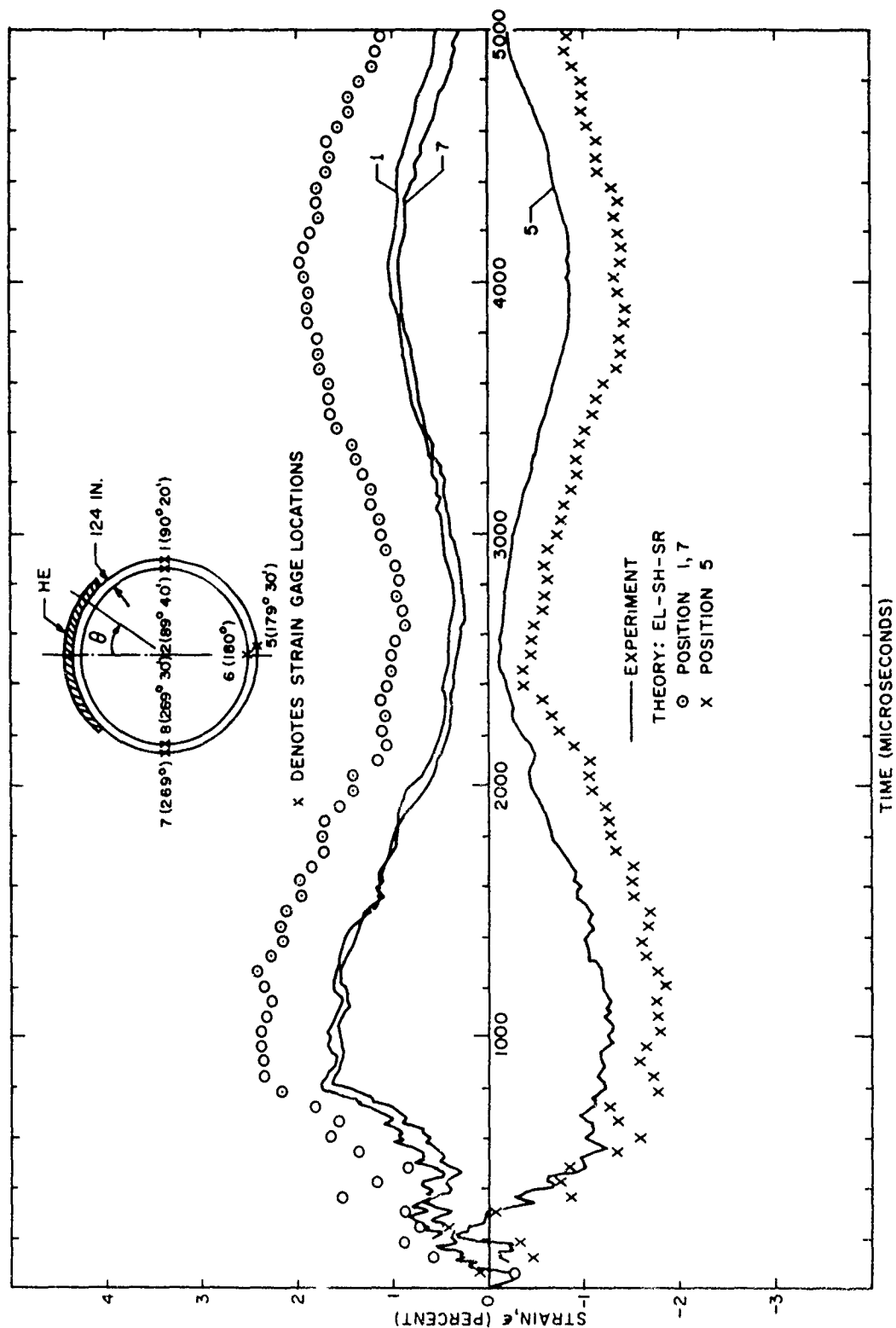


FIG. 4.30. COMPARISON OF PREDICTED AND EXPERIMENTAL STRAIN-TIME HISTORIES FOR EXPLOSIVELY-LOADED 6061-T6 FREE CIRCULAR RING F4

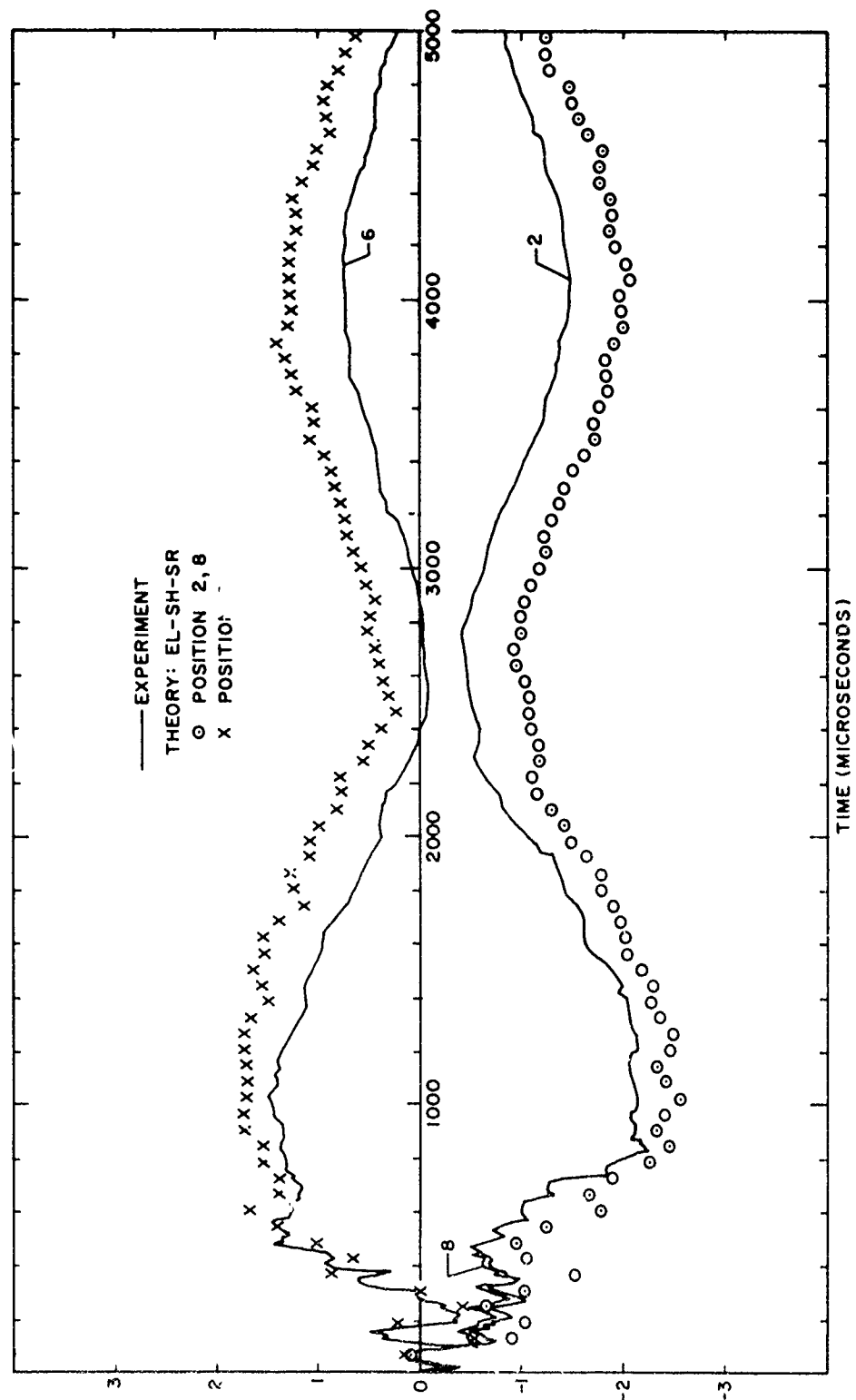
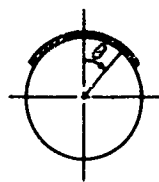


FIG. 4.30. CONCLUDED



THEORY: EL-SH-SR

— OUTSIDE

- - - INSIDE

□ EXPERIMENT

////// REGION COVERED BY EXPLOSIVE

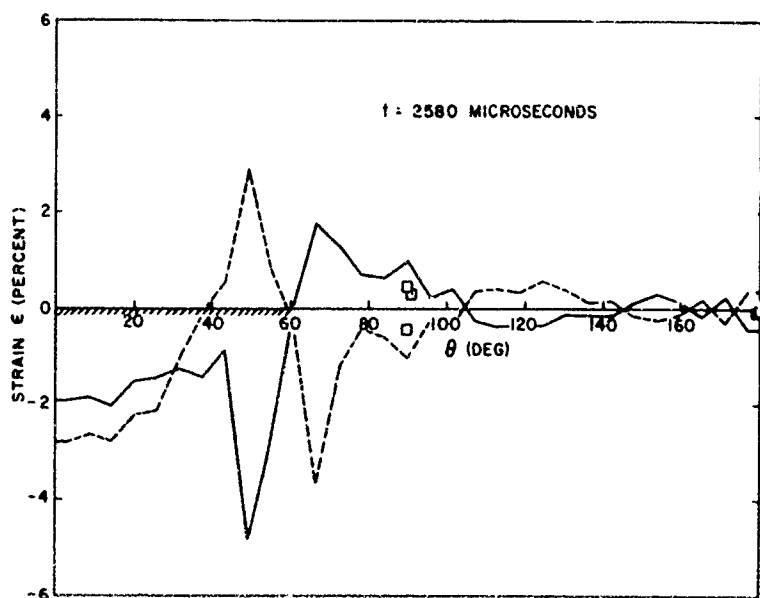
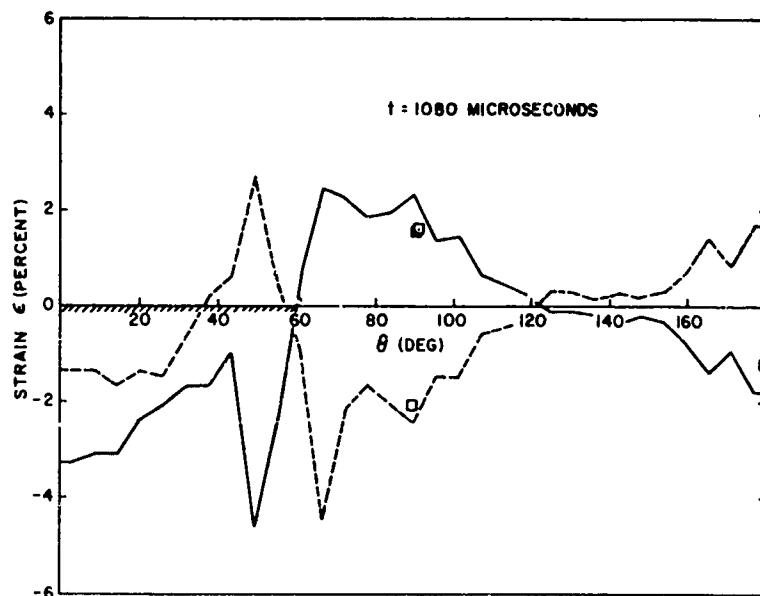


FIG. 4.31. STRAIN PROFILES FOR EXPLOSIVELY-LOADED 6061-T6 FREE CIRCULAR RING F4

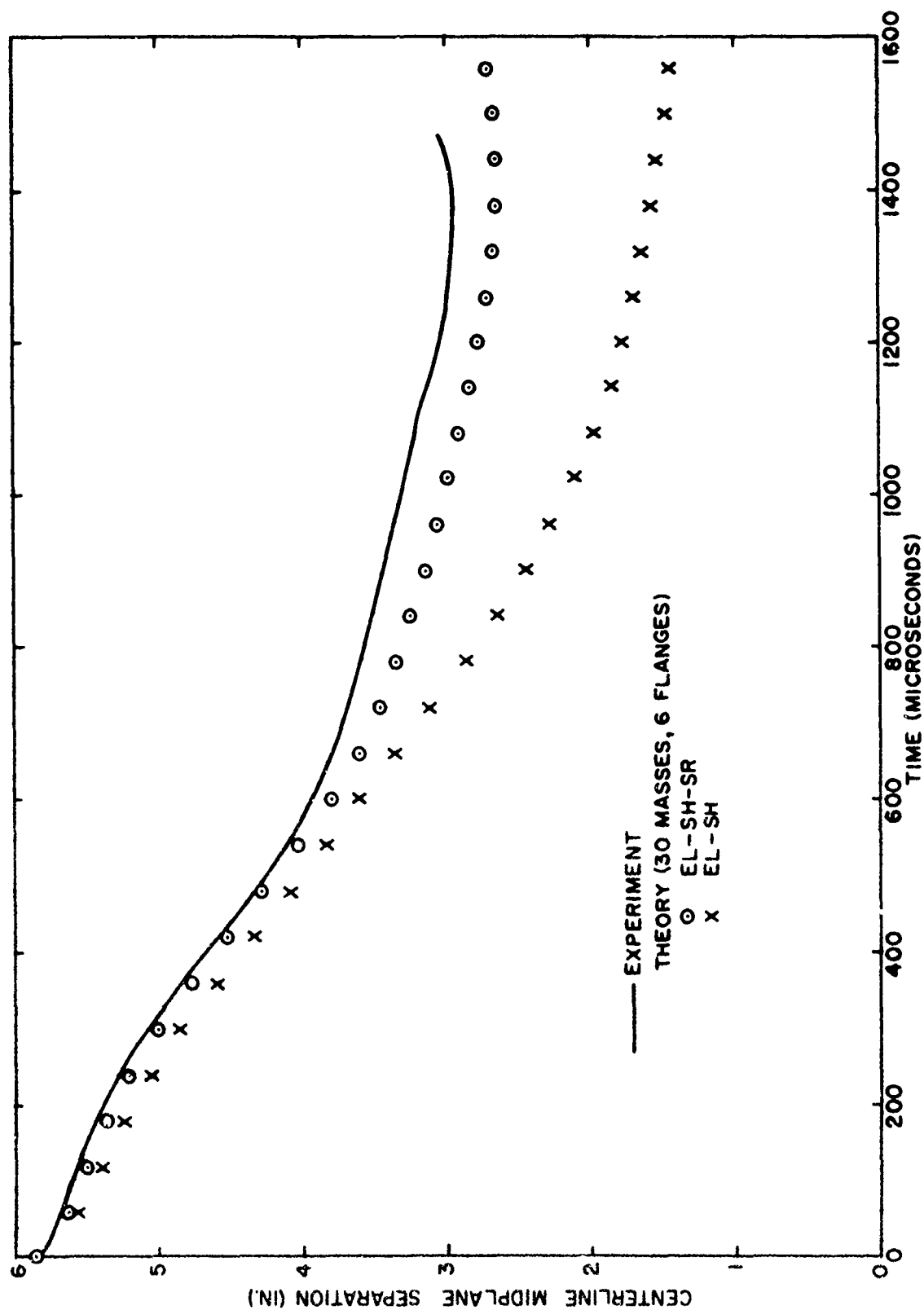


FIG. 4.32. COMPARISON OF PREDICTED AND EXPERIMENTAL CENTRAL SEPARATION RESPONSES FOR EXPLOSIVELY-LOADED 6061-T6 FREE CIRCULAR RING F15

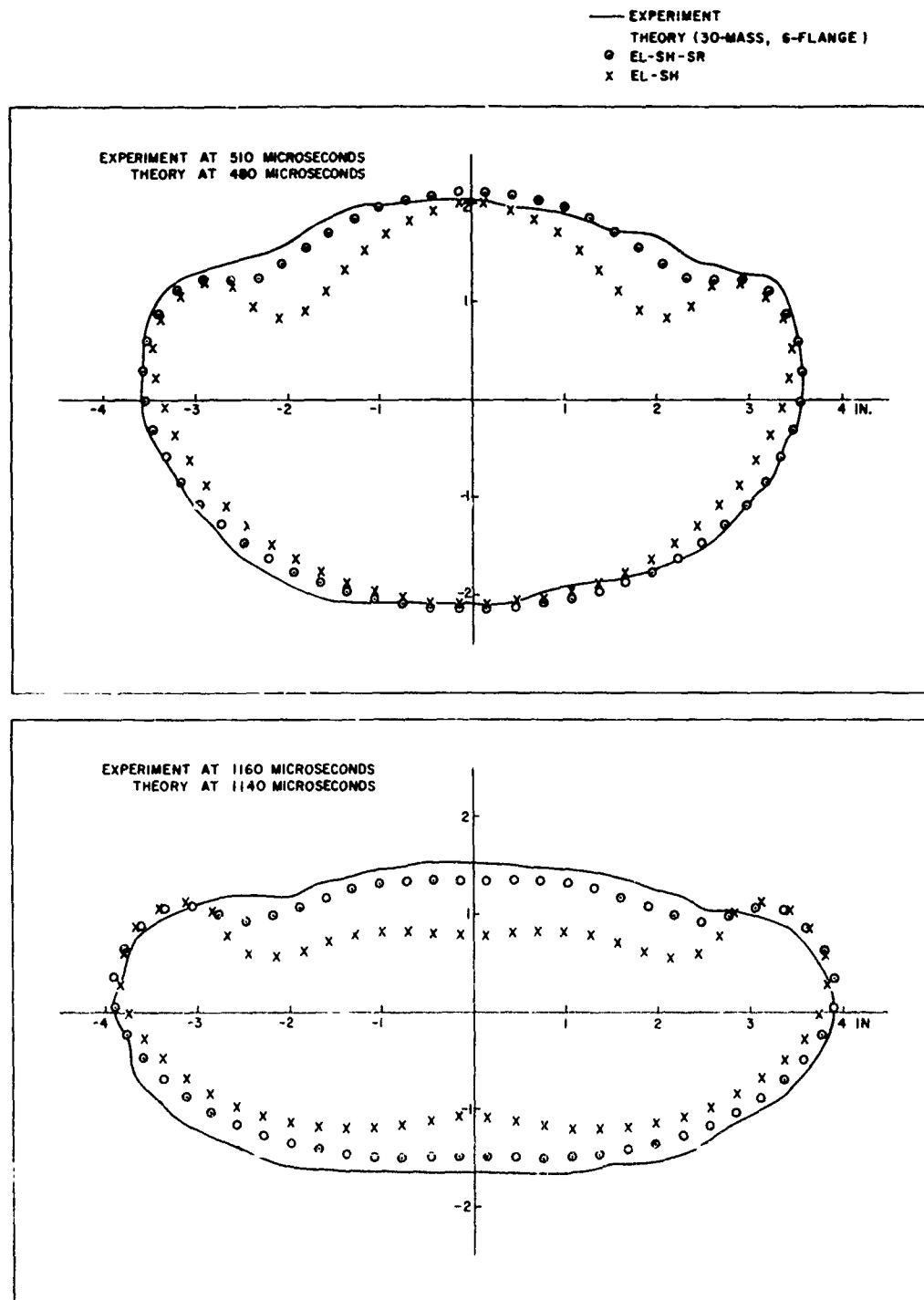


FIG. 4.33. COMPARISON OF PREDICTED AND EXPERIMENTAL DEFORMATION PROFILES FOR EXPLOSIVELY-LOADED 6061-T6 FREE CIRCULAR RING F15

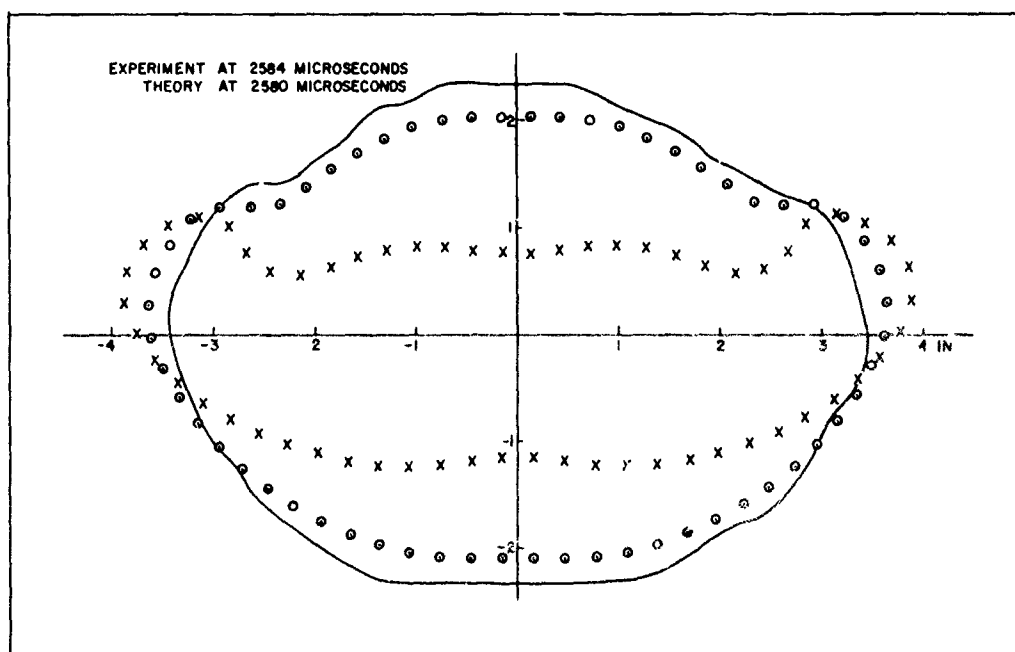
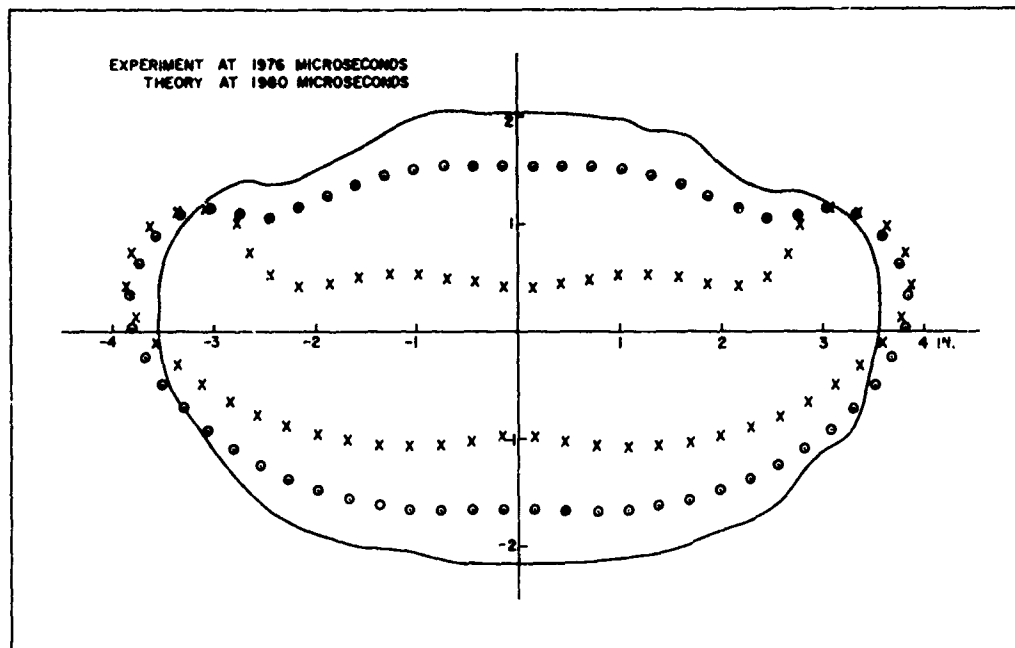


FIG. 4.33. CONTINUED

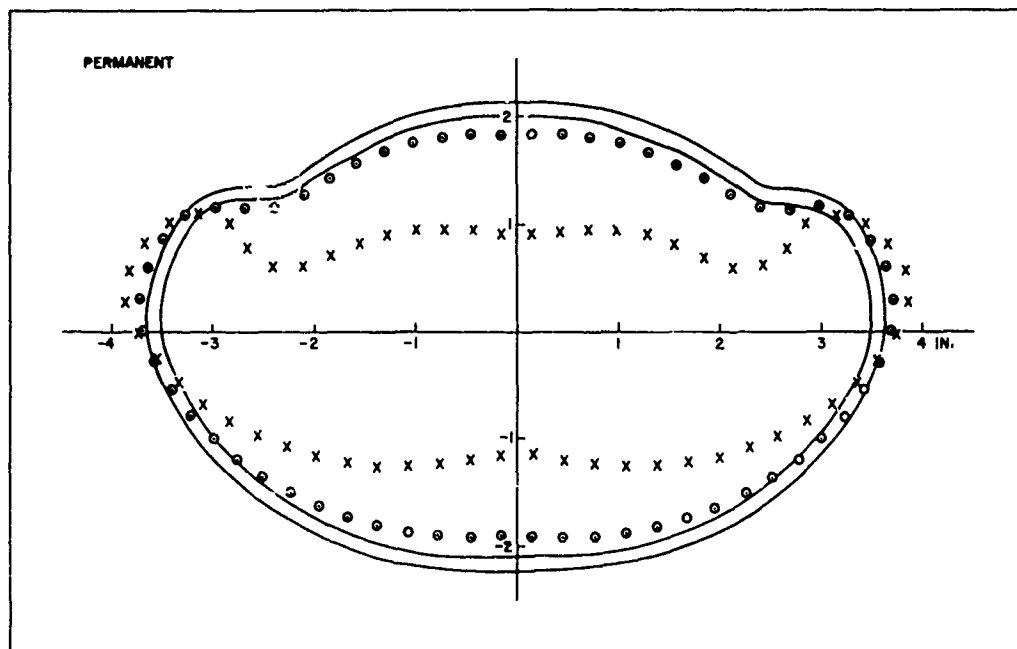


FIG. 4.33. CONCLUDED

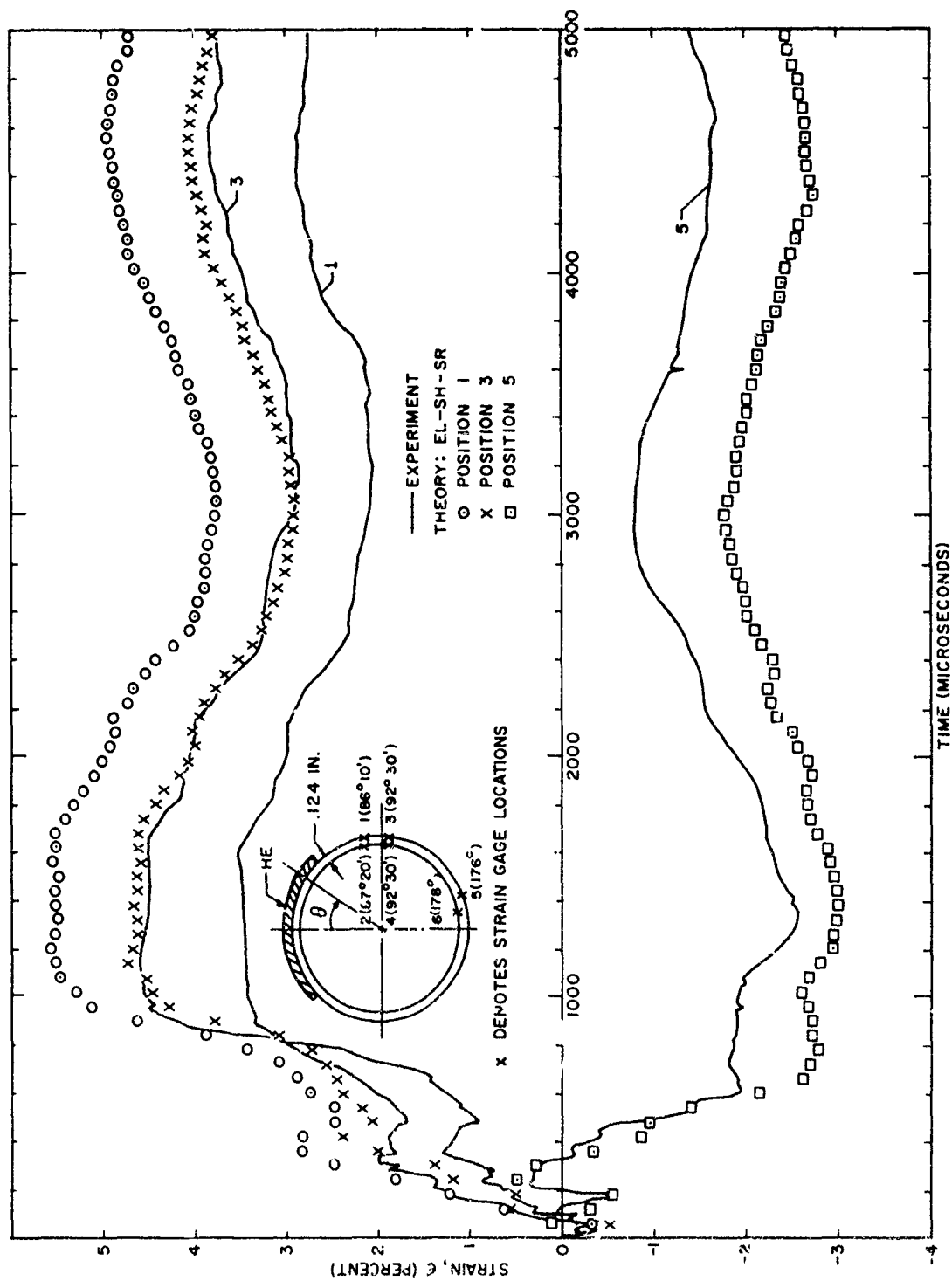


FIG. 4.34. COMPARISON OF PREDICTED AND EXPERIMENTAL STRAIN-TIME HISTORIES 1  
EXPLOSIVELY-LOADED 6061-T6 FREE CIRCULAR RING F15

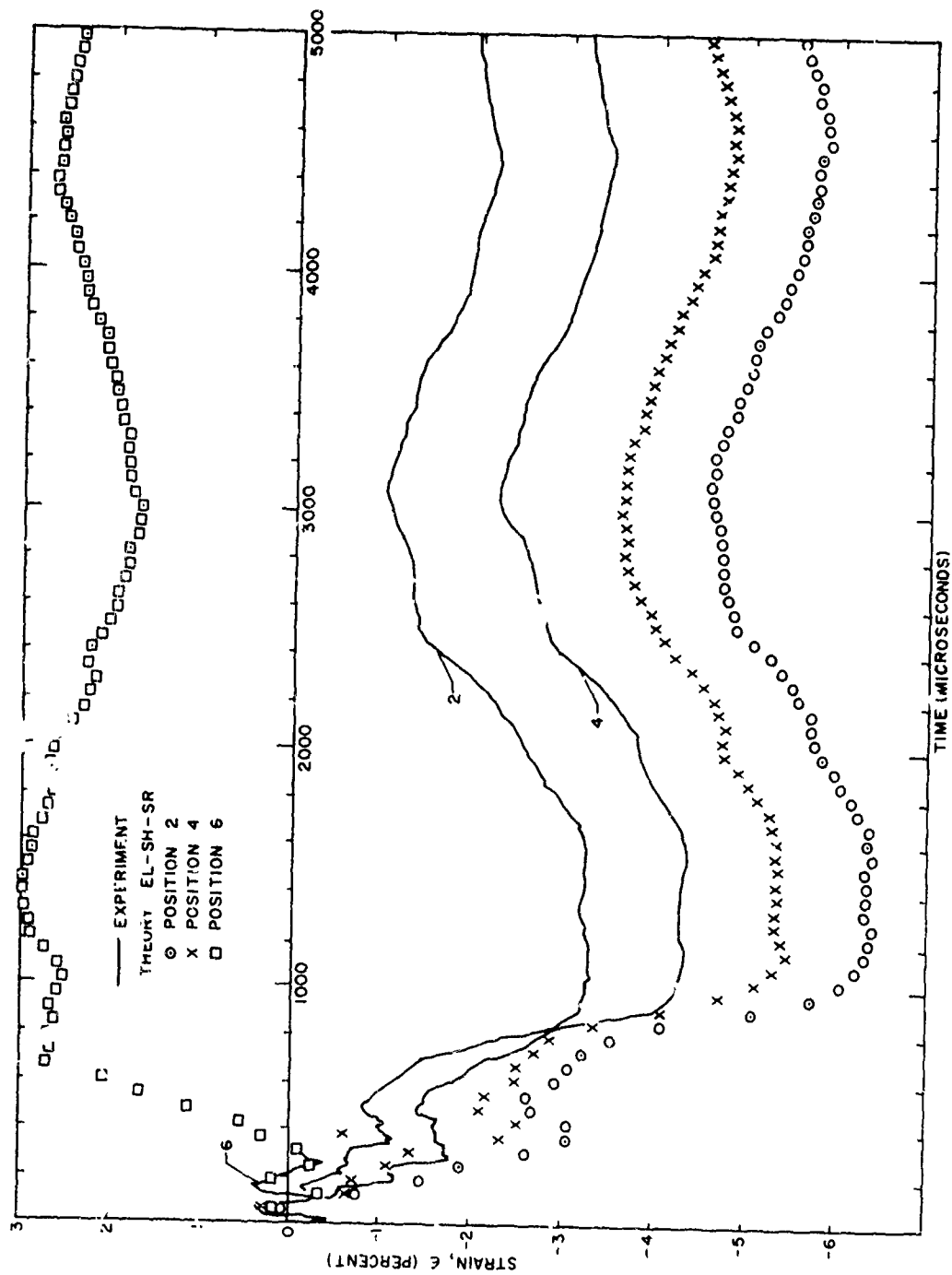


FIG. 4.34 CONCLUDED

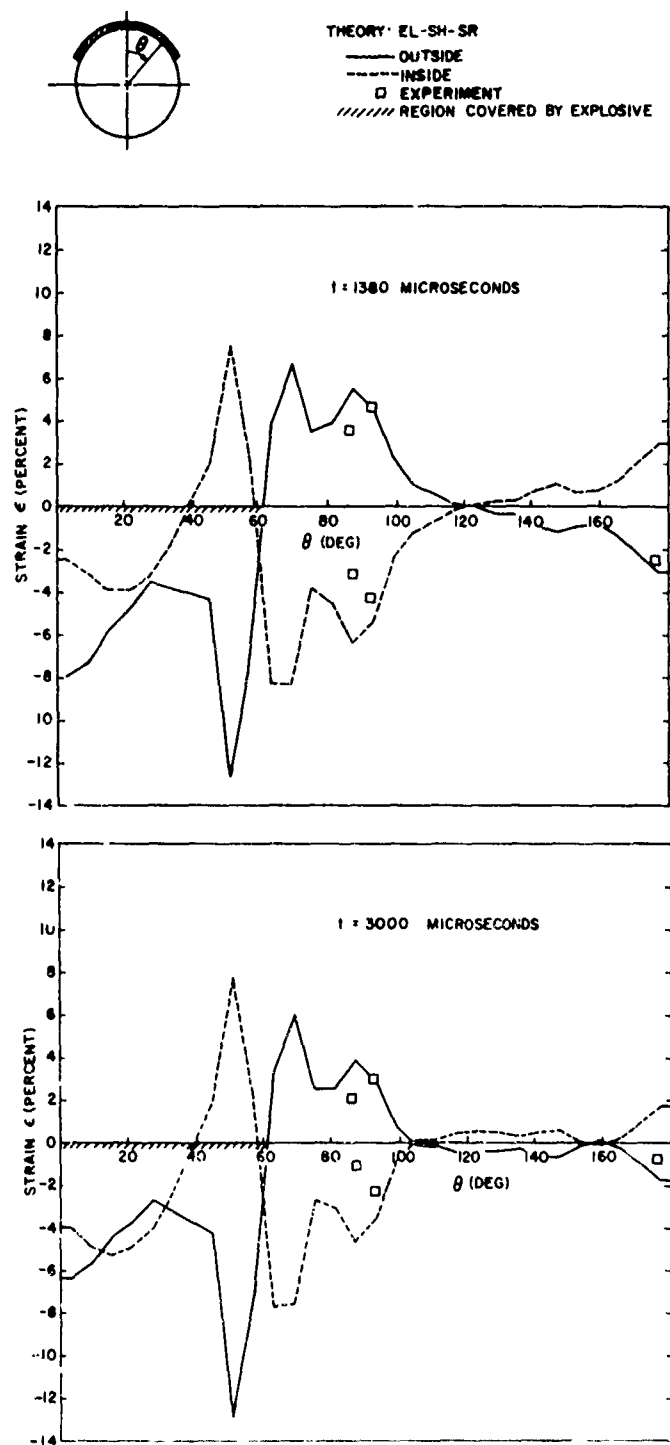


FIG. 4.35. STRAIN PROFILES FOR EXPLOSIVELY-LOADED 6061-T6 FREE CIRCULAR RING F15

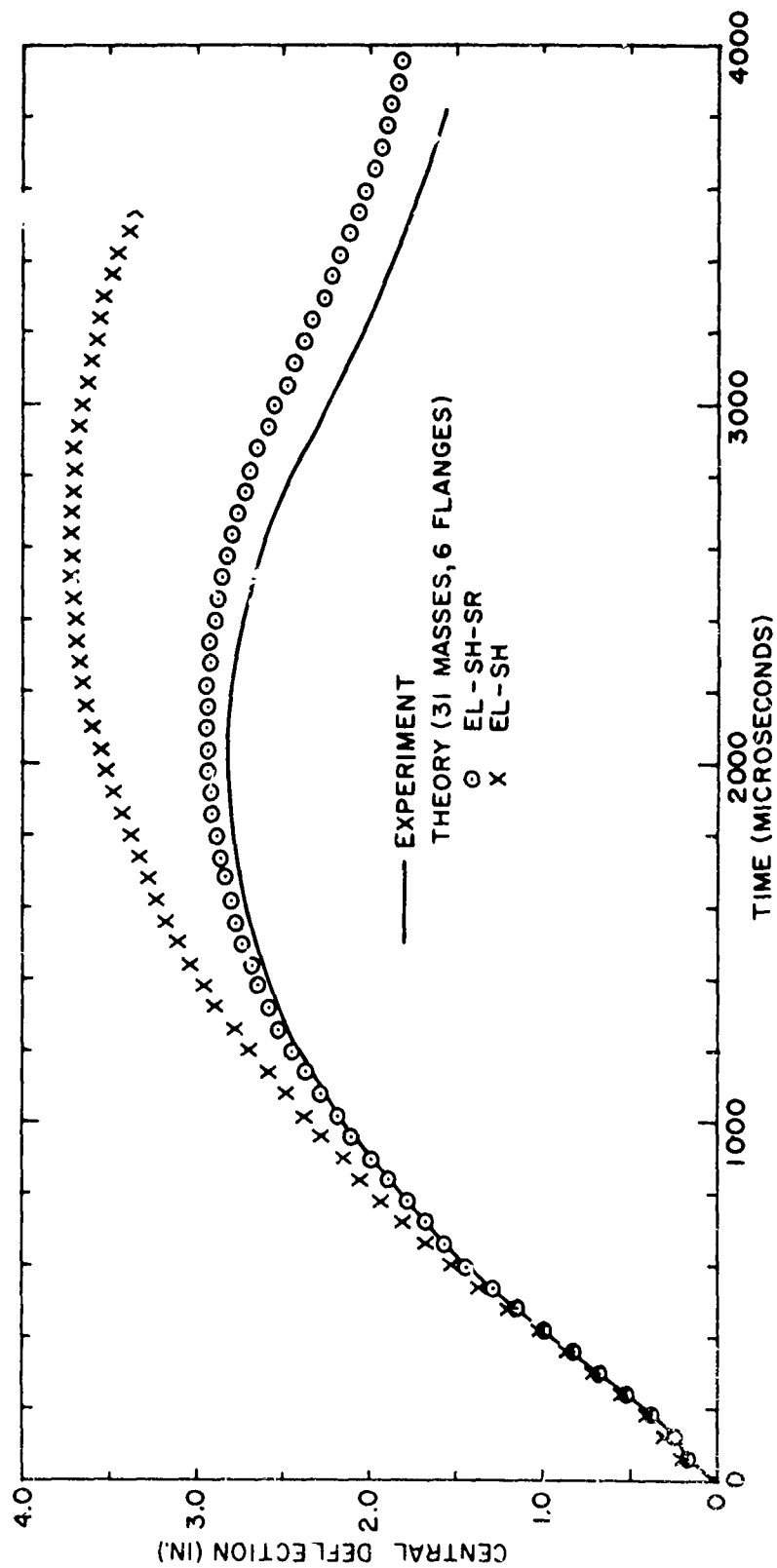


FIG. 4.36. COMPARISON OF PREDICTED AND EXPERIMENTAL CENTRAL DEFLECTION RESPONSES FOR EXPLOSIVELY-LOADED 6061-T6 CLAMPED CIRCULAR RING C4

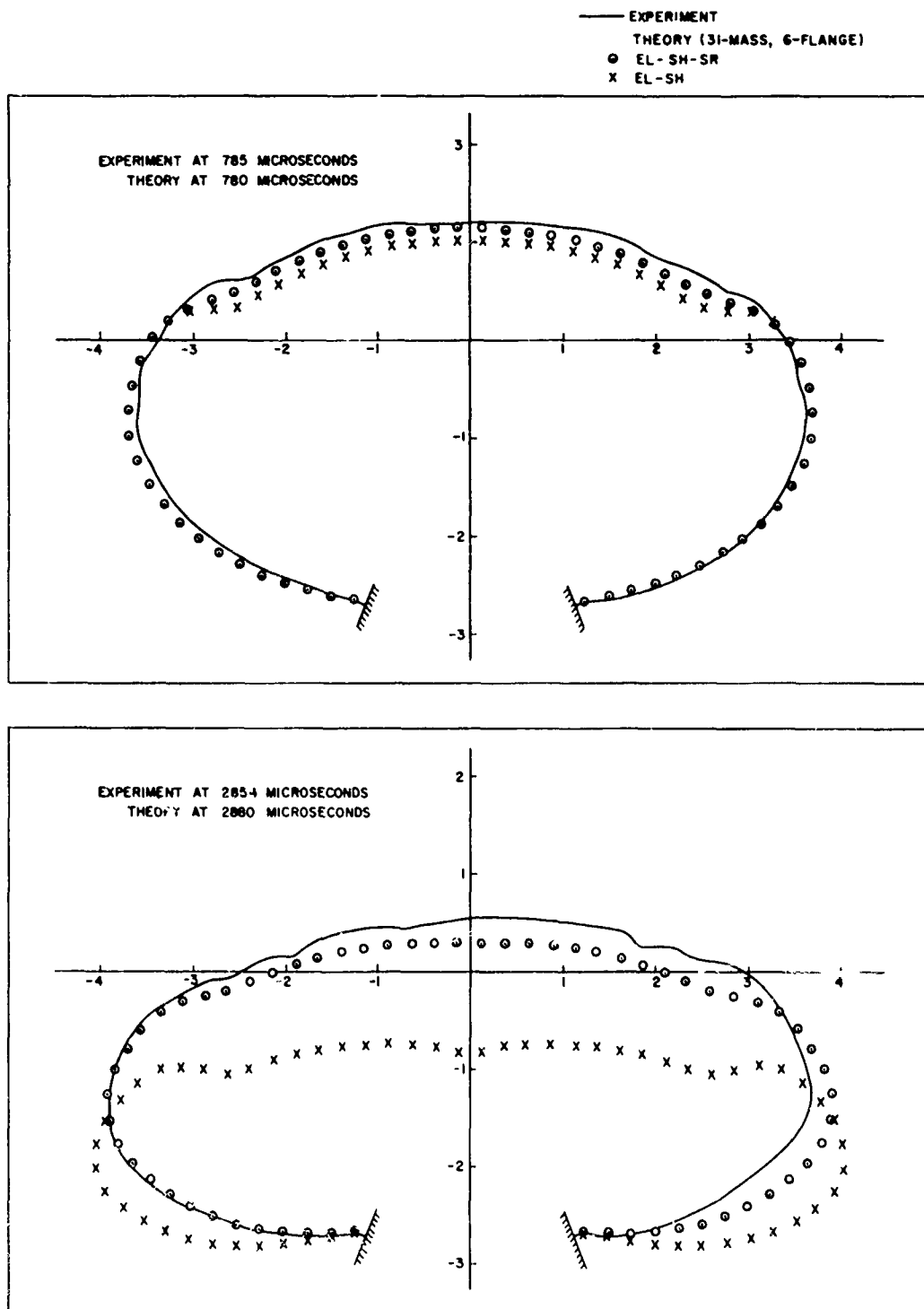


FIG. 4.37. COMPARISON OF PREDICTED AND EXPERIMENTAL DEFORMATION PROFILES FOR EXPLOSIVELY-LOADED 6061-T6 CLAMPED CIRCULAR RING C4

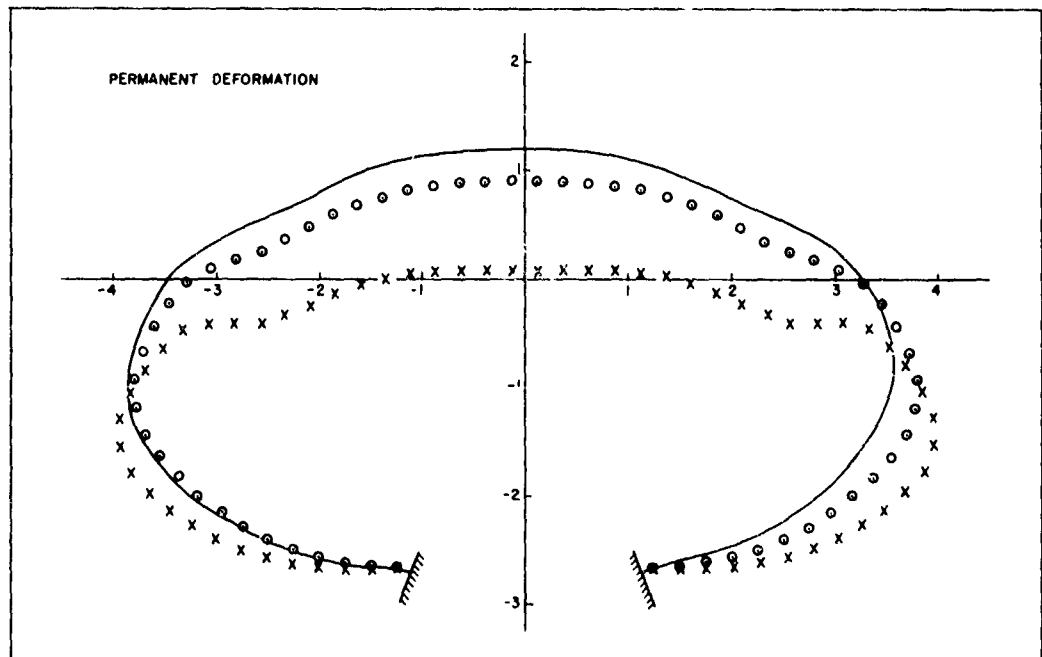
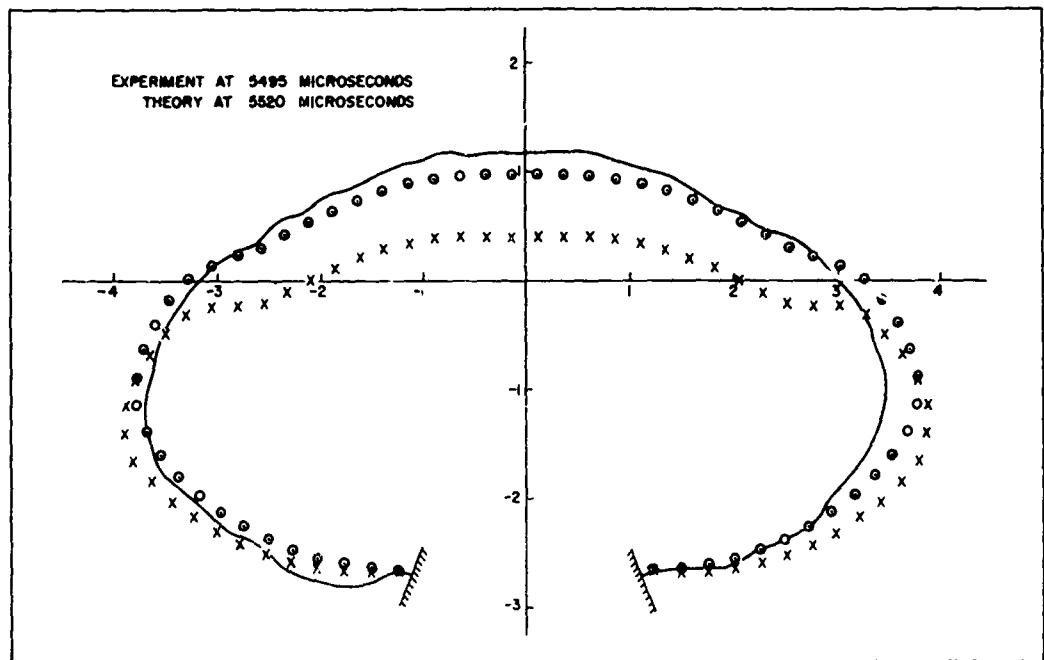


FIG. 4.37. CONCLUDED

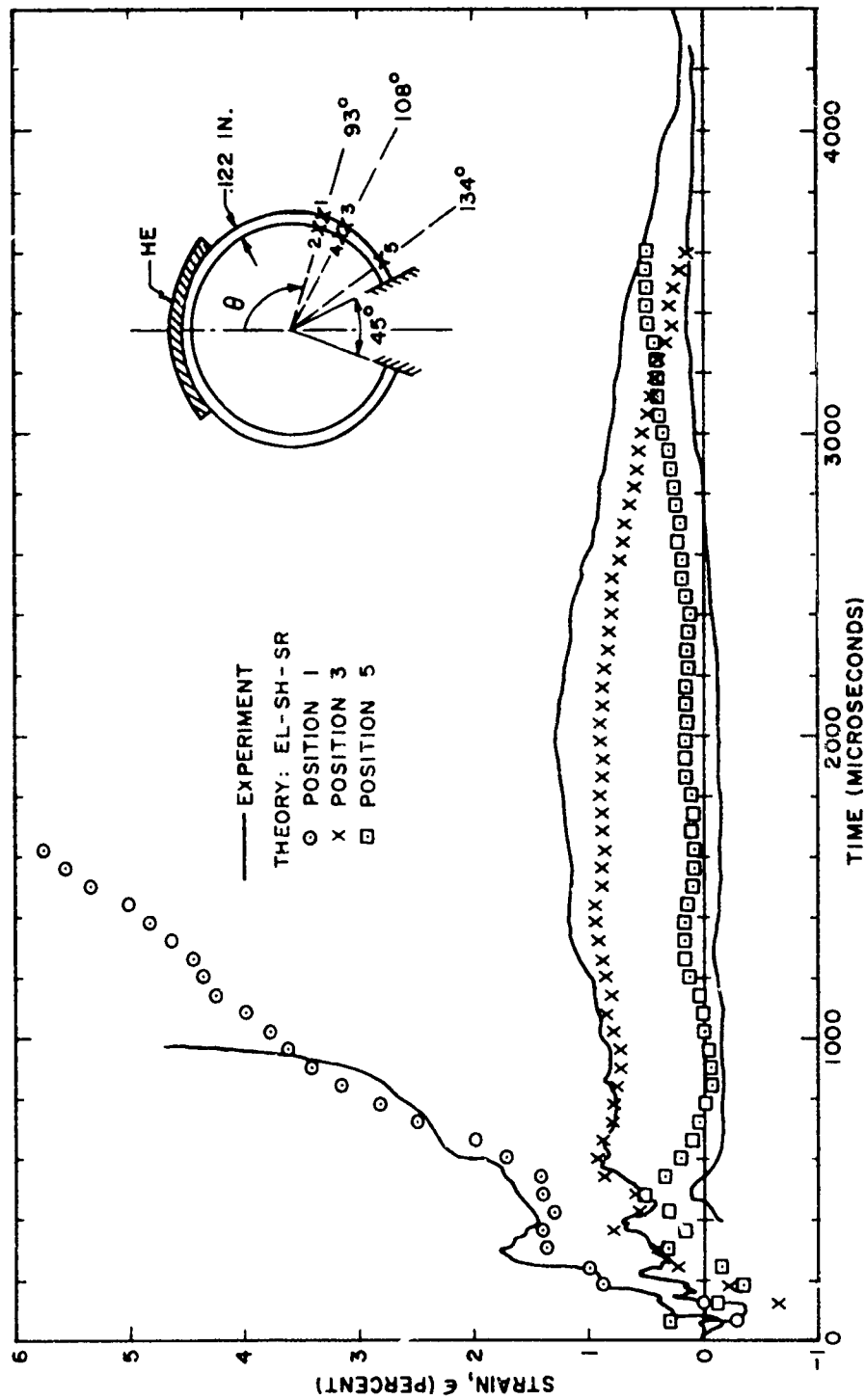


FIG. 4.38. COMPARISON OF PREDICTED AND EXPERIMENTAL STRAIN-TIME HISTORIES FOR EXPLOSIVELY LOADED 6061-T6 CLAMPED CIRCULAR RING C4

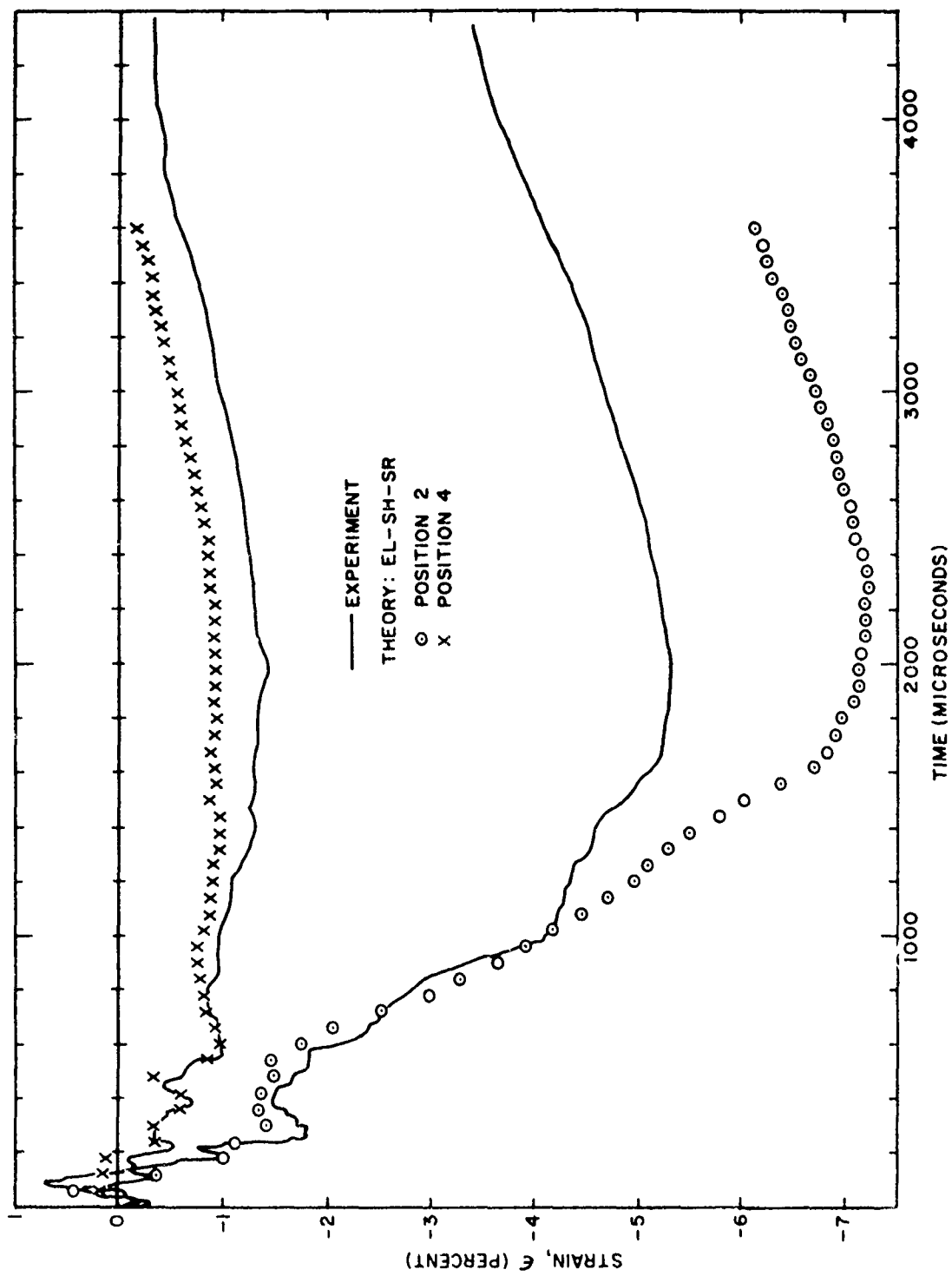
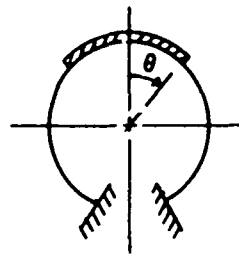


FIG. 4.38. CONCLUDED



THEORY: EL-SH-SR  
 ——— OUTSIDE  
 - - - INSIDE  
 □ EXPERIMENT  
 ///// REGION COVERED BY EXPLOSIVE

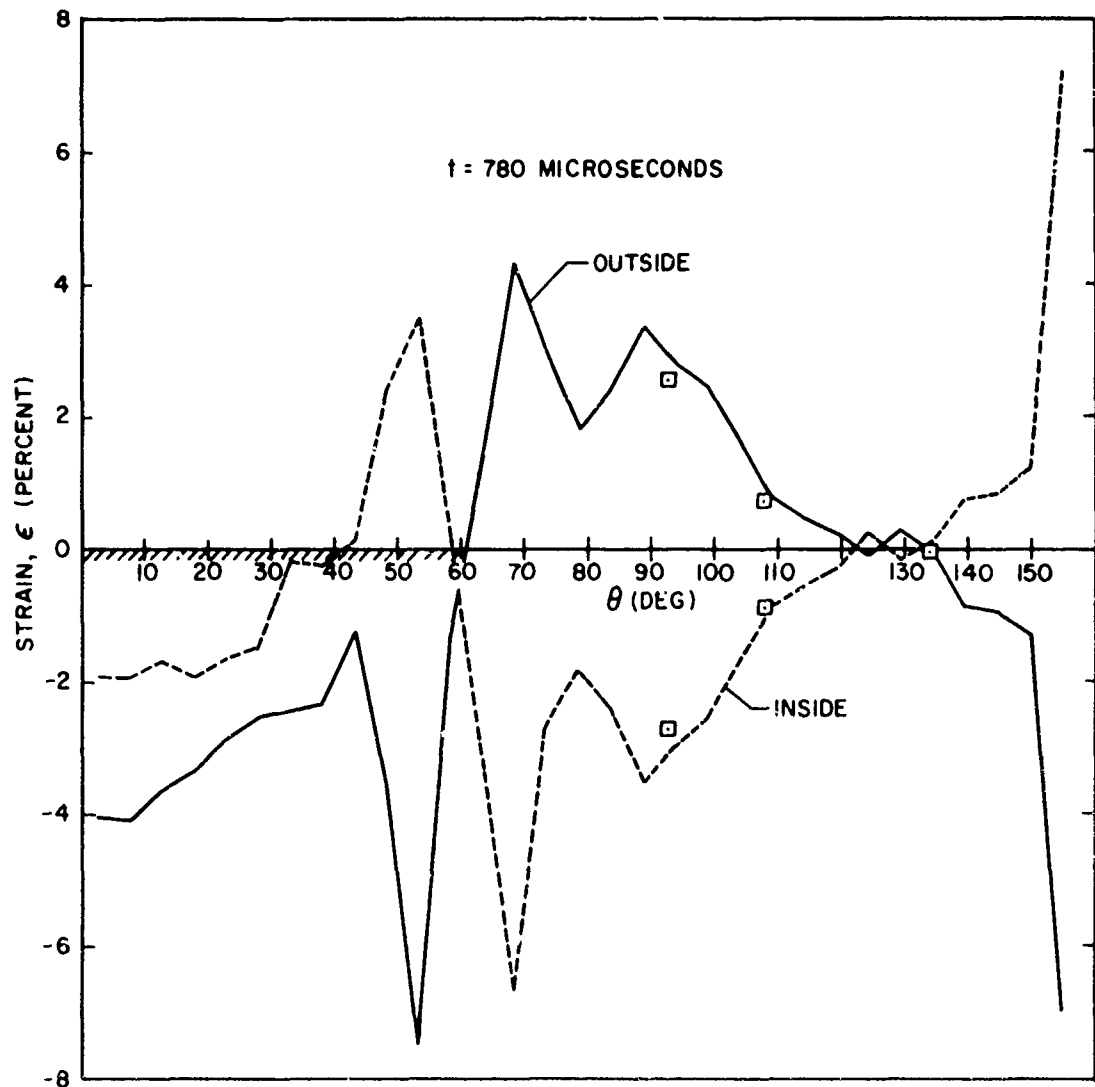


FIG. 4.39. STRAIN PROFILES FOR EXPLOSIVELY-LOADED 6061-T6 CLAMPED CIRCULAR RING C4

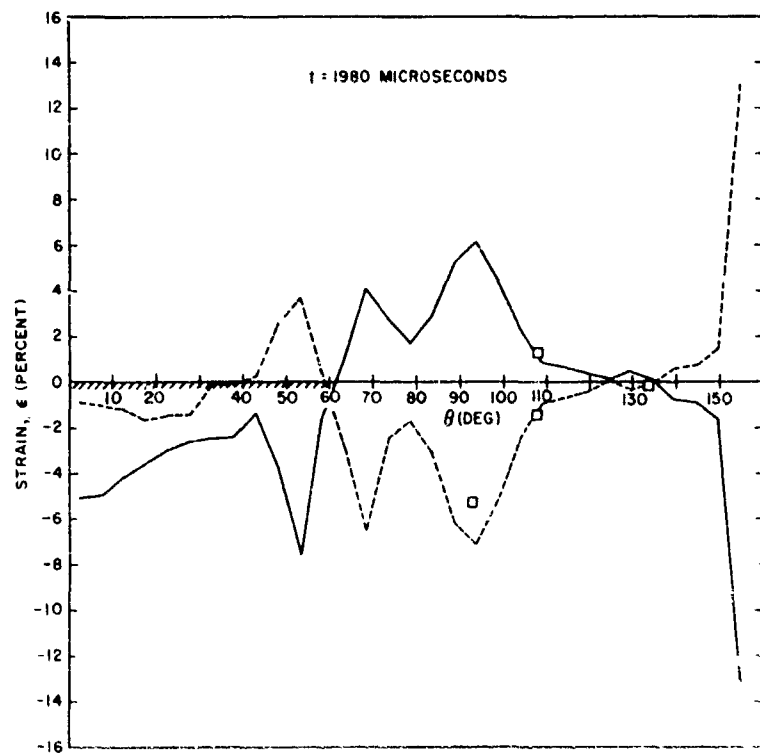
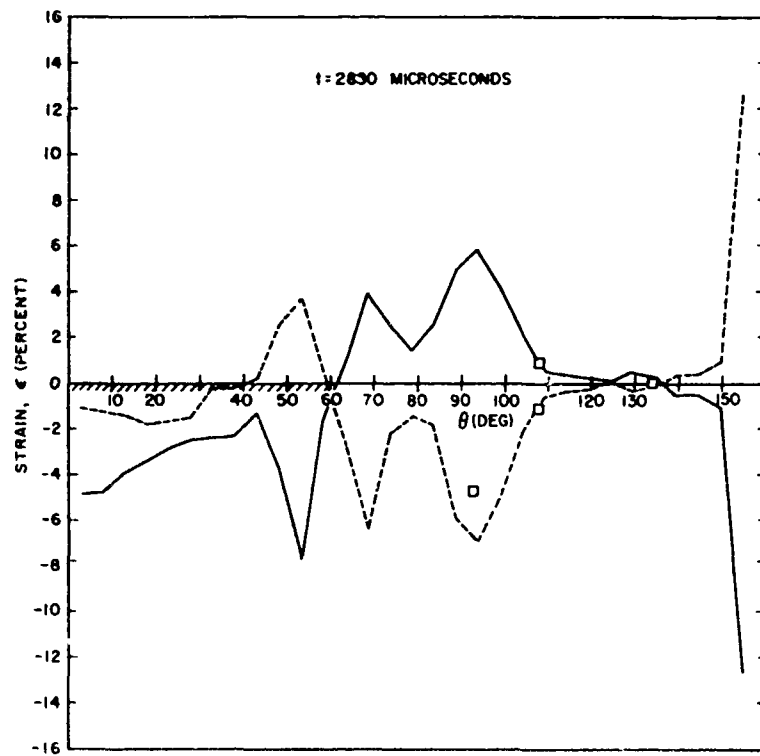


FIG. 4.39. CONCLUDED

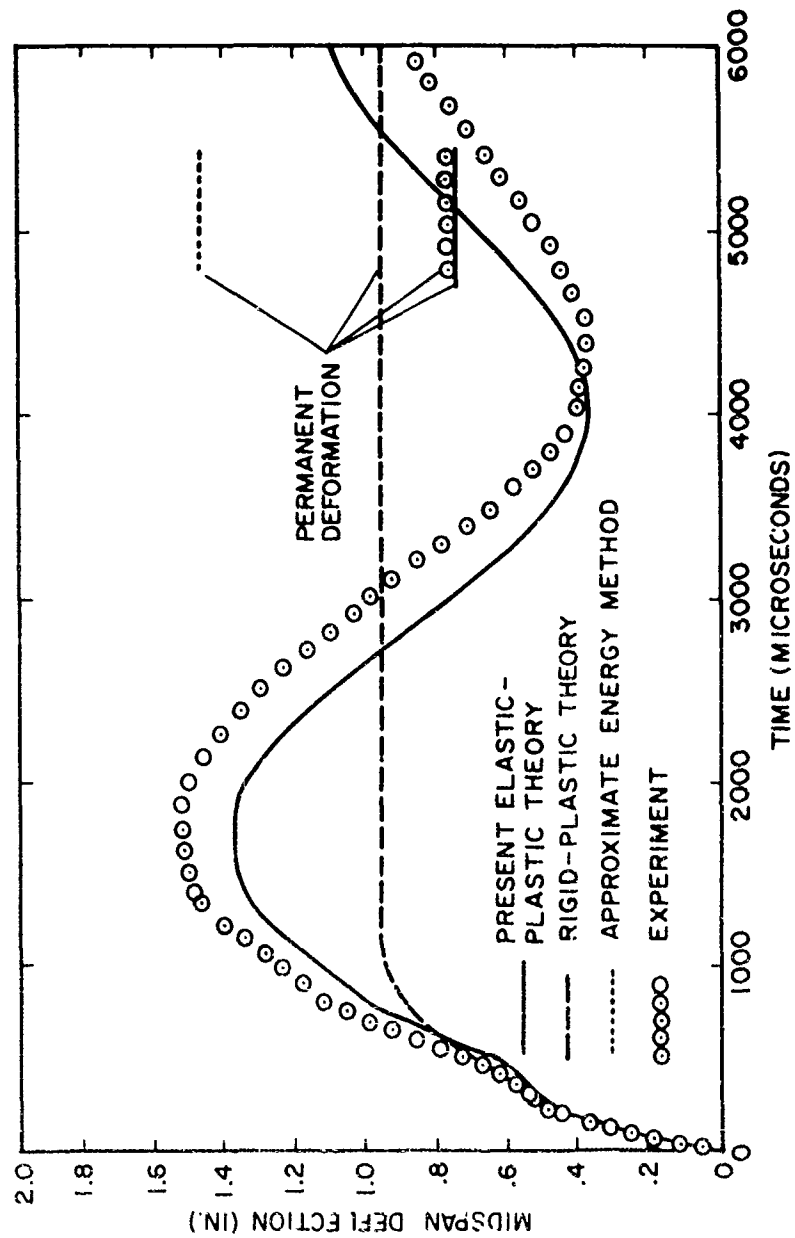


FIG. 4.40. COMPARISON OF TRANSIENT RESPONSES OBTAINED BY THE PRESENT ELASTIC-PLASTIC THEORY AND RIGID-PLASTIC THEORY (SIMPLY-SUPPORTED BEAM 121)